FABRICATION AND CHARACTERIZATION

OF INVERSE OPALS WITH

TUNABLE STOPBANDS

By

UJITH S. K. MADDUMA-BANDARAGE

Bachelor of Science in Chemistry
University of Kelaniya
Kelaniya, Sri Lanka
2010

Submitted to the Faculty of the
Graduate College of the
Oklahoma State University
in partial fulfillment of
the requirements for
the Degree of
DOCTOR OF PHILOSOPHY
December, 2018

FABRICATION AND CHARACTERIZATION

OF INVERSE OPALS WITH

TUNABLE STOPBANDS

Dissertation Approved:

Dr. Yolanda Vasquez

Dissertation Adviser

Dr. Nicholas F. Materer

Dr. Frank D. Blum

Dr. Christopher Fennell

Dr. Albert T. Rosenberger

ACKNOWLEDGEMENTS

I am sincerely grateful to my adviser Dr. Yolanda Vasquez for her guidance and support for the research that I have conducted at Oklahoma State University. I further convey my gratitude to my committee members, Dr. Nicholas F. Materer, Dr. Frank D. Blum, Dr. Christopher Fennell, and Dr. Albert T. Rosenberger for their valuable suggestions and feedbacks.

I would also like to thank faculty and staff members of the Department of Chemistry at Oklahoma State University, Ms. Lisa Whitworth and Mr. Brent Johnson at Oklahoma State University Microscopy Laboratory, and Dr. Feng Lu and Mr. Jonathan Gonzales from Helmerich Research Center at Oklahoma State University-Tulsa.

I truly admire the inspiration and guidance that I have received from my undergraduate adviser Dr. K. A. Saman Pathiratne and other faculty members at the University of Kelaniya, Sri Lanka. I would also like to appreciate all the teachers at Mahanama College, Colombo 03, Sri Lanka for the strong foundation that they have placed on me.

My deepest appreciation goes to my father Mr. Nihal S. P. K. Madduma-Bandarage and my mother Ms. Ashoka Samarasinghe for their unconditional love. I would also like to appreciate my brother Mr. Rajith D. K. Madduma-Bandarage for all the encouragement, friendship, and support. I would like to show my greatest appreciation to my loving wife Ms. Hasani G. Jayasinghe, without whose encouragement and persistent help, this dissertation would not have been materialized. My further gratitude goes to my in-laws, especially father-in-law late Mr. Piyasiri Jayasinghe, for their love and support.

Finally, I would like to thank all of my friends for their valuable friendship that I received whenever it was necessary at the most.

Name: UJITH S. K. MADDUMA-BANDARAGE

Date of Degree: DECEMBER, 2018

Title of Study: FABRICATION AND CHARACTERIZATION OF INVERSE OPALS WITH TUNABLE STOPBANDS

Major Field: CHEMISTRY

Abstract:

Inverse opals, a major type of self-assembled structures, provide good examples of photonic crystals that result from the periodic arrangement of voids. The periodic arrays of voids interfere with the light passing through them and prevent the propagation of certain wavelengths (stopband). The ability to tune the stopband of an inverse opal is important in applications such as photonics and sensing. Inverse opal films can be fabricated by filling the interstitial sites of self-assembled colloids with a precursor solution and then removing the template (assembly of colloids) by means of heat or chemical dissolution. However, the fabrication of inverse opals with long range ordering of voids by using traditional methods is challenging due to the introduction of defects. Co-assembly is an evolving technique that is used to generate inverse opals with minimal defects but the use of experimental conditions to control the defects has not been widely explored. In this study, silica-based inverse opals were fabricated by using co-assembly technique and the quality of the resultant films was evaluated with respect to the colloidal concentration and sol-gel precursor concentration. To tune the stopband, the size of voids was altered by varying the size of colloids. Also, another type of inverse opals was produced from a cross-linked polymer based on 2-hydroxyethyl methacrylate which can result tunable stopbands in response to the external stimuli. The mechanical and dimensional stability of the polymer inverse opals were improved using a poly(dimethylsiloxane) mold. Overall, defect-free inverse opal photonic crystals with tunable stopbands in the visible region of the electromagnetic spectrum have been produced using inexpensive and simple techniques.

TABLE OF CONTENTS

Chapter Page

LIST OF TABLES

Table Page

LIST OF FIGURES

Figure Page

Figure Page

Figure Page

Figure Page

LIST OF SCHEMES

Scheme Page

CHAPTER I

INTRODUCTION

Photonic crystals are a group of materials that interact with light in a unique way. The periodic arrays of microstructures in photonic crystals can prevent the propagation of specific wavelengths of light, thereby resulting in a photonic band gap.[1-3] Photonic band gap materials are used in a variety of applications such as optical transistors,[4] optical waveguides with sharp bends,[5, 6] optical fibers,[7, 8] optical integrated circuits,[6] high-efficiency lasers,[9-11] etc. These photonic crystals are generally produced *via* lithography or self-assembly where the latter is simple and inexpensive compared to the former.[12-16] Self-assembly in photonic crystals is an autonomous process that allows particles, made out of either organic or inorganic compounds,[17, 18] to assemble into periodic structures.[19] For example, polymer colloids dispersed in a solvent can be self-assembled into a close-packed structure by evaporating the solvent to produce colloidal assemblies known as opals.

The opals are used as templates to fabricate inverse opal structures. Theoretically, it is predicted that inverse opals are more useful as photonic band gap materials compared to opals.[16] Inverse opals block the propagation of specific wavelengths in the visible range of the electromagnetic spectrum and consequently show stopbands. Stopband, determines the color of the inverse opal; hence these materials find interesting applications as displays and sensors. Position of a stopband varies depending on the dynamic and static changes of the matrix and structure of an inverse opal; for instance, size of voids, or effective refractive index of the material result in stopband shifts.

Changing the size of voids to obtain stopband shifts is advantageous because it provides control in a broad range of wavelengths.

This dissertation mainly focuses on the fabrication of inverse opals to obtain static and dynamic variation in the position of the stopbands. The static variation was obtained by changing the size of voids in silica inverse opal thin films and the dynamic variation can be obtained by fabricating inverse opal hydrogels from poly(HEMA/DMAEMA/TEGDMA) (HEMA = 2-hydroxyethyl methacrylate, DMAEMA = N,N-(dimethylaminoethyl)methacrylate, and TEGDMA = tetraethylene glycol dimethacrylate). The first chapter describes the theoretical aspects of photonic crystals, bandgap structure, light diffraction, methods of fabrication of opals and inverse opals, and potential applications of photonic crystals.

The second chapter describes a study conducted to investigate the limitations and quality of the inverse opals made by using a relatively new method known as co-assembly. The co-assembly method was introduced recently to substitute the conventional infiltration method used to fabricate inverse opals.[20] Usually, inverse opals are made in three steps: assembly of colloids on a substrate, infiltration of the sol-gel precursor solution, and removal of the template. In co-assembly, the first two steps are performed simultaneously, using a mixture containing both template particles and partially condensed sol-gel precursor molecules to reduce the defects associated with the inverse opals produced using the conventional method.[20] The conventional method causes defects such as cracks, dislocations of particles, and presence of multiple lattice orientations. Although several remedies have been proposed,[21-24] most of them are complex, time consuming, and expensive. Therefore, co-assembly is a good alternative. This chapter highlights the parameters, such as concentrations of colloids and sol-gel precursor, which affect the quality of the co-assembled thin films and ways to improve the quality. Furthermore, the defects were successfully semi-quantified using image analysis techniques. In addition to that, the fabrication of inverse opals with tunable stopbands is also explained. The

position of the stopband was varied by changing the size of the voids. Here, poly(methyl methacrylate) (PMMA) beads were used to generate the templates and the sizes of the PMMA beads were varied by changing the concentration of methyl methacrylate used in synthesis of PMMA.

Several methods have been used to analyze the periodic structures, such as opals and inverse opals. For example, small-angle x-ray diffraction (SAXS),[25, 26] Transmission Electron Microscopy (TEM),[27-29] Scanning Electron Microscopy (SEM),[30, 31] and diffraction of light.[32] However, there are few studies that use image analysis techniques to determine the structure of inverse opals. In chapter 3, a methodology was introduced to determine the structure of the inverse opal films made using the co-assembly technique. Here, SEM images of inverse opals made with different ratios of concentrations of colloids to tetraethyl orthosilicate were analyzed for the size of the voids, interplanar distance, center-to-center distance, the extra amount of silica on the surface, and percentage of surface cracks. Moreover, it was shown that the lattice orientations of voids can be determined from 2D-fast Fourier transform (2D-FFT) analysis.

Dynamic changes in the position of the stopband are important in sensing applications. A photonic crystal which can change the position of the stopband reversibly in the presence of an analyte is considered as a visual sensor. Since hydrogels can significantly change their volume in response to external stimuli, such as solvents, temperature, lights, ionic strength, etc., hydrogels are ideal candidates for inverse opal photonic sensors. Poly(HEMA)-based hydrogels, with modifications, are extensively studied as materials for optical sensors.[33-36] In chapter 4, a study was conducted using poly(HEMA/DMAEMA/TEGDMA) to produce the matrix of inverse opal films. This polymer is known to swell remarkably in solvents such as N,N-dimethyl formamide (DMF), dimethyl sulfoxide (DMSO), methanol, ethanol, and ethylene glycol.[37] Here, a new methodology was introduced to increase the mechanical and dimensional stability of the hydrogel inverse opal film.

CHAPTER II

AN OVERVIEW OF PHOTONIC CRYSTALS

2.1 Photonic crystals

Photonic crystals (PhCs) are a unique type of materials that control the propagation of light. PhCs can be classified as natural[1, 38, 39] and synthetic.[40] The microstructures seen in insects,[41-45] birds,[46-49] gemstones,[50] reptiles, aquatic species,[51-53] etc., provide examples for natural PhCs. Artificial materials containing a periodic array of microstructures are considered synthetic PhCs. Unlike pigments that absorb or emit certain wavelengths of light, PhCs produce colors due to the reflection of light by microstructures.[1] These microstructures have materials with regular arrays of high and low refractive indices.

PhCs are classified into three subcategories based on the direction of periodicity: 1D, 2D, 3D (**Figure 2-1)**. Bragg grating is an example for 1D-PhCs. The patterned structures of the scales of a butterfly wing are a good example of a natural 2D-PhC. Opal gemstones such as Ethiopian opals and Australian opals are well-known examples for 3D-PhCs. The most common 3D-PhC lattice types are face-centered cubic (fcc), woodpile, spiral lattice, and quasi-diamond lattice.[54] Since the propagation of light interferes in all dimensions, 3D-PhCs have many potential applications, and the fabrication of artificial 3D-PhCs has been broadly studied.[55-60]

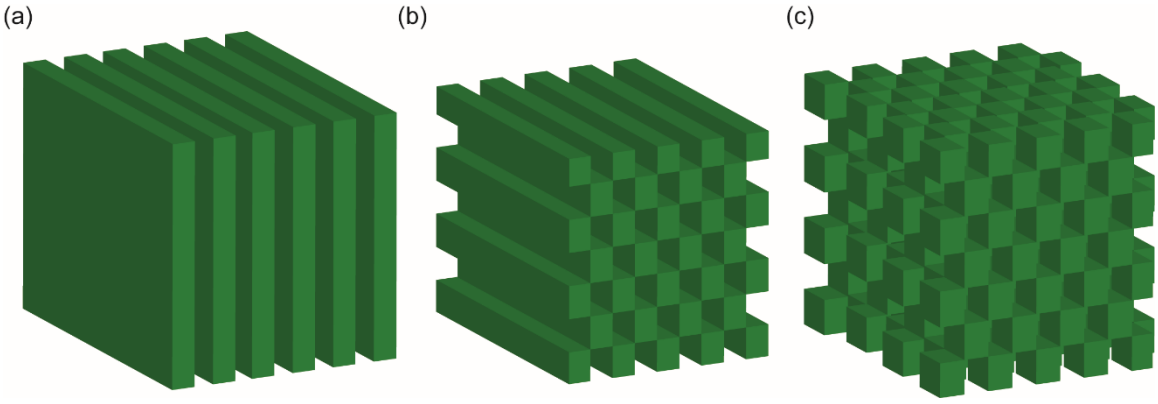

Figure 2-1: A cartoon representation of (a) 1D, (b) 2D, and (c) 3D-photonic crystals.

2.2 Significance and applications

In semiconductors, a periodic potential influences the motion of electrons and creates allowed and forbidden electronic energy states. The forbidden states generate the electronic bandgap. Similarly, in PhCs, dielectric structures are periodically arranged and can prohibit the propagation of some frequencies of electromagnetic waves, creating energy gaps known as photonic bandgaps.[61] Manipulation of light in various ways can be achieved by engineering the bandgap by changing the lattice parameters or introducing artificial defects, such as line defects or point defects.[13, 62-64] A line defect is a disturbance introduced to a line of the periodic array that allows the propagation of light along only the direction of the defect that acts as a waveguide.[65] A point defect introduces a defect only to a certain point of the lattice and results in a photonic nanocavity that can trap light.[66] Photonic circuits can be fabricated by introducing waveguides and nanocavities to the same PhC.[67] Furthermore, by changing a lattice parameter such as interplanar distance; the bandgap of the PhC can be manipulated to alter the wavelength of the reflected light. This feature can be used in applications such as displays[68] and sensors.[34] PhCs can even improve the photocatalytic activity of

a system by increasing the absorbance of light, resulting the slow photon effect, where the speed of light decreases near the photonic bandgap.[69]

2.3 Photonic band structure

A photonic band gap is achieved when propagation of certain frequencies of light are prohibited in all possible directions inside a photonic material. The interrupted frequencies cause a gap in the transmitted light. In 1887, Lord Rayleigh proved the existence of a 1D photonic bandgap, and almost a century later Eli Yablonovitch and Sajeev John have confirmed the 2D and 3D photonic bandgaps.[2, 3] The finding of the 2D and 3D bandgap was inspired by the work of Charles Galton Darwin, who had introduced the dynamical theory of X-ray diffraction.[70] In order to have a 3D photonic bandgap, two important features – electromagnetic wave polarization and higher refractive index contrast – must be introduced to the dynamical theory.

The Maxwell equations govern macroscopic electromagnetism and the propagation of light in a dielectric media. The four Maxwell equations are

$$\nabla \times E + \frac{\partial B}{\partial t} = 0 \qquad \textbf{(2-1)}$$

$$\nabla \times H - \frac{\partial D}{\partial t} = J \qquad \textbf{(2-2)}$$

$$\nabla \cdot B = 0 \qquad \textbf{(2-3)}$$

and

$$\nabla \cdot D = \rho \qquad \textbf{(2-4)}$$

where B is the magnetic induction field, D is the electric displacement, J is the electric current density, and ρ is the free charge density. Since the structure is constant over time and there are no current or free charges, both J and ρ are set to zero. Moreover, D and E are related to each other *via* a power series. Usually, PhCs are made of transparent, macroscopic, and isotropic materials,

hence a relationship between D and E is obtained by assuming smaller field strengths and no material dispersion[71] and the relationship is given by

$$D = \varepsilon_0 \varepsilon E \quad \textbf{(2-5)}$$

Also, a relationship between B and H can be obtained:

$$B = \mu_0 \mu H \quad \textbf{(2-6)}$$

The ε_0 is the vacuum permittivity, ε is the relative permittivity, μ_0 is the vacuum permeability, and μ is the relative permeability; for many dielectric materials, μ is close to unity. From all the assumptions mentioned above and using **equation (2-5)** and **(2-6)** Maxwell's equations are simplified to:

$$\nabla \times E(r,t) + \mu_0 \frac{\partial H(r,t)}{\partial t} = 0 \quad \textbf{(2-7)}$$

$$\nabla \times H(r,t) - \varepsilon_0 \varepsilon \frac{\partial E(r,t)}{\partial t} = 0 \quad \textbf{(2-8)}$$

$$\nabla \cdot H(r,t) = 0 \quad \textbf{(2-9)}$$

$$\nabla \cdot \varepsilon E(r,t) = 0 \quad \textbf{(2-10)}$$

Since the Maxwell equations are linear and E and H depend on both space and time, both fields can be separated to:

$$E(r,t) = E(r)e^{-i\omega t} \quad \textbf{(2-11)}$$

$$H(r,t) = H(r)e^{-i\omega t} \quad \textbf{(2-12)}$$

where ω is the frequency. Application of **equation (2-11)** and **(2-12)** to Maxwell's curl equations yields

$$\nabla \times E(r) = i\omega \mu_0 H(r) \quad \textbf{(2-13)}$$

$$\nabla \times H(r) = -i\omega \varepsilon_0 \varepsilon(r) E(r) \quad \textbf{(2-14)}$$

By solving **equation (2-14),** and substituting $\nabla \times E$ to the **equation (2-13)** the master equation can be derived,

$$\nabla \times \left(\frac{1}{\varepsilon(r)} \nabla \times \mathrm{H(r)}\right) = \frac{\omega^2}{c^2} H(r) \qquad \textbf{(2-15)}$$

where c is the speed of light and $c = 1/\sqrt{(\varepsilon_0 \mu_0)}$. Similarly, an equation can be derived for the electric field. For simplicity, only the magnetic field is considered for the next step. **Equation (2-15)** has a form of an eigenvalue problem, where H is the eigenvector. The operator $\nabla \times (1/(\varepsilon(r)) \nabla)$ is known as the Hermitian operator, which has positive and real values. So, the wave equation can be written in terms of the magnetic field as:

$$\nabla \times \left(\frac{1}{\varepsilon(r)} \nabla \times \mathrm{H(r)}\right) = k^2 H(r) \qquad \textbf{(2-16)}$$

where k^2 is the eigenvalue and $k = \omega/c$. From Bloch theorem,

$$H(r) = h_k(r) e^{ik \cdot r} \qquad \textbf{(2-17)}$$

Furthermore, application of the Bloch theorem for the magnetic field [**equation (2-17)**] to the master **equation (2-16)** yields:

$$(\nabla + ik) \times \frac{1}{\varepsilon_r} (\nabla + ik) \times h_k = \left(\frac{\omega_k}{c}\right) h_k \qquad \textbf{(2-18)}$$

The variational theorem is used to obtain the lowest eigenmode, where

$$\left(\frac{\omega_k}{c}\right) = min \frac{\int |(\nabla + ik) h_k|^2 \, d\Omega}{\int \varepsilon |h_k|^2 \, d\Omega} \qquad \textbf{(2-19)}$$

In order to minimize **equation (2-19)**, the denominator has to be maximized. This is possible only if the magnetic field is in the high dielectric medium (ε is higher). So, the mode with the lowest order stays in the highest dielectric medium, whereas the next eigenmode resides in the lowest dielectric medium; the difference is responsible for the photonic bandgap (**Figure 2-2**). Since the wave vector of a photon, k, ($k = 2\pi/\lambda$) is related to the angular frequency, ω, by $\omega = k/c$, the plot between ω and k will show the possible states for a particular PhC. The following equation gives the band structure for a 1D-PhC:[72]

$$\omega = {ck}/{n} \qquad \textbf{(2-20)}$$

where n is the refractive index of the material, which is equal to $\sqrt{\varepsilon}$.

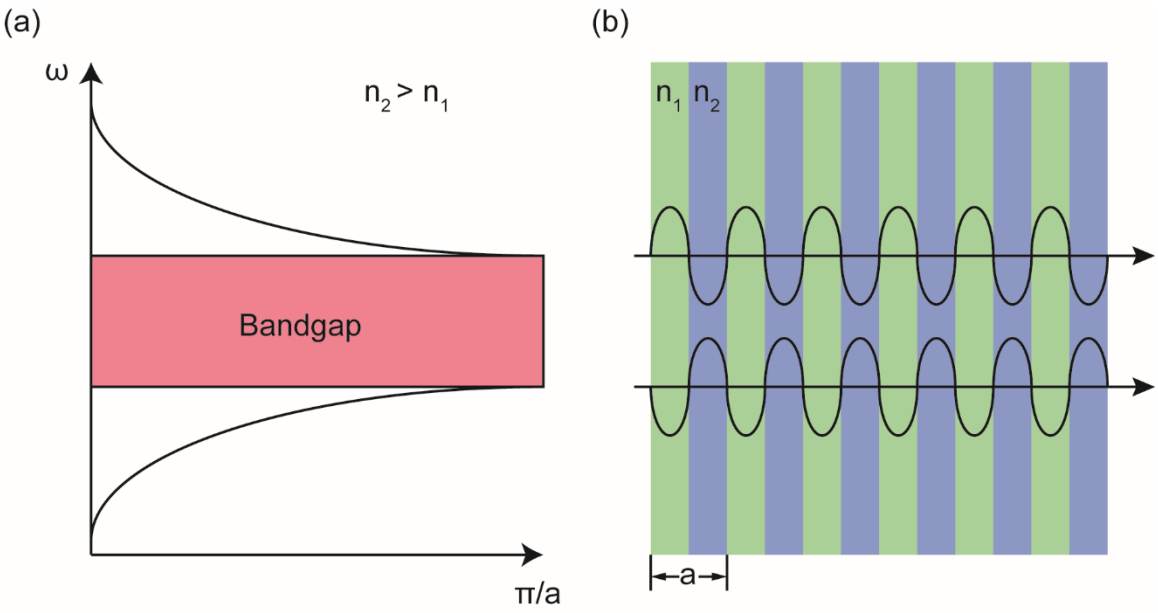

Figure 2-2: The photonic bandgap of a 1D-PhC, where (a) shows the appearance of the bandgap and (b) shows the lower and higher limits of propagation of the wave.

There are two modes of propagation of a wave: Transverse Electric (TE), where electric field does not exist in the direction of propagation and Transverse Magnetic (TM), where magnetic field does not exist in the direction of propagation. In order to have a complete bandgap, there should be a gap for both TE and TM modes. A 2D-PhC made of cylinders has a bandgap for the TE mode whereas a 2D-PhC made of connected lattice with veins has a bandgap for TM mode. Furthermore, when there is a high symmetry in the lattice there is a high probability to have a bandgap. If all three requirements are combined, a complete bandgap is obtained. For example, hexagonal arrays in **Figure 2-3b** have a complete bandgap. The 2D-PhCs have band gaps only in certain directions but 3D-PhCs have complete bandgaps in all directions.

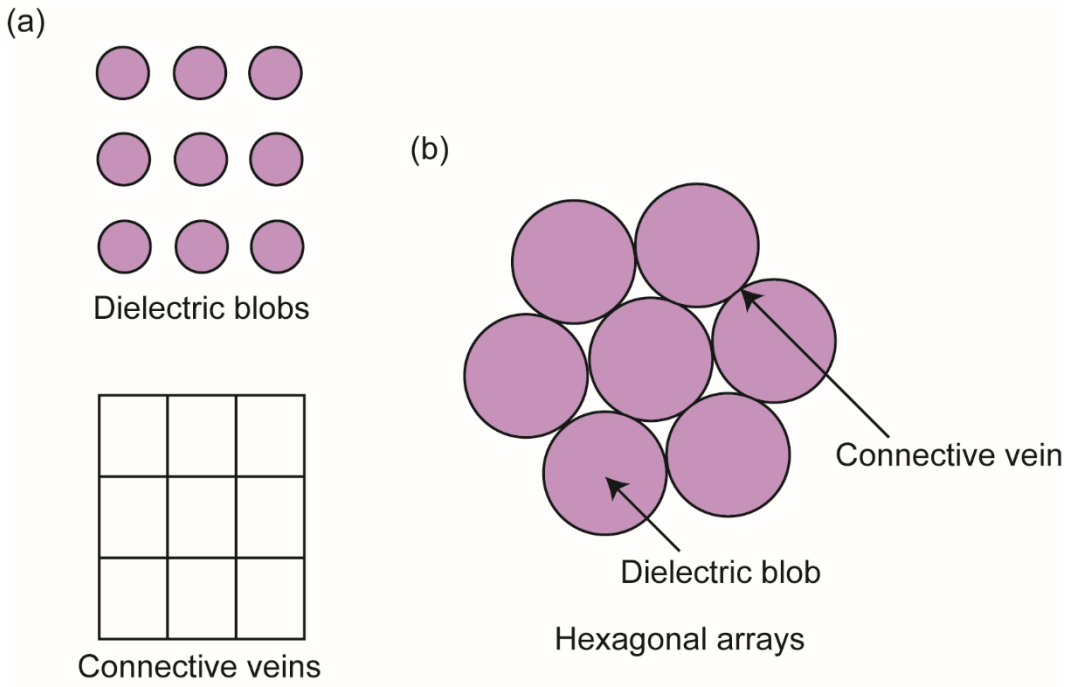

Figure 2-3: Three possible types of 2D-PhCs (a) dielectric blobs (top), connective veins (bottom), and (b) hexagonal arrays. Dielectric blobs have a band gap for TE mode, connective veins have a bandgap for TM mode, and hexagonal arrays have a band gap for both TE and TM modes.

2.4 Light diffraction by Photonic crystals

Electromagnetic radiation with shorter wavelengths, such as X-rays, which pass through an atomic crystal, interfere with the periodicity of atoms, and scatter. If the waves reflected by the crystal planes are in the same phase, constructive interference results, and if they are out of phase destructive interference results. Therefore, waves generate diffraction patterns when passing through an atomic crystal. The diffracted intensities and angles are used to determine the crystal structure, for an instance, in X-ray crystallography. Similarly, PhCs diffract light when the wavelength of the incident light has the same magnitude as the spacing between micro-structures.[73] Consequently, light diffraction is used to study the structure and properties of PhCs.

Bragg's law gives a good approximation to the constructive interference of waves reflected by crystal planes. In contrast to X-ray diffraction, the effective refractive index of the PhCs should be taken into account as it becomes significant for the diffraction of light. To get a better approximation of the reflected wavelength, known as the stopband, Snell's law can be combined with Bragg's law.[72] The waves reflected by a PhC are shown in **Figure 2-4.**

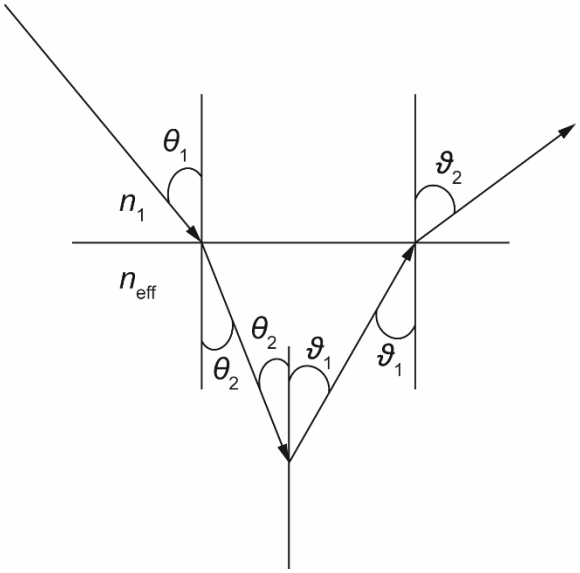

Figure 2-4: Light diffraction by a photonic crystal, where θ_1 is the angle of incident light, θ_2 is the angle of refracted light corresponded to Snell's law, ϑ_1 is the angle of reflected light due to Bragg's reflection, ϑ_2 is the angle of light exiting from the PhC, n_1 is the refractive index of the surrounding environment, and n_{eff} is the effective refractive index of the PhC. (Modified from work published by Baryshev et al.)[74]

Since colloidal particles assemble into fcc structures, the specular reflection of the (111) plane of an fcc lattices is widely used as a model study for the light reflection by 3D-PhCs. According to Bragg's law for a 3D photonic lattice, the wavelength of the reflected wave is given by[74]

$$\lambda = \frac{2dn_{eff}\cos\theta_2}{m} \qquad \textbf{(2-21)}$$

where d is the interplanar distance, θ_2 is the angle of the incident light for Bragg's reflection, n_{eff} is the effective refractive index of the PhC, and m is the order of the incident light. There are many studies that evaluate the lowest order of diffraction, where m =1, by fcc PhCs[75-81] and the above equation is simplified to:

$$\lambda = 2dn_{eff}\cos\theta_2 \quad \textbf{(2-22)}$$

Furthermore, from the Snell's law

$$\frac{\sin\theta_1}{\sin\theta_2} = \frac{n_2}{n_1} \quad \textbf{(2-23)}$$

where θ_1 and θ_2 are the angles measured to the normal at the boundary of the two media with different refractive indices n_1 and n_2, respectively. **Equation (2-23)** can be further simplified by incorporating the air-PhC interface:

$$\sin\theta_2 = \frac{1}{n_{eff}}\sin\theta_1 \quad \textbf{(2-24)}$$

The combination of Bragg's and Snell's law from **equation (2-22)** and **(2-24)** gives[82-84]

$$\lambda = 2d\sqrt{n_{eff}^2 - \sin^2\theta_1}. \quad \textbf{(2-25)}$$

The n_{eff} can be calculated as follows;[85]

$$n_{eff} = n_1\phi + n_2(1-\phi) \quad \textbf{(2-26)}$$

where ϕ is the volume fraction occupied by the medium having a refractive index of n_1. When the angle of incident light is equal to zero and when one substitutes **equation (2-26)** for n_{eff}, **equation (2-25)** becomes,

$$\lambda = 2d[\phi n_1 + (1-\phi)n_2] \quad \textbf{(2-27)}$$

Since Bragg's law assumes equal contribution from all the planes for light reflection and does not encounter the attenuation of light, the dynamic diffraction theory is incorporated into Bragg's equation.[83, 86] The relationship between Bragg's reflection (λ_b) and reflection from dynamic diffraction theory (λ_d) is as follows;[87]

$$\lambda_d = \lambda_b(1 + \frac{\psi}{2}) \quad \textbf{(2-28)}$$

where ψ is

$$\psi = 3\phi\frac{r^2 - 1}{r^2 + 2} \quad \textbf{(2-29)}$$

Here r is the ratio of the refractive indices of the two dielectric materials where

$$r = \frac{n_1}{n_2} \quad \textbf{(2-30)}$$

The combination of **equations (2-27)** and **(2-28)** gives:

$$\lambda = 2d[\phi n_a + (1 - \phi)n_s]\left(1 + \frac{\psi}{2}\right) \quad \textbf{(2-31)}$$

Here, n_1 and n_2 was substituted by the refractive indices of air (n_a) and spheres (n_s) respectively. Since the reflection caused by the (111) planes of an fcc crystal is responsible for its most intense stopband, the interplanar distance d can be related to the size of the spheres (D) to obtain:[88]

$$\lambda = 1.632D[\phi n_a + (1 - \phi)n_s](1 + \frac{\psi}{2}) \quad \textbf{(2-32)}$$

2.5 Self-assembly

Self-assembly is a unique phenomenon, where the objects assemble themselves with specific interactions between each other but without any significant external modification. This phenomenon can be seen everywhere in nature including biological and non-biological environments.[19, 89] In the self-assembly of particles, interactions such as dipole-dipole,[90] depletion,[91-93] or capillary forces[94, 95] control the assembly. Due to the simplicity and inexpensiveness of the process, self-assembly is introduced as a technique for the fabrication of new materials, especially the PhCs.[88, 96-98] Currently, expensive and complex methods, such as chemical vapor deposition,[99] molecular beam epitaxy,[100-102] and lithographic techniques,[97, 103, 104] such as optical,[105] X-ray,[106] scanning probe,[107] nanoimprint,[108] and electron beam,[109] are used to fabricate PhCs.[103, 104] These methods are

not only expensive but also slow and result PhCs limited to a thickness of few layers. In contrast, self-assembly results in PhCs with a thickness of a few to a several hundred layers.

2.6 Opals and inverse opals (IOs) as PhCs

An opal is a type of gemstone composed of silica and it is a well-known example of a natural PhC. The name opal is derived from Sanskrit word "upala," which means precious stone.[110] These gemstones show iridescence when viewed in different angles. This iridescence is due to the periodic close-packed arrangement of silica beads with diameters of several hundreds of nanometers. Microstructures containing close-packed spheres are generally referred to as opals. In the opal, the interstitial sites among the close-packed spheres contain a medium of low refractive index, such as air (n=1). When the refractive indices are reversed, an inverse opal is obtained. The **Figure 2-5** shows a cartoon representation of an opal and inverse opal.

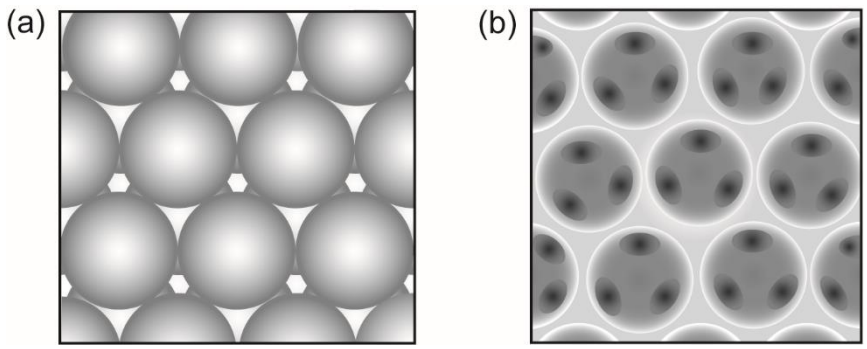

Figure 2-5: Schematic representation of (a) an opal and (b) an inverse opal.

The photonic bandgap is one of the most interesting features of a PhC. A complete bandgap is possible when the propagation of light is forbidden for all states of directions and polarizations. However, some PhCs have incomplete or pseudo band gaps, where the propagation of light is forbidden in only some directions that are sometimes referred to as "stopbands." Theoretically, for opaline structures, a complete band gap is obtained if the contrast of the refractive indices is higher than 2.9 ($n_1/n_2 > 2.9$), which is not possible with most opals. The opals usually have pseudo

bandgaps, whereas complete bandgaps can be easily achieved with inverse opals. Laser resonance cavities, waveguides, inhibitors of spontaneous emission, etc., are good examples for the application of PhCs with complete bandgaps.[111]

2.7 Fabrication of opals and inverse opals

The majority of synthetic opals are made of silica or polymer colloids, where the colloids are arranged into an fcc or hcp crystal and the interstitial sites are usually filled with air.[112] Poly(methyl methacrylate) (PMMA) and polystyrene (PS) polymers are widely used to generate colloids for the fabrication of opals and inverse opal structures.

There are various methods to fabricate opals;[72, 113, 114] of these, sedimentation and evaporative assembly are used frequently. Sedimentation is conducted using gravity or electric fields,[115, 116] and evaporative assembly involves the evaporation of the dispersant of the colloids. Sedimentation methods are good for the fabrication of thick films of opals; whereas, evaporative assembly is good for thin films. The colloids are vertically[117] or horizontally[118] deposited onto a substrate, but horizontal deposition results in opals with uneven thickness. Even though vertical deposition yields a much more uniform colloidal crystal, there are some drawbacks, such as the formation of a thickness gradient and difficulty with the fabrication of thin films with large colloids. These drawbacks can be minimized by controlling the evaporation temperature, applying vertical temperature gradient, mechanical agitation, and isothermal heating. **Figure 2-6a** shows a typical evaporative vertical assembly setup, where a substrate is submerged in a colloidal solution and kept open to the environment for the evaporation of solvent.

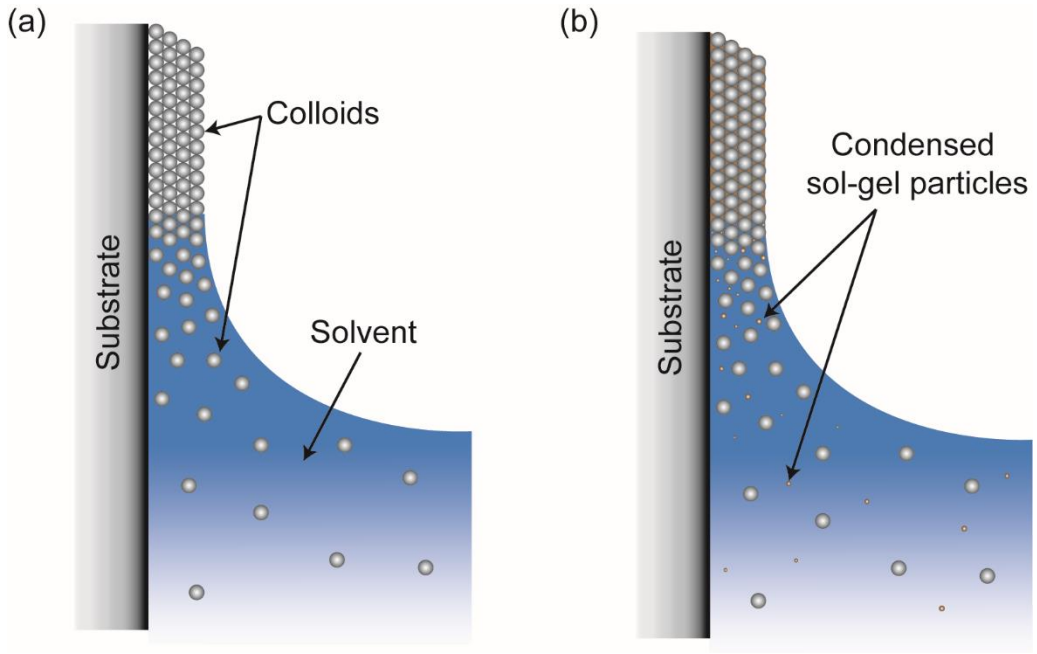

Figure 2-6: Schematic representation of vertical deposition of colloids on a substrate, where (a) is the vertical deposition of colloids and (b) is the co-assembly of colloids.

The inverse opals are made of various materials such as SiO_2,[119] Al_2O_3,[120] TiO_2,[98, 121, 122] CeO_2,[111] GaAs,[123] V_2O_5,[124] and ZrO_2,[88, 125] etc. Even polymers, such as hydrogels, have been used to fabricate inverse opals. Voids of an inverse opal are usually filled with air and the contrast of refractive indices of the matrix and voids determines the properties of the PhC.

Usually, inverse opals are fabricated by infiltrating a sol-gel precursor solution into the interstitials sites of a self-assembled opal, which is condensed and forms a solid after hydrolysis. The solid matrix starts drying as the solvent is evaporated. Next, the template is removed chemically or physically. Various sacrificial templates are used for the fabrication process such as PMMA, PS and silica. Mostly, the silica templates are removed using dilute hydrofluoric acid, and polymer templates by calcination. The calcination not only removes any adsorbed solvent or trapped by-products but also facilitates further condensation of the 3D solid network. Usually, fabrication of inverse opals utilizes sol-gel precursors to build up the matrix. However, the inverse opals made

with conventional infiltration technique have numerous defects. Also, the vertical deposition of colloids itself generates defects, such as polycrystallinity and cracks, which will be transferred to the inverse opal. Moreover, it is difficult to control the amount of the precursor added to the template, which results in poor or over infiltration. So there is a need for a better technique to fabricate inverse opals with a good quality. To improve the quality of inverse opals, research has been conducted on controlled template deposition of colloids, such as assembly of colloids under negative pressure,[126] capillary-enhanced processes,[127] vertical depo-sitions combined with a piezoelectric actuator,[128] etc.

Co-assembly is a simple technique that is used to fabricate Inverse opals with good quality. In co-assembly both colloids and the sol-gel precursor are mixed in the same solution and the self-assembly and infiltration take place simultaneously. Once the process is completed the template is removed.[20] This method reduces the main drawbacks of the infiltration technique, such as the excess or lack of precursor, poor assembly of colloids, and presence of multiple domains. It is reported that the presence of a sol-gel precursor and colloids in the same solution is beneficial as the precursor aids on the assembly of colloids; this results in a single crystalline domain and can be extended to several centimeters in length.[20] **Figure 2-6b** shows a schematic representation of the co-assembly technique.

CHAPTER III

FABRICATION OF DEFECT-FREE INVERSE OPALS WITH VARAIBLE STOPBANDS

3.1 Introduction

Opals and inverse opals, two major types of self-assembled structures, provide good examples of photonic crystals that result from the periodic arrangement of colloids and voids, respectively. Self-assembly techniques continue to be studied as an alternative to lithographic methods because while photonic structures generated by lithographic methods are intricate and functional, the fabrication is cumbersome, time consuming, and expensive.[12-15, 129, 130] Self-assembly is finding application in photonics,[131-133] catalysis,[133,134] sensing,[34, 135] and tissue engineering.[136] Applications of opals and inverse opals in sensing and photonics make use of the structural color that results from the periodicity of the structures. Inverse opal films can be fabricated by filling the interstitial sites of self-assembled colloids with a precursor solution and then removing the template (assembly of colloids) by means of heat or chemical dissolution. The co-assembly is a technique that is used for fabrication of inverse opal films where the colloids and the matrix material (a sol-gel precursor) assemble simultaneously. According to Hatton, et al.,[20] co-assembly reduces defects of the inverse opal structure significantly, resulting in high-quality thin films that have large, ordered domains. This is in contrast to inverse opal films made with the conventional technique, where the self-assembly and infiltration of the sol-gel precursor occur in two consecutive steps, which leads to a significant amount of defects in inverse opals.

Long-range order is required for maximum functionality, but the fundamental issue with the self-assembly of colloids is the cracks associated with the drying process that disrupt periodicity.[137-141] Other defects include the presence of multiple crystal domains, colloid vacancies, and colloidal dislocations. Even though many methods have been proposed to improve the self-assembly technique,[22-24, 142, 143] enhancing the overall quality of the fabricated materials remains challenging. Previous studies have shown that co-assembly can improve upon cracks and yield inverse opals having long-range order in the centimeter length scale.[20]

In this study, the effects of three parameters on the overall quality of the fabricated inverse opals produced by the co-assembly process were investigated. The parameters include varying the concentration of the colloids, the concentration of the sol-gel precursor, and the rate of hydrolysis. Thresholding, a semi-quantitative image analysis technique, was used to assess the defects that result in the fabricated inverse colloidal crystal films with respect to the aforementioned parameters. Our results show that the number of defects reached to a minimum when the concentrations of colloids and tetraethyl orthosilicate were changed to 1.3 mg/mL and 1.9 mg/mL. It was further revealed that the mild hydrolysis of tetraethyl orthosilicate facilitates the reduction of cracks. Also, the position of the stopband was tuned by synthesizing poly(methyl methacrylate) colloids with different sizes for use as templates of inverse opal films.

3.2 Materials and methods

3.2.1 Materials and Instruments

Chemicals were used as received. Methyl methacrylate (99%), ethylene glycol dimethacrylate (98%), ammonium persulfate ($(NH_4)_2S_2O_8$, 98%), 1-dodecanethiol (98%), and tetraethyl orthosilicate (TEOS, 98%) were obtained from Sigma-Aldrich Chemicals (St. Louis, MO). Absolute ethyl alcohol (EtOH), sulfuric acid (H_2SO_4, 95.0-98%), and ACS reagent grade hydrochloric acid (HCl, 36.5-38.0%) were purchased from Pharmco-AAPER (Brookfield, CT).

ACS reagent grade hydrogen peroxide (H_2O_2, 30% (w/w)) was bought from Ricca chemical company (Arlington, TX). Silicon wafers (p-type Si:B[100], R_o = (1-100) Ω cm) were acquired from El-Cat Inc. (Ridgefield Park, NJ) and fused quartz slides were purchased from Technical Glass Products, Inc. (Snoqualmie, WA). Opal films were fabricated on microscope slides (premium) obtained from Fisher Scientific (Fair Lawn, NJ). The surface of the substrates was cleaned using a corona treater (Electro technique products incorporation BD-20). The images of the thin films were taken using a scanning electron microscope (SEM, FEI Quanta 600 FE-ESEM) and light microscope (Olympus IX 83). Particle sizes were measured using both particle size analyzer (Malvern instrument Nano-ZS90) and SEM images. The thin film deposition was carried out in a convection oven (Binder ED 115) and calcination was conducted in a tube furnace (Thermolyne 2110). Transmittance spectra were taken using a UV-Vis spectrophotometer (Cary 50 Bio) in transmittance mode. Image analysis was conducted using Image J 1.48v (Wayne Rasband, National Institutes of Health, USA) and Photoshop CS6 software (Adobe Systems Inc.). All the graphs were plotted using OriginPro 9 software (OriginLab Corporation). Water was deionized at a resistance of 18.1 Ω/cm using a Barnstead Nanopure^{TM} water purification system.

3.2.2 Synthesis of poly(methyl methacrylate) colloids

Poly(methyl methacrylate) (PMMA) colloids were prepared by adding ammonium persulfate (0.100 g) to a flask containing deionized water at 80 °C. After stirring the solution for 1 h, a pre-sonicated mixture of methyl methacrylate (9.25 mL), ethylene glycol dimethacrylate (47.4 µL), and 1-dodecanethiol (23.7 µL) was added and the stirring was continued for 3 h. The resulting colloidal solution was purified by centrifugation. The particle size, zeta potential, and polydispersity index of the colloidal particles were determined using a particle size analyzer (Nano-ZS90, Malvern Instruments). The particle size and the polydispersity of the air-dried polymer colloids were measured using SEM images as mentioned elsewhere.[144, 145] Briefly, random images of PMMA particles placed on a 1 cm × 1 cm silicon wafer were taken and image processing soft-ware (ImageJ)

was used to measure the diameter of the particles. The polydispersity was determined by taking the square of the ratio between the standard deviation and mean particle diameter.

The size of the PMMA colloidal particles was varied by changing the amount of monomer used in the synthesis. The sizes of 298(±15) nm, 354(±14 nm), 391(±13) nm, 438(±15) nm, and 465(±19) nm were obtained for the colloids synthesized by using the respective amounts of the monomer: 4.9 g (5.25 mL), 6.7 g (7.25 mL), 8.6 g (9.25 mL), 10.4 g (11.25 mL), and 12.3 g (13.25 mL).

3.2.3 Preparation of TEOS stock solution

A tetraethyl orthosilicate stock solution was prepared by mixing 0.1 M HCl, ethanol, and tetraethyl orthosilicate in a ratio of 1:1.5:1 (by weight) followed by stirring the mixture for 1 h.

3.2.4 Fabrication of opal and inverse opal films

Both opal and inverse opal films were fabricated either on silicon wafers, glass microscope slides, or fused quartz slides (with dimensions of 10 mm × 50 mm) as necessary. The substrates were cleaned using piranha solution (1:2 mixture of H_2O_2 and H_2SO_4) and treated with a corona treater prior to use. The opal films were fabricated using vertical deposition, where the substrates (silicon wafers and glass slides) were submerged vertically in a dilute colloidal solution and heated in an oven at 65 °C for 20 h. The evaporative co-assembly technique was used for the fabrication of inverse opal films.[20] The co-assembled technique is similar to the fabrication process of the opal films except for the addition of tetraethyl orthosilicate into the colloidal solution. In this study, two sets of inverse opal films were fabricated. The first set of films was fabricated by varying the concentration of colloids at a constant concentration of tetraethyl orthosilicate (1.9 mg/mL). The colloid concentrations were the following: 0.4 mg/mL, 0.7 mg/mL, 1.0 mg/mL, 1.3 mg/mL, and 1.6 mg/mL. For the second set of inverse opal films, the concentration of colloids (1.3 mg/mL) remained constant while the concentration of tetraethyl orthosilicate was varied as follows:

1.0 mg/mL, 1.3 mg/mL, 1.6 mg/mL, 1.9 mg/mL, and 2.2 mg/mL. The resulting co-assembled films (length ~18 mm) were calcined in a tube furnace by heating for 2 h at 500 °C with a 5 h ramping time of 95 °C/h. Opal and inverse opal films were fabricated on glass microscope slides or fused silica glass for evaluation by optical microscopy. Images of the fabricated films were taken using an Olympus IX 83 light microscope with a 20× objective along the direction of fabrication (for *ca*. 1 mm from the top) and stitched together.

3.2.5 Defect analysis of inverse opal films using SEM images

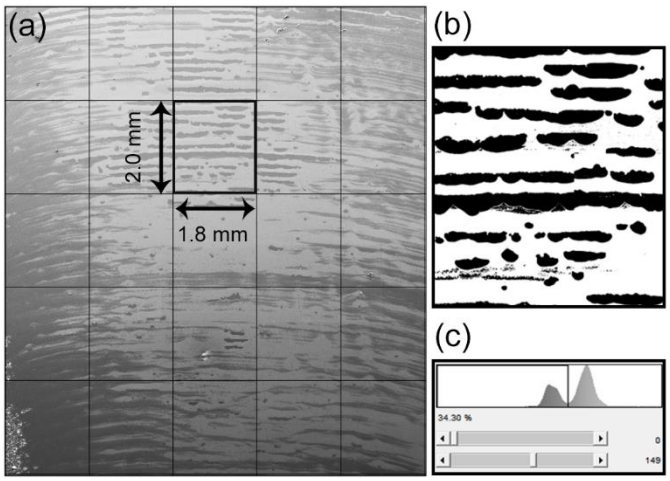

Figure 3-1: Quantification of a defected area using thresholding. (a) An SEM image of an inverse opal film made with 0.4 mg/mL of colloids and 1.9 mg/mL of tetraethyl orthosilicate. The SEM image is stitched to generate an area of 90 mm^2, and then divided into 25 small rectangles (1.8 mm × 2.0 mm). (b) A binary image that represent the area of the small rectangle indicated by the black open square in panel (a); the defects were highlighted in black and the differentiation between the two gray contrasts values was done by adjusting the thresholding window (c).

The use of binary images to analyze defects has precedence in the study of fractures in con -crete. [146, 147] In this study, the SEM images (8-bit) were converted to binary images by thresholding using ImageJ 1.48v (Wayne Rasband, National Institutes of Health, USA). The total defected area

was highlighted by adjusting the thresholding window manually, determined from the "measure" in-built function, and reported as a percentage of the total area. The sample area (90 mm^2) of the inv-erse opal film was selected for the analysis and imaged using SEM (voltage-20 kV, spot size-3.0, magnification-100×, and under the same brightness and contrast). Later, the SEM images were stit-ched together to remove the overlaps and an image of the entire area was obtained (**Figure 3-1**). Next, this image was divided into 25 sections (each having an area of 3.6 mm^2). Each section was analyzed individually and combined to obtain the total area of defects.

3.3 Results and Discussion

3.3.1 Colloidal Assembly

Koh, et al.[148] proposed a mechanism for the self-assembly of colloids, which includes three distinct stages. First, near the pinned contact line of the meniscus, hydrated colloids arrange with a large lattice parameter due to the Derjaguin, Landau, Verwey, and Overbeek (DLVO) potential barrier[148]. As the meniscus recedes, the volume fraction of colloids increases and capillary forces facilitate the nucleation. The second stage arrives as the meniscus passes the first pinned contact line, where the colloids assemble with a lower lattice parameter. At this stage, the solvent is filled into the interstitial sites between the colloids. Finally, solvent at the interstitial sites evaporates, which results in hollow spaces. The sizes of the colloids decrease during the process since the colloids become dehydrated with the evaporation of the solvent.

Table 3-1: Size distribution and zeta potential of PMMA colloids.

	Wet colloids	**Dry colloids**
Size /nm	460(±5)	345(±20)
Polydispersity	0.19	0.06
Zeta potential /mV	58.0(±0.7)	-

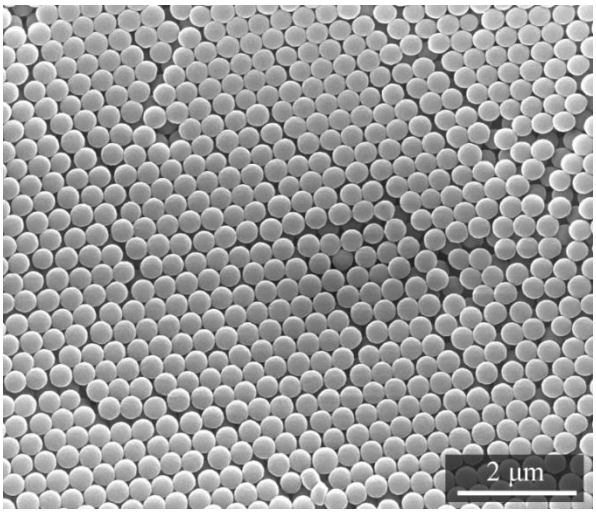

Figure 3-2: Representative SEM image of PMMA particles (345 nm) synthesized by emulsion polymerization.

The colloids used in this study were made out of poly(methyl methacrylate) (PMMA) (**Figure 3-2**). Both the sizes and the zeta potential (ζ) of the colloids were measured to determine the stability of the colloidal suspension. The sizes of the colloids were determined using a particle size analyzer (wet) and SEM images (dry) as mentioned in the procedures. There was a difference of ~100 nm in sizes between the dry and wet colloids (**Table 3-1)**. The polydispersity of dry colloids was calculated from the square ratio of the standard deviation and mean particle diameter. The polydispersity of the dry colloids was 0.06. As previously reported, when the polydispersity of the colloids is lower than 0.07 (dry), better close-packing is observed.[145] As measured by light scattering, the polydispersity index (PdI) of the wet colloids synthesized was ~0.04, which falls in the range of monodisperse colloids (<0.05).[149] A colloidal solution is considered stable when the zeta potential is between ±40 and 60 mV.[150-152] The measured zeta potential of the PMMA colloids synthesized in this experiment was ~60 mV (**Table 3-1**).

3.3.2 Inverse Opals Made by Co-assembly

Co-assembly was used to fabricate the inverse opal films: tetraethyl orthosilicate was used as the sol-gel precursor and PMMA colloids were the sacrificial template. Then, the crystal structure was determined using SEM images. There are two possible crystal structures for a close-packed arrangement of colloids: hexagonal close-packed (hcp) and face centered cubic (fcc). The fcc structure has three distinct alternating layers of colloids or voids stacked in an A-B-C sequence and hcp has an A-B stacking sequence of colloids or voids. Here, the crystal structure of inverse opal films was determined by analyzing the arrangement of voids at a crack, and confirmed to be fcc. Castañeda-Uribe, et al.,[153] previously used a similar analysis to determine the crystal arrangement of an opal film using SEM images. As seen in **Figure 3-3**, three alternating layers were observed in the fabricated inverse opal films, which suggest the A-B-C arrangement of the fcc structure.

The size of the voids of inverse opal films was measured using SEM images and found to be 270(±20) nm. The void size is smaller compared to the size of the dry colloidal template (345 nm). The reduction in the void size is likely caused by the volume expansion of the silica network that results from heating at high temperatures (500 °C) during the calcination process that can deform the PMMA colloids.

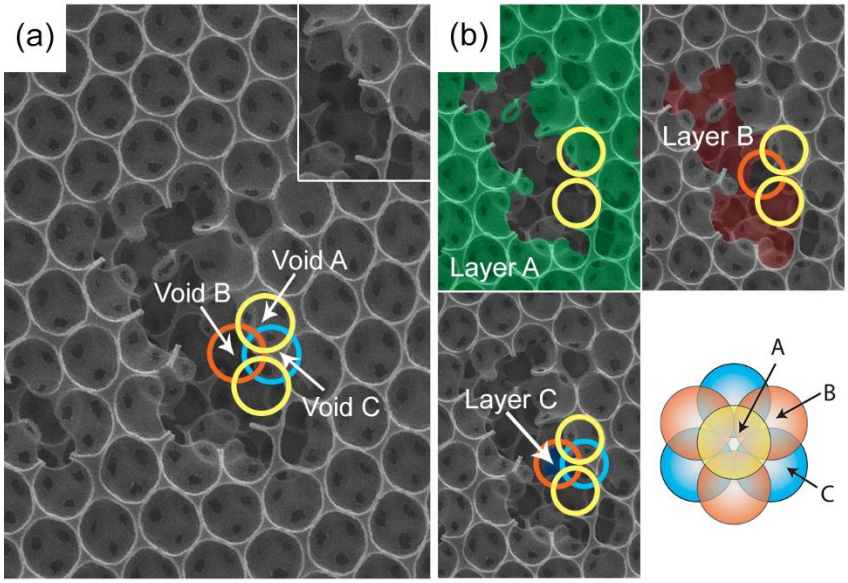

Figure 3-3: (a) An SEM image of an inverse opal film with a crack; the colored circles show the fcc crystal arrangement of voids; the inset shows the area of the crack that was used for the analysis. (b) The layer by layer arrangement of voids confirms the fcc crystal structure of the inverse opal film: green - layer A, red - layer B, and blue - layer C; the diagram (right-bottom) clearly shows the arrangement of voids in the layers is fcc; yellow circles - layer A, orange circles - layer B, and light blue circles - layer C.

3.3.3 Inverse Opal Structures: Effect of Colloidal Concentration

3.3.3.1 Quantification of Defects

In the vertical deposition method, evaporation of the solvent facilitates a convectional flux of colloidal particles towards the thinning region of the meniscus onto the substrate. This region has a high volume fraction of colloidal particles with a low interplanar distance, which ultimately results in the nucleation step in the formation of colloidal crystal. When there is a low concentration of particles, the particles are arranged as a few layers at the pinned contact line of the meniscus. Subsequently, the meniscus recedes to the minimum contact angle that it can possibly have with the substrate and slips to a new pinned contact line with a new contact angle. Since the

concentration of particles is not sufficient, the packing of the colloidal particles can be seen only at regular intervals and the stick-slip bands are created.[154, 155] In co-assembly, a mixture of colloids and a sol-gel precursor is used to produce the colloidal composite; hence both the concentration of colloidal particles and the sol-gel precursor should influence the quality of the resultant inverse opals.

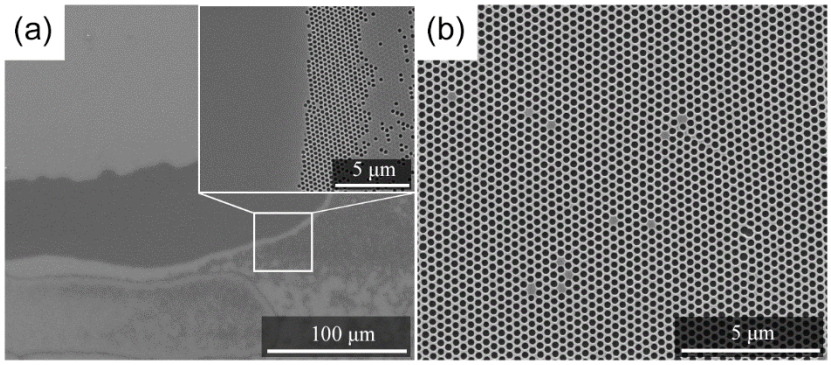

Figure 3-4: SEM images of the types of defects observed in the inverse opal films made by the co-assembly technique. (a) An SEM image showing a stick-slip band (dark contrast) and an overlayer of silica on an inverse opal film (the colloidal template was made with 0.4 mg/mL of colloids and 1.9 mg/mL of tetraethyl orthosilicate). The inset shows a magnified area on an edge of the stick-slip band (the stick-slip band on the left and the overlayer on the right are separated by a close packed arrangement of voids) and (b) a magnified SEM image of the light gray area of (a).

To study the effect of the colloidal concentration on the quality of inverse opal films, a set of inverse opal films was fabricated by changing the concentration of PMMA colloids, from 0.4 mg/mL to 1.6 mg/mL, while keeping the concentration of tetraethyl orthosilicate constant (1.9 mg/mL). SEM was used to analyze the defects in the inverse opal films. Here, defects larger than 1µm that could be easily observed in SEM images taken at a low magnification (100×) are referred to as *macroscopic defects*. The types of *macroscopic defects* found in the inverse opal films made by co-assembly include stick-slip bands, overlayers, and cracks. Stick-slip bands are areas where there is no assembly of colloids (for direct opals) or voids (for inverse opals). Overlayers are the areas

where a thin layer of silica is deposited on the top surface of the close-packed voids. Stick-slip bands and overlayers can be identified in the SEM images since they appear dark gray in contrast, whereas closely packed voids appear light gray (**Figure 3-4**). The dark gray area shown in **Figure 3-4a** is a stick-slip band where an area of non-colloidal assembly is surrounded by close-packed voids (a magnified area is shown in the inset). The light gray area has well-ordered voids, and overlayers are present in some places.

According to previous studies, defects can be analyzed by differentiating segments of gray values using binary images.[146, 147, 156] In these binary images, the defected area is highlighted in black while the rest is in white. As mentioned earlier, in the SEM images of the inverse opals, the defects appear dark gray while defect-free areas appear in light gray. Since it is not possible to differentiate the stick-slip bands from the overlayers, defects as a whole were quantified using image analysis. To differentiate the segments of gray values (dark and light contrast) the SEM images of the inverse opals were converted to binary images using the thresholding method. For this analysis, an area of 90 mm^2 was selected from the top of each the inverse opal film (see **section 3.2.5** and **Figure 3-1a** for more details). The number of defects was reported as a percentage of the total area that was analyzed (90 mm^2).

As depicted by the graph in **Figure 3-5e**, at low concentrations of colloids (0.4 mg/mL and 0.7 mg/mL), more than 46% of the total area of the inverse opal films is defected. The percentage of the defected area increased up 77% at a colloidal concentration of 0.7 mg/mL and reached ~1% at 1.3 mg/mL. Even though the percentage of defects was ~1% at high colloidal concentrations (1.3 mg/mL and 1.6 mg/mL), triangular-shaped cracks were observed in the inverse opal films at 1.6 mg/mL. The cracks, mostly observed at the bottom of the thin film, originated from the edges and propagated toward the center **(Figure 3-6)**.

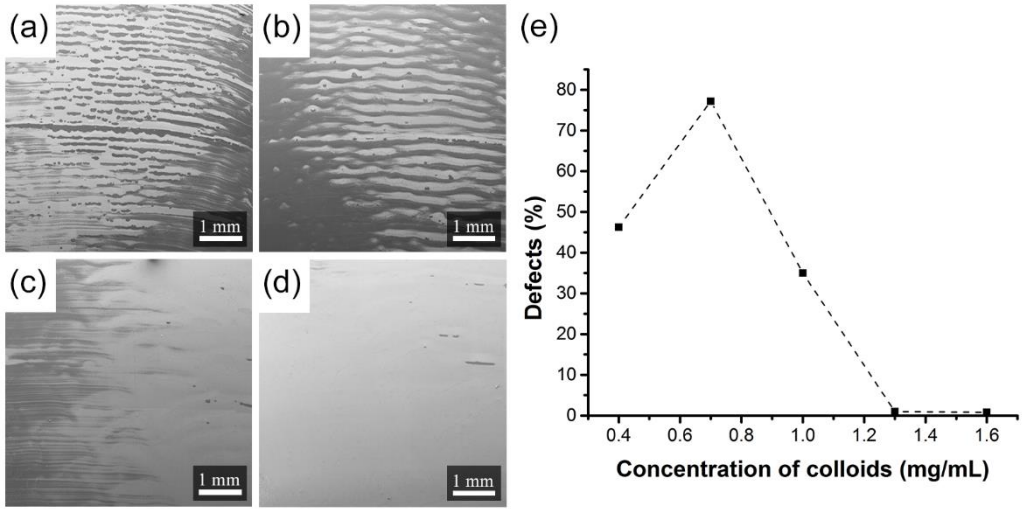

Figure 3-5: Stitched SEM images of inverse opal films made with PMMA colloids (345 nm) of different concentrations: (a) 0.4 mg/mL, (b) 0.7 mg/mL, (c) 1.0 mg/mL, and (d) 1.3 mg/mL. The concentration of colloids was varied, while keeping the concentration of tetraethyl orthosilicate constant (1.9 mg/mL). (e) Graph of the percentage of defects (analyzed using thresholding of SEM images) as a function of the concentration of colloids.

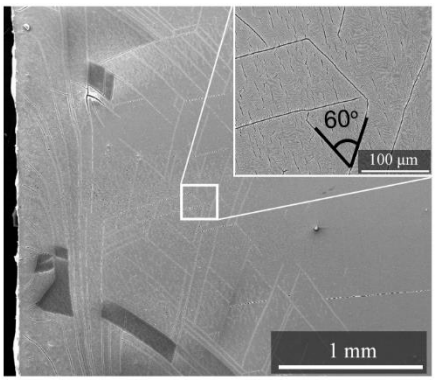

Figure 3-6: An SEM image (100×) of an inverse opal film made with 1.6 mg/mL of colloids and 1.9 mg/mL of tetraethyl orthosilicate. The inset showing a triangular shaped crack is obtained at a higher magnification (1000×). The images were taken at the bottom of the thin film.

3.3.3.2 Crystal Orientation

The (111) plane of an fcc crystal of an inverse opal film has voids arranged in a hexagonal pattern parallel to the substrate.[27, 157] Hatton, B. et al., reported that even though the expected growth direction is <112>, inverse opals has preferential growth along <110> direction. The SEM images shown in **Figure 3-7** verified that inverse opals made with a high concentration of colloids (>1.3 mg/mL) growth along <110> family of planes (red color arrow in **Figure 3-7b**).[20] We have observed a mix of <112> and <110> growth directions (**Figure 3-7a**) when low colloidal concentrations (<1.3 mg/mL) were used in the fabrication process, but when the concentration increases (>1.3 mg/mL) the crystal preferentially grows along the <110> direction. Further analysis was conducted using 2D Fast Fourier Transform (2D-FFT), and from the analysis, it is clear that the top plane of the inverse opal films is (111) and the hexoganal pattern of spots indicate the long-range of order of the inverse opal film (insets, **Figure 3-7a** and **b**).

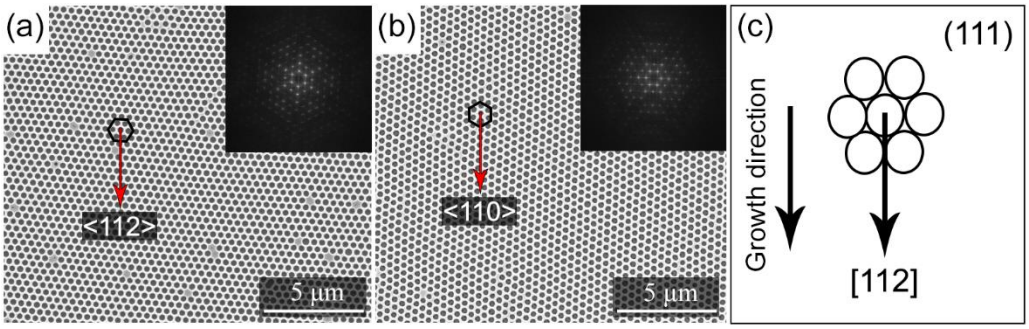

Figure 3-7: Magnified SEM images of inverse opal films made by using (a) 0.7 mg/mL of colloids and (b) 1.3 mg/mL of colloids, where insets represent the FFT images of the particular SEM image. Red arrows show the growth direction of the respective colloidal crystal. (c) A schematic representation of orientations of voids in the (111) plane along the growth direction of colloids; the expected growth direction is [112].

3.3.3.3 Spectrophotometric Analysis

When an inverse opal film is exposed to the visible range of electromagnetic radiation, the specific wavelength of the reflected light is known as the stopband. Since inverse opal films have an fcc crystal structure, and the top surface has a (111) crystal plane, the most intense stopband is due to the reflection of light from (111) planes, which determines the color of an inverse opal film. If the inverse opal is polycrystalline then other planes can also contribute to the color of an inverse opal film. For an example, the final color of an inverse opal film can be a mix of reflections of light from the (111), (220), (200) and (311) planes.[88] The stopband due to the reflection from the (200) planes are less intense, and the peak appears close to the main (111) diffraction, mostly it is indistinguishable in the spectrum. [158] The position and the shape of the stopband are useful to determine the quality of the inverse opals. The wavelength of a stopband of a photonic crystal is related to the interplanar distance by the following equation,

$$\lambda = \frac{2d_{hkl}}{m}[\phi n_v + (1-\phi)n_m] \qquad \textbf{(3-1)}$$

which is a combination of Bragg's law and Snell's law. Here, λ is the wavelength of the stopband, d_{hkl} is the interplanar distance between two crystal planes, m is the order of the incident light, ϕ is the volume fraction of the matrix (silica), n_m is the refractive index of the matrix, and n_v is the refractive index of voids (air). Since the most intense stopband is due to the reflection of light from the (111) plane of the fcc crystal, d_{hkl} can be related to the void size (D) and the following equation can be obtained for the first order reflection.

$$\lambda = 1.632D[\phi n_v + (1-\phi)n_m] \qquad \textbf{(3-2)}$$

The wavelength of the stopband can be varied by tuning the interplanar distance (d) or the volume fraction of the voids (ϕ). The interplanar distance depends on the size of the voids and the close-packed arrangement of voids. The stopband wavelength of our inverse opal films was calculated, from the **equation (3-2)**, using the following parameters: volume fraction of 0.74 (for a perfect

close-packed inverse opal crystal), interplanar distance of 260 nm, and the refractive index of 1.459 for silica and 1.000 for air. Here, the interplanar distance was measured from the cross section of an inverse opal film, which shows spheroidal voids resulting from the anisotropic shrinkage of silica during calcination.[159] The interplanar distance was measured along the minor axis of voids. According to the calculation, the stopband should be positioned at 580 nm; however, a shift in the stopband was observed when the concentration of colloids was varied. **Figure 3-8** demonstrates the transmittance spectra of inverse opal films made with colloids at different concentrations (0.4 mg/mL to 1.6 mg/mL) and 1.9 mg/mL of tetraethyl orthosilicate. At the colloidal concentrations of 0.7 mg/mL and 1.3 mg/mL, the stopband was observed at 605 nm and 550 nm, respectively. Further increasing the colloidal concentration to 1.6 mg/mL shifted the stopband to 595 nm. The inverse opal film made using 0.4 mg/mL of colloids did not show any stopband at all due to poor packing of the colloids. Quasi-amorphous assemblies show an angle-independent stopband while amorphous assemblies do not show any stopband at all.[160, 161] The crystallinity of the inverse opal films was further confirmed by the angle dependency of the stopband where the stopband is blue shifted as the angle of incident wavelength increases.[153] The transmittance spectra of all the inverse opal films showed an angle dependency, which indicates a close-packed arrangement of colloids. The quality of the inverse opal structure can be evaluated in terms of the width of the stopband and the intensity. The wider the band, the greater is the influence of the adjacent wavelength to the reflected color, leading to a mixing of colors. The width of the stopband increases as a result of inhomogeneity of the d-spacing or the refractive index of the crystal. Inhomogeneity of the d-spacing reduces with the increments of the concentration of the colloids and increases again after 1.3 mg/mL. The inverse opal films made with 1.3 g/mL gave the narrowest stopband with the highest intensity indicating the best quality.

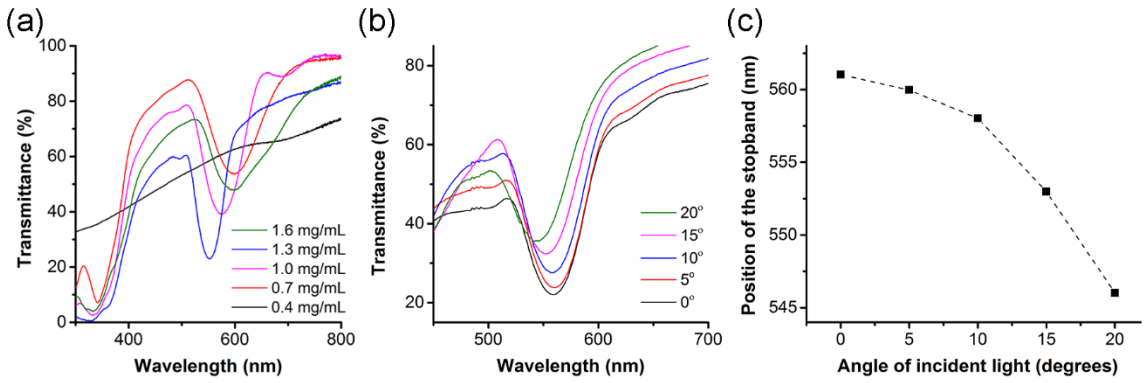

Figure 3-8: (a) Transmittance spectra of inverse opal films made with colloids at different concentrations (0.4 mg/mL, 0.7 mg/mL, 1.0 mg/mL, 1.3 mg/mL, and 1.6 mg/mL) and 1.9 mg/mL of tetraethyl orthosilicate; (b) the transmittance spectra of an inverse opal film made with 1.3 mg/mL of colloids and 1.9 mg/mL of tetraethyl orthosilicate with different angles of incident light; (c) A graph showing the position of the stopband at different angles of incident light (for an inverse opal film made with 1.3 mg/mL of colloids); the stopband blue-shifted as the angle of incident light is increased.

To determine the effect of the colloidal concentration itself to the position and the shape of the stopband, by decoupling the effect from tetraethyl orthosilicate, a series of opal films were made by varying the concentration of colloids (0.7 mg/mL, 1.0 mg/mL, 1.3 mg/mL, 1.6 mg/mL, and 1.9 mg/mL). As previously reported, the thickness of the opal films increases with the concentration of colloids.[117, 162] For opal films, an increase in the intensity of the stopband is expected with the increase in the number of layers of colloids.[163] However, as seen in **Figure 3-9**, the intensity of the stopband increases with the concentration of colloids up to 1.6 mg/mL of colloids and then decreased. When the concentration of colloids exceeded 1.3 mg/mL, cracks were evident at the bottom of the thin film and, with further increments in the colloidal concentration, the cracks started to propagate toward the top of the film. The formation of cracks might be the reason for the reduction of the intensity of the stopband at 1.6 mg/mL of colloids. Furthermore, no significant

shift was observed in the wavelength of the stopband obtained for the opal films (**Figure 3-9a**); hence the shift of the wavelength of the stopbands of the inverse opal films made using different concentrations of colloids is due to the defects introduced at a later stage of fabrication. As well, the width of the stopbands was found to be more or less the same for all the opal films. From **Figure 3-8** and **Figure 3-9**, we can conclude that the shifts and the variations of the stopbands recorded for the inverse opal films were caused by the poor quality of some inverse opal films but not by the variation of the thickness resulting from different concentrations of colloids.

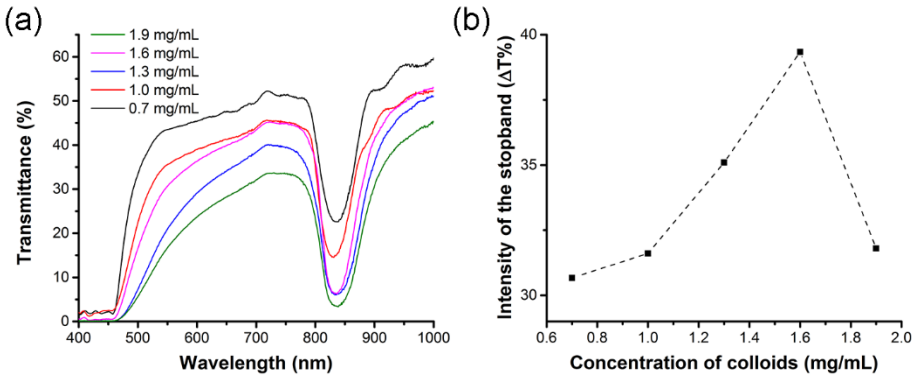

Figure 3-9: (a) Transmittance spectra for the opal films made by changing the concentration of colloids (0.4 mg/mL, 0.7 mg/mL, 1.0 mg/mL, 1.3 mg/mL, 1.6 mg/mL, and 1.9 mg/mL). (b) A graph that shows the variation of the intensity of stopbands of opal films based on the concentration of colloids (the concentrations of colloids are the same as mentioned in (a)).

3.3.4 Inverse Opal Structures: Effect of Tetraethyl Orthosilicate

3.3.4.1 Analysis of Defects

For this part of the study, a set of inverse opal films were prepared by changing the concentration of tetraethyl orthosilicate in the working solution as 1.0 mg/mL, 1.3 mg/mL, 1.6 mg/mL, 1.9 mg/mL, and 2.2 mg/mL. The concentration of colloids was maintained constant at 1.3 mg/mL, since it was determined to result in fewer defects (for more details refer **Section 3.3.3.1**). The

fabricated inverse opal films contained cracks, but were free of stick-slip bands and overlayers, which were the main types of defects observed in the inverse opal films when the concentration of colloids was varied.

As shown in **Figure 3-10**, two main types of cracks, which were classified as microscopic and macroscopic, were observed. The microscopic cracks were shorter than 10 µm and visible only at high magnifications (>15,000× – insets of **Figure 3-10**), whereas the macroscopic cracks were larger than 100 µm and visible even at low magnifications (<100×). As concentration of tetraethyl orthosilicate increased, the shape of the macroscopic cracks was changed. At low concentrations of tetraethyl orthosilicate (1.0 mg/mL), a partially connected network of cracks (**Figure 3-10a**) was observed and the network became fully connected as the concentration of tetraethyl orthosilicate was increased (**Figure 3-10b**). Furthermore, the area between two branches of the network broadened with an increase in the concentration of tetraethyl orthosilicate. Once the tetraethyl orthosilicate concentration reached an optimum value (1.9 mg/mL) cracks were completely disappeared.

Quantification of defects (cracks) was done using the same method mentioned in **section 3.3.3**. Both macroscopic and microscopic cracks decreased with increasing tetraethyl orthosilicate concentration. **Figure 3-11** shows an SEM image of a highly defective inverse opal film: the concentration of tetraethyl orthosilicate is 1.0 mg/mL and the concentration of colloids is 1.3 mg/mL. Since most cracks were < 2µm in width, at low magnifications most of these cracks were barely seen. Therefore, only the area of macroscopic cracks can be measured from the image analysis (thresholding). When the SEM images were taken at high magnifications (16,000×), voids interfered with thresholding; hence, for this analysis only images taken at a low magnification (100×) were used. The defects were highest at lowest concentration of the tetraethyl orthosilicate and reduced as the tetraethyl orthosilicate concentration increases.

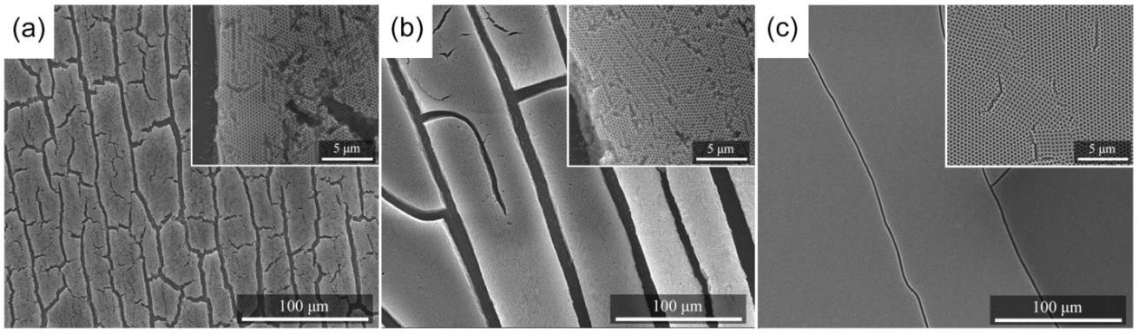

Figure 3-10: SEM images of the types of defects seen in the inverse opal films made by using different concentrations of tetraethyl orthosilicate. The colloidal concentration was constant at 1.3 mg/mL). SEM images of inverse opal films prepared at (a) 1.0 mg/mL, (b) 1.3 mg/mL, and (c) 1.6 mg/mL of tetraethyl orthosilicate. The insets represent higher magnified images (16,000×) of (a), (b), and (c).

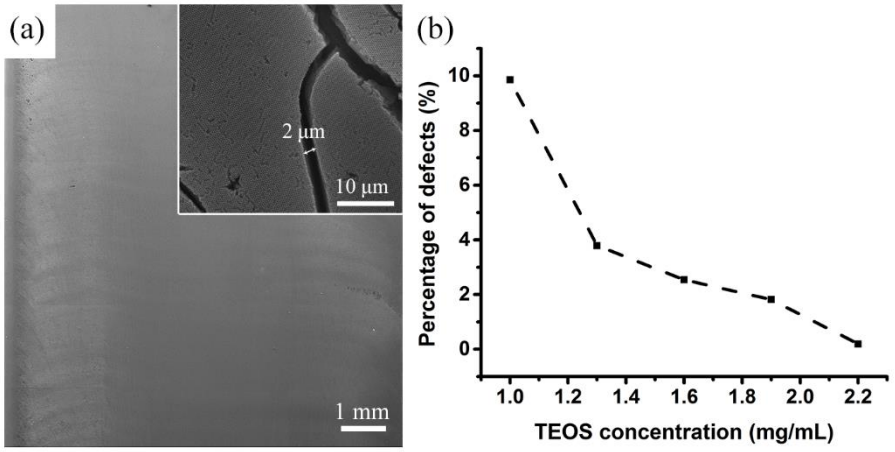

Figure 3-11: (a) An SEM image of an inverse opal film made with 1.0 mg/mL of tetraethyl orthosilicate and 1.3 mg/mL of colloids. The inset shows a magnified area of the inverse opal film. (b) The graph of percentage of defects (analyzed using SEM images) vs the concentration of tetraethyl orthosilicate.

The study was further extended to explain the formation of cracks in the inverse opal films made by co-assembly. According to the previous studies, factors such as particle size,[164] chemical composition,[165, 166] relative humidity,[167] film thickness,[168, 169] temperature,[170] etc., are important to control the shape and the size of the cracks. It was further reported that there is a critical film thickness to be free of cracks.[171] As reported by Lazarus and Pauchard,[171] when the thickness increased beyond the critical thickness, the type of cracks changed, from isolated junctions to sinuous cracks, to partially connected network, to fully connected network, to delamination, and to spiral cracks that were observed at the highest thickness. Since the parameters such as temperature, particle size, and relative humidity were not changed in our study, the thickness of the film was assumed to have a major effect on cracks. According to our results, the cracks present in the inverse opal films changed depending on the tetraethyl orthosilicate concentration, which suggests an influence of tetraethyl orthosilicate concentration towards the film thickness. Therefore, it is important to investigate the effect of the concentration of tetraethyl orthosilicate on the thickness of the inverse opal films and thereby on the formation of cracks.

The color of a thin film depends on the thickness.[172] Since the transparent thin films can undergo constructive interference with the waves reflected by front and back surfaces, thin films with thickness gradient will have set of colors.[172] The **Figure 3-12a** shows a set stitched optical microscopy images of inverse opals films made with varying concentrations of tetraethyl orthosilicate. The images were taken for ~1 mm distance from the top and cover an area of ~0.2 mm^2. The differences in the color indicate that the thickness of the inverse opal films changes with the concentration of tetraethyl orthosilicate.

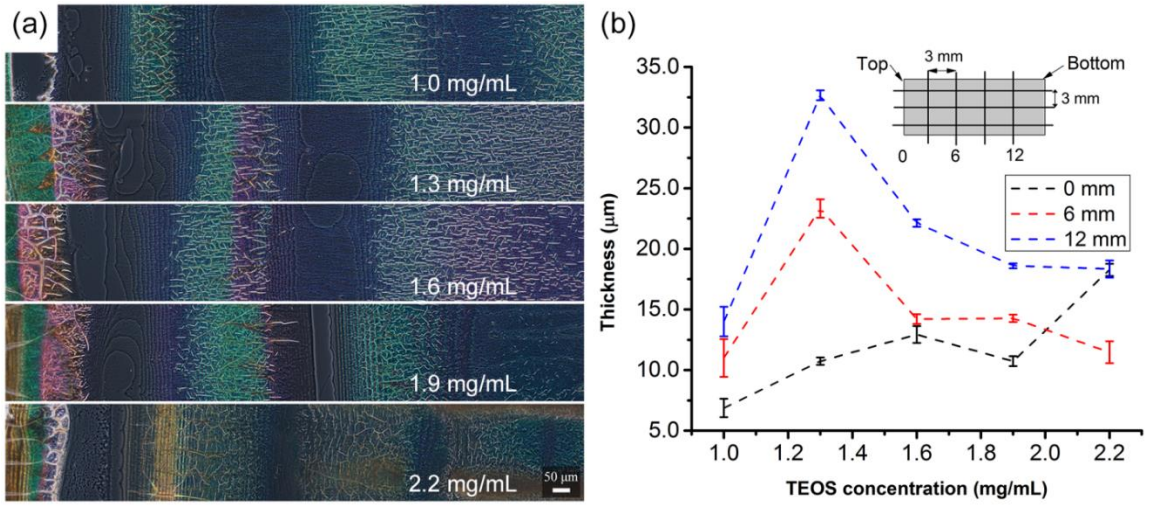

Figure 3-12: (a) Stitched light microscopy images of the inverse opal films made by changing the concentrations of tetraethyl orthosilicate, the images obtained for ~1 mm distance from the top of the film were stitched to acquire the large images (growth direction of the films are left to right); the different colors are due to the variation of the thickness of the inverse opal films; (b) variation of the thickness measured by a light microscope for 3 mm intervals, where only the 0 mm (starting point – top of the film), 6 mm and 12 mm were plotted; the inset shows an inverse opal film with imaginary horizontal and vertical lines and the thickness was measured at the intersections of the lines**.**

The thickness of the inverse opal films made with varying concentration of tetraethyl orthosilicate was measured using a light microscope with Z-stacking capability (OLYMPUS IX83). The thickness measured using Z-vertical displacement is not accurate. As shown in **Figure 3-12b**, the thickness was measured at 0 mm, 6 mm, and 12 mm distances from top along the growth direction. As previously reported for colloidal crystals, the thickness of the thin film gradually increases along the growth direction due to the development of a concentration gradient of colloids over the fabrication period.[173, 174] This explains the higher thickness at the bottom of the of the inverse opal films. However, in most of the inverse opal films, only a slight increase was observed in the thickness as the color of the film did not change significantly over a short distance. In contrast to

the films fabricated at other concentrations, the inverse opal film made at 1.3 mg/mL of tetraethyl orthosilicate showed a notable increase in the thickness (**Figure 3-12b)**. The film thickness increased when the tetraethyl orthosilicate concentration increased from 1.0 mg/mL to 1.9 mg/mL which was confirmed by the different colors of the thin films. Even the cracks were seen at different thicknesses and the areas that have the same color showed the cracks with a similar morphology. The bluish-green area had very few cracks as seen in the micrographs. As depicted by the graph in **Figure 3-12b**, as the concentration of tetraethyl orthosilicate increased, the film thickness reached to a maximum and then decreased at the 6 mm mark. The highest thickness (~22.5 μm) was recorded at 1.3 mg/mL of tetraethyl orthosilicate, then decreased to ~15.0 μm at 1.6 mg/mL and remained the same upon reaching 1.9 mg/mL. Further increase in tetraethyl orthosilicate concentration slightly decreased the thickness of the film (~11.0 μm at 2.2 mg/mL).

At 1.9 mg/mL of tetraethyl orthosilicate, the inverse opal films did not have cracks. Thus, the corresponding thickness of ~15.0 μm can be considered as the critical thickness. A slight increase in the thickness beyond its critical value causes the formation of partially connected cracks in the inverse opal films.[171] As described earlier, the inverse opal films prepared at 1.0 mg/mL of tetraethyl orthosilicate had partially connected networks of cracks; but the film thickness was less than the critical value (~15.0 μm) (**Figure 3-12b**).

Cracks are generated in inverse opal films as a result of volume shrinkage caused by the evaporation of the dispersant during the drying process.[174] It is also reported that the drying rate can significantly affect the stress applied to the thin film yielding cracks, where a slow drying rate yields few cracks.[175] As seen in the **Figure 3-13**, in the inverse opal films prepared in this study, the cracks were propagating along the direction of the assembly. As well, more cracks can be found near the edges of the inverse opal film than in the center. Formation of more cracks near the edges and the

origination of cracks from the edges might be associated with the faster drying rate at the edges. Moreover, the high amount of cracks in inverse opals made of low concentrations of tetraethyl orthosilicate can be explained as follows; during the calcination process, tetraethyl orthosilicate acts as the binding agent between colloids. At low concentrations, the amount of tetraethyl orthosilicate is not sufficient to hold the colloids in place. Lack of binding agent applies an additional stress on the inverse opal films causing the cracks. As well, when the binding agent is insufficient, the colloids tend to be close to each other. The center-to-center distance of voids in the inverse opal films proves this. At low concentrations of tetraethyl orthosilicate, the center-to-center distance of voids (obtained from top surface view of inverse opals) was ~380 nm which is less than the ~400 nm, the center-to-center distance observed in the films with minimal defects where the tetraethyl orthosilicate was sufficient to keep the colloids in place.

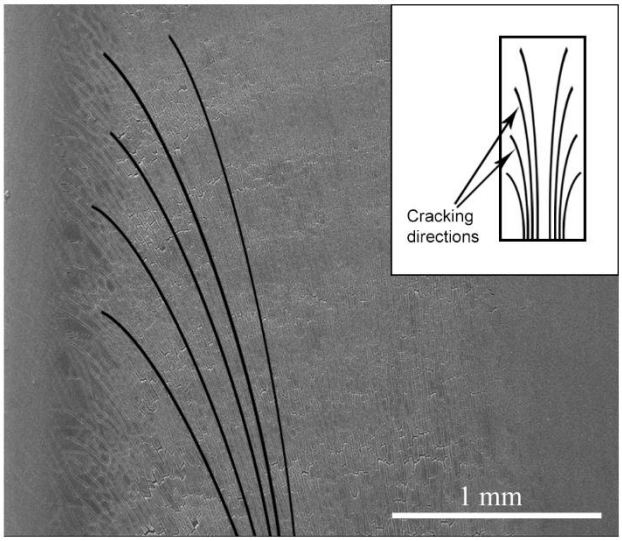

Figure 3-13: An SEM image of an inverse opal film taken at a low magnification showing the propagation of cracks in the inverse opal films and the inset shows the direction of cracks.

3.3.4.2 Crystal Orientation

Another interesting feature that was observed with changing tetraethyl orthosilicate was the change in the growth direction of the colloidal crystal. The prominent crystal growth orientation at low

concentrations of tetraethyl orthosilicate showed a mix of <110> and <112>, and the <110> direction became prominent at high concentrations of tetraethyl orthosilicate (above 1.9 mg/mL). As a consequence of shifting growth directions between different orientations (i.e. <110> and <112>), at low concentrations of tetraethyl orthosilicate, the inverse opal films showed a large number of domains. As seen in the SEM image in **Figure 3-13**, the area between two large domains consisted of many small domains that had different orientations (the black arrows indicate the growth direction of individual domains). In **Figure 3-13** the two major domains with the prominent growth direction of <110> are separated by the dark line whereas the gray lines separate the small domains with different orientations.

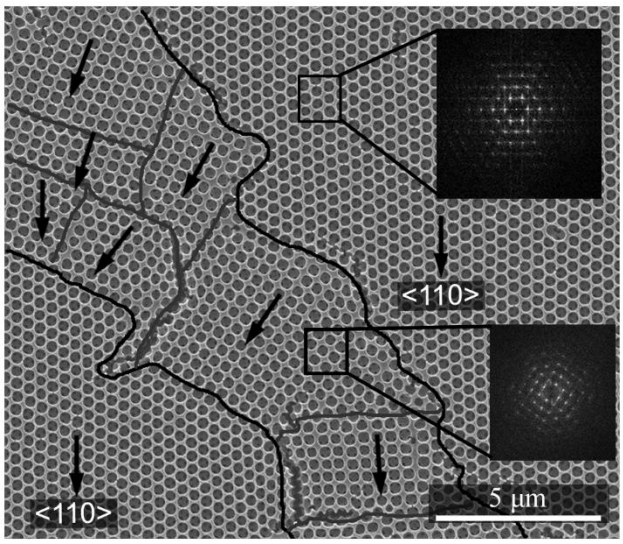

Figure 3-14: An enlarged SEM image showing the domains with different orientations. Insets show the FFT images of selected areas.

Other than shift in the crystal growth direction, square arrays were observed in some places (middle region of **Figure 3-14).** The hexagonal arrays are the most favorable assembly of colloids in a colloidal crystal. However, a study published by Cong and Cao showed that under low

temperatures (< 50 °C) and in the presence of surfactant considerable amount of square arrays is produced.[173] According to their study, the square arrays were formed as a result of restrained free motion of particles at low temperatures and low surface tension due to surfactants. In our study, we have used the same PMMA particles (345 nm), colloidal concentration, and fabrication conditions (e.g. temperature) except for the concentration of tetraethyl orthosilicate. Moreover, these square arrays were seen in the inverse opals made with low concentrations of tetraethyl orthosilicate. Therefore, in co-assembly, the sol-gel precursor concentration plays an important role in the arrangement of colloids.

3.3.4.3 Spectrophotometric Analysis

According to the **Figure 3-15**, when the concentration of tetraethyl orthosilicate has increased the stopband was blue shifted up to 1.6 mg/mL and then red shifted after 1.9 mg/mL. The shift of the stopband might be due to the changes in the lattice parameters caused by the poor close packing at low concentrations. The inverse opal films made using low concentrations of tetraethyl orthosilicate had a large number of defects. The intensity of the stopbands was increased with increasing tetraethyl orthosilicate concentration. The decrease in the intensity of the stopband must have an influence from the scattering of light due to cracks. Even though the stopbands appeared at an almost the same wavelength in both inverse opal films made from 1.9 mg/mL and 1.6 mg/mL of tetraethyl orthosilicate, the latter had more cracks and a less intense stopband compared to the former. Furthermore, the inverse opal film made with 2.2 mg/mL had the most intense stopband due to the presence of the least amounts of defects.

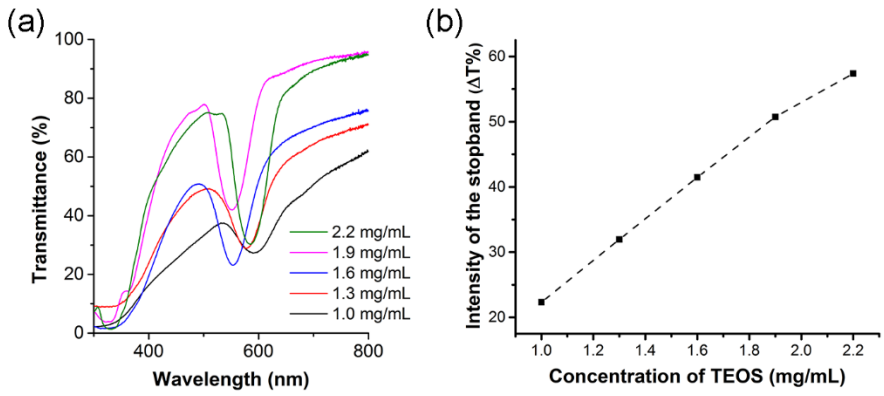

Figure 3-15: (a) Transmittance spectra of inverse opal films made with tetraethyl orthosilicate at different concentrations (1.0 mg/mL, 1.3 mg/mL, 1.6 mg/mL, 1.9 mg/mL, and 2.2 mg/mL) and 1.3 mg/mL of colloids. (b) A graph that shows the variation of the intensity of stopbands of inverse opal films based on the concentration of tetraethyl orthosilicate (the concentrations of tetraethyl orthosilicate are the same as mentioned in (a)).

3.3.5 Microscopic Defects Analysis

In this analysis, several types of defects were considered as *microscopic defects*. A point that is displaced from or inserted into an irregular spot in a crystal lattice is called as a point defect.[176] There are several types of point defects: insertion of an impurity atom into a lattice point, vacancy, insertion of an extra atom to the lattice, and insertion of an impurity atom to an interstitial site. Since the inverse opal films were fabricated by using a colloidal lattice, similar types of point defects can be present in the inverse opal films. In the inverse opal films, the voids act as the lattice points and the absence, misplacement, or difference in the size of voids are considered as point defects. Here, the absence of a void was counted as a vacancy (V) and a void of which the size significantly deviated from the average size was analyzed as a size defect (S). Also, the voids that were shifted in positions were considered as dislocations (L). The dislocations were usually found in places where the grain boundaries were present. The collapse of the wall between two voids was

recognized as a wall defect (W). The cracks propagated along the surface of the thin film were identified as surface cracks (C) and the cracks penetrated deep into the film were counted as deep cracks (D). When analyzing the cracks, the length was manually measured and reported as the approximate values. **Figure 3-16** shows the type of microscopic defects seen in the inverse opal films.

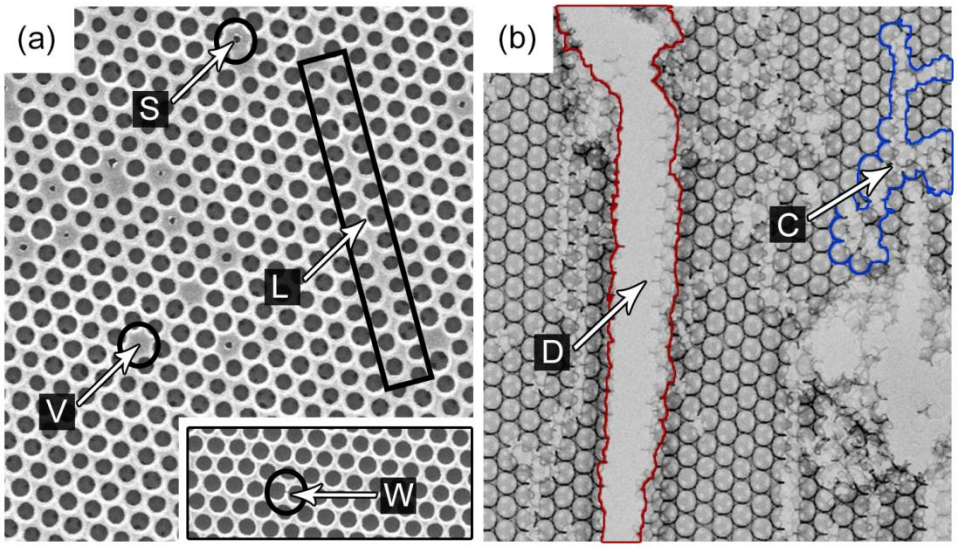

Figure 3-16: Types of *microscopic defects* found in the inverse opal films: (a) void defects (**V**), size defect (**S**), dislocations (**L**), and wall defects (**W**) and (b) surface cracks (**C**) and deep cracks (**D**).

The analysis of *microscopic defects* was conducted using SEM images taken at 16,000× and the defects were calculated from ImageJ software. The defects were reported as the defect density (the number of voids per unit area). To evaluate the size defects (S), the size of voids was measured using the "analyze particle" option in the ImageJ software. The outliers were identified for a series of void sizes and considered as defective voids (or size defects). The maximum possible area of a void is 0.095 μm^2 (as the size of colloids is 0.345 μm). Therefore the higher and lower limits for the determination of outliers were set to 0.110 μm^2 and 0.040 μm^2, respectively.

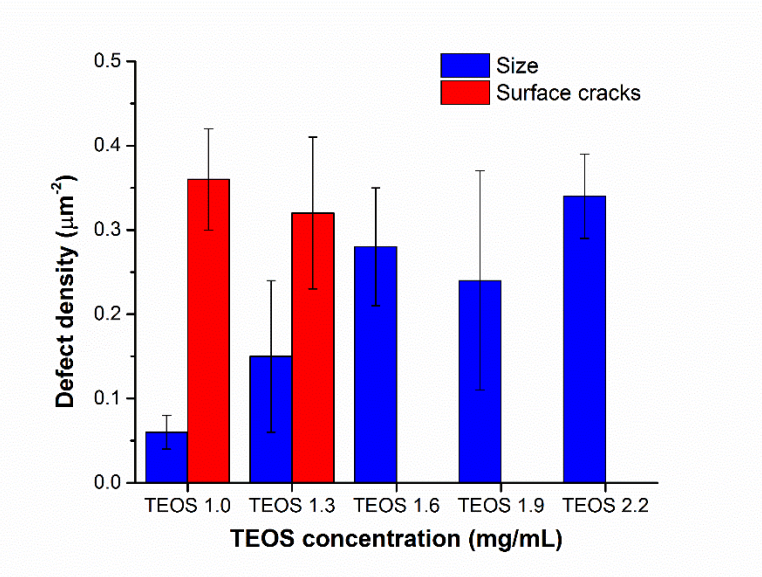

Figure 3-17: The defect density calculated for the inverse opal films made by varying the concentration of tetraethyl orthosilicate, the concentration of colloids was kept constant at 1.3 mg/mL.

The first set of samples were prepared by varying the concentration of colloids (at 1.9 mg/mL of tetraethyl orthosilicate). Unlike the vacancies, which are negligible at some colloidal concentrations, the size defects were observed at all concentrations (**Figure 3-17**). However, the size defects may appear greater than the actual amount due to the presence of overlayers (e.g. inverse opals made with changing colloidal concentration – 0.4 and 0.7 mg/mL of colloids). The silica overlayers partially covered some voids resulting a high density of size defects (S). Line defects and wall defects did not show any trend with respect to the colloidal concentration. Moreover, none of the cracks were seen in these inverse opal films.

The second set of samples were prepared by varying the concentration of tetraethyl orthosilicate (at 1.3 mg/mL of colloids). At the lowest concentration of tetraethyl orthosilicate (1.0 mg/mL or TEOS 1.0), the lowest density of size defects was reported (**Figure 3-17**). Both TEOS 1.0 and

TEOS 1.3 showed high densities of surface cracks (C), which propagated to a similar length. As described earlier, the poor infiltration of tetraethyl orthosilicate at low concentrations caused the high density of cracks. The density of surface cracks was comparatively higher than the density of deep cracks (D). The cracks significantly reduced beyond TEOS 1.6. There was no significant effect from the colloidal concentration on *microscopic defects*. Low tetraethyl orthosilicate concentrations resulted surface cracks whereas high concentrations caused size defects.

3.3.6 Inverse Opal Structures: Effect of HCl Concentration

The sol-gel process starts with the hydrolysis step, which can be catalyzed by acid or base catalytic agents. Mineral acids are commonly used as acid catalysts. According to Iler's description,[177] water facilitates the hydrolysis process, which is followed by the condensation reactions where Si-O-Si bonds form. Further condensation generates colloidal silica particles (sol), which are 1-100 nm in size. The size and the internal cross-links of the particles depend on the pH and the ratio between water and tetraethyl orthosilicate. In the co-assembly technique that we have used for fabrication of inverse opal films, the silica sol particles fill the interstitial spaces between PMMA colloids due to the capillary forces. When the silica sol particles link together with condensed silica molecules, the gelation starts and produces a solidified silica network. The drying step of the fabrication process removes the solvent from the pores of the interconnected network of silica and, if the pores are smaller than 20 nm, the capillary forces generate cracks. As the formation of cracks depends on the silica network, the cracks can be minimized by controlling the rates of hydrolysis and condensation.[178] The sol-gel process of tetraethyl orthosilicate is shown in the **Scheme 3-1**.

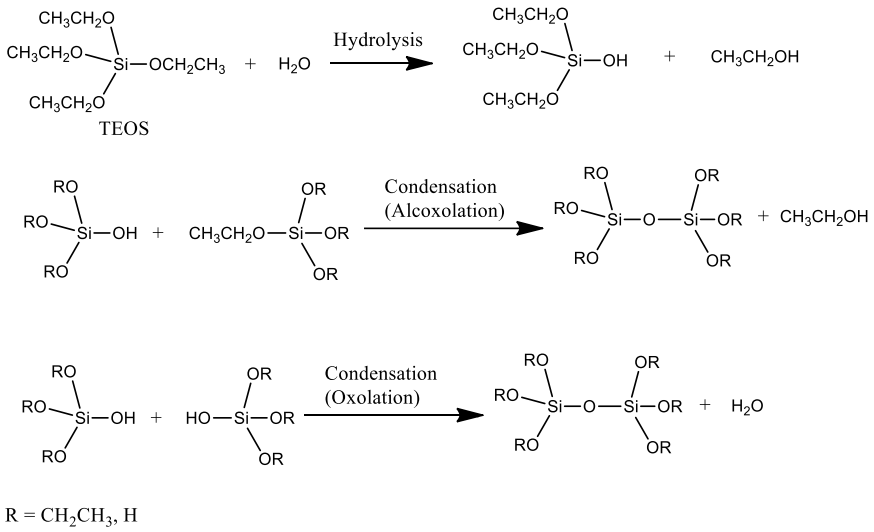

Scheme 3-1: The sol-gel process of silica in the presence of tetraethyl orthosilicate (TEOS) as the sol-gel precursor.

In this study, the hydrolysis of tetraethyl orthosilicate was acid catalyzed. Therefore, the main purpose of this experiment was to investigate the effect of concentration of acid on the quality of the inverse opal films. The tetraethyl orthosilicate stock solution was prepared, as reported elsewhere,[20] by mixing HCl (aq) [the concentrations of HCl solutions was changed as follows: 1.0 $\times 10^{-4}$ M (pH 4), 1.0 $\times 10^{-3}$ M (pH 3), 1.0 $\times 10^{-2}$ M (pH 2), 1.0 $\times 10^{-1}$ M (pH 1), and 1.0 M (pH 0)], ethanol and tetraethyl orthosilicate in the weight ratio of 1:1.5:1 followed by stirring for 1 h. Ethanol facilitates the dissolution of tetraethyl orthosilicate while water helps the hydrolysis. During the stirring period, the hydrolysis of tetraethyl orthosilicate is started.

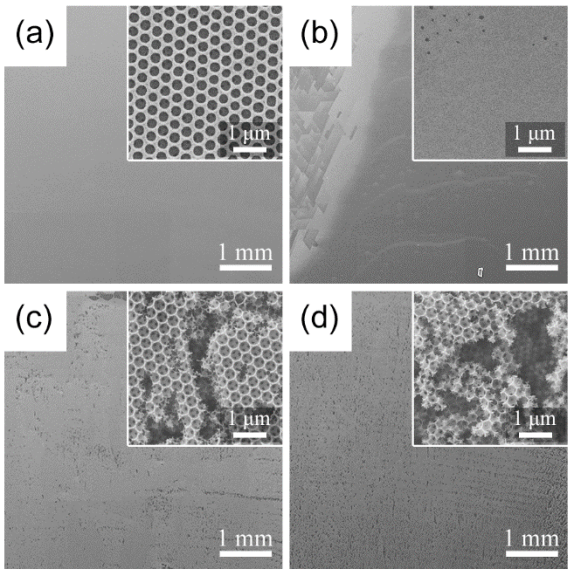

Figure 3-18: Stitched SEM images of Inverse opal films made at 1.3 mg/mL of colloids and 1.9 mg/mL of tetraethyl orthosilicate, where the tetraethyl orthosilicate stock solution was made by using HCl solutions a different pH values: (a) pH 0.0 (1.0 M), (b) pH 2.0 (1.0×10^{-2} M), (c) pH 3.0 (1.0×10^{-3} M), and (d) pH 4.0 (1.0×10^{-4} M), the concentrations of HCl solutions are mentioned in the parentheses and the insets show the magnified SEM images of the respective inverse opal film; (f) the percentage of defects as a function of pH of the HCl solution.

In the fabrication process, the catalytic activity of the acid plays an important role as the gelation time increases at elevated pH values.[179] It was observed that the tetraethyl orthosilicate stock solutions prepared by adding HCl solutions at pH 4 and pH 3 solidified completely within seven days whereas the solutions made with HCl solutions at pH 2, pH 1, and pH 0 did not solidify even after 14 days. As shown in **Figure 3-18**, the acid solutions at pH 0 and 1 resulted in very few defects in the inverse opal films, while the pH 2 acid solution caused a large number of defects, especially a large overlayer (inset of **Figure 3-18b**). Our results show that low acid concentrations used in the tetraethyl orthosilicate stock solution caused more cracks as a consequence of fast gelation, which applied an additional stress on the film. On the contrary, slow gelation supported by high acid

concentrations improved the quality of inverse opal films by producing fewer cracks. The cracks seen in the samples made using acid solutions of both pH 3 and 4 (insets of **Figure 3-18c** and **d)**, cannot be quantified by thresholding (for more details see **Section 3.3.4.1**). Since 0.1 M solution of HCl was used in the fabrication of inverse opals with changing both colloidal and tetraethyl orthosilicate concentrations (**Section 3.3.3** and **3.3.4**), the effect due to the HCl concentration for the formation of defects was minimized.

3.3.7 Synthesis of PMMA Colloids with Different Sizes (Analysis of Dry and Wet Particle Sizes)

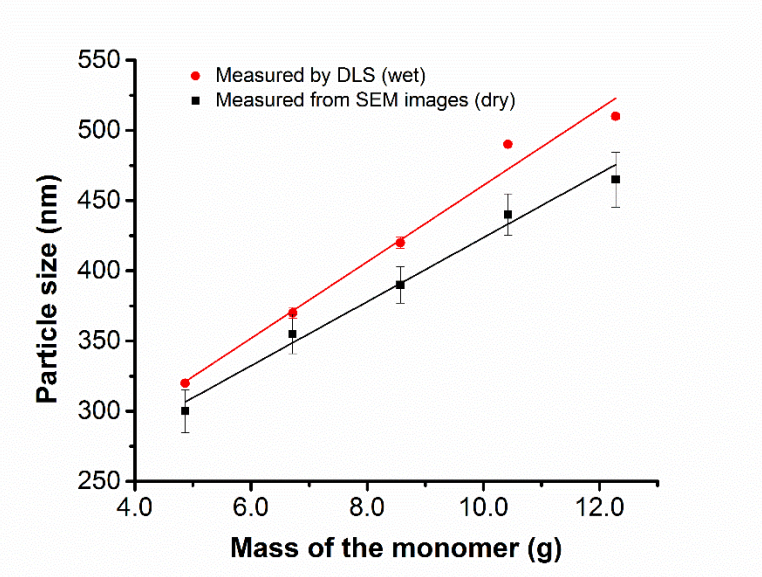

Figure 3-19: The sizes of PMMA colloids synthesized by using different monomer masses of 4.9 g (5.25 mL), 6.7 g (7.25 mL), 8.6 g (9.25 mL), 10.4 g (11.25 mL), and 12.3 g (13.25 mL).

Here, an investigation was conducted on the fabrication of inverse opal films with PMMA colloids of different particle sizes in order to tune the stopband.[180] The parameters such as concentrations of the initiator, monomer, surfactant etc., influence the particle size of the PMMA colloids. It was found that the concentration of monomer can be successfully used to significantly change the size of the particles in a linear fashion (**Figure 3-19**). According to **Figure 3-19**, the monomer volume showed linear relationship with the particle size, both dry and wet, and had good R^2 values (0.98) in both cases. Colloids with particle sizes ranging from 300 to 465 nm (dry) were synthesized from the procedure that we used.

3.3.7.1 Inverse Opal Films Fabricated using Colloids of Different Sizes

The opal and inverse opal films were fabricated by using the PMMA colloids of different particle sizes in order to study the effect of the size of colloids on the quality of the thin films. Here, the quality was evaluated by SEM images and optical spectroscopy.

3.3.7.2 Analysis of SEM Images

SEM images of the opal and inverse opal films showed close-packed arrangements of colloids and voids, respectively. The hexagonal arrays of particles and voids are clearly visible in these SEM images (**Figure 3-20**). The two-dimensional fast Fourier transform (2D-FFT) images also confirmed the long-range periodicity of the opal and inverse opal samples. The PMMA colloids were less stable under the electron beam of SEM and the movement of colloids in the opal films was observed. Furthermore, expansion of the cracks was also observed under the long exposure of the opal films to the electron beam. The deterioration of the colloidal film can be minimized by applying conditions such as low vacuum and low voltage; but, the images were not as sharp as the images taken under high vacuum and voltage. However, the SEM images provide a clear view of morphology and assembly of the colloids. Unlike the opal films, the inverse opal films were stable

under the harsh conditions (high vacuum and electron beam) used in the SEM imaging (**Figure 3-20b**).

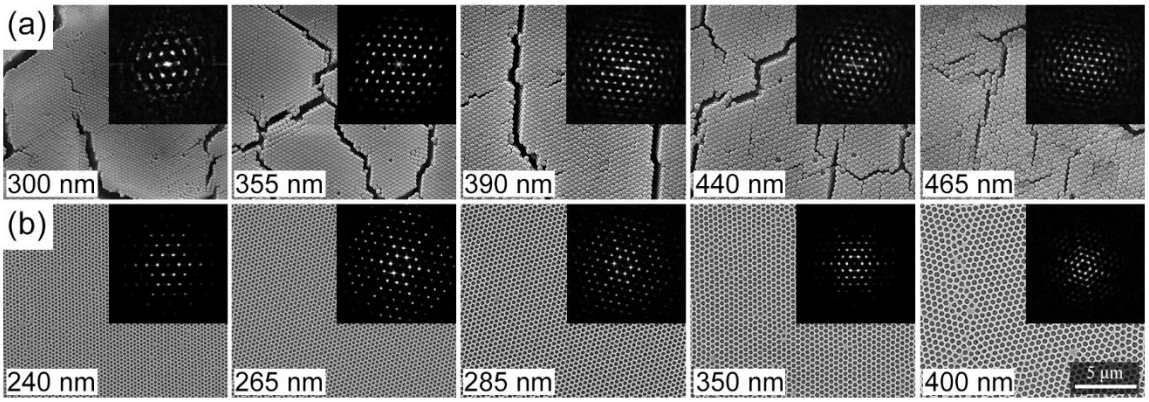

Figure 3-20: (a)The SEM images of opal films made with varying particle sizes (300-465 nm) (b) Inverse opal films made with colloids having same size as (a). The average size of colloids (opals) and voids (inverse opals) are mentioned in each image. The insets show 2D-FFT images of each SEM image.

3.3.7.3 Optical spectroscopy analysis of the opal and inverse opals made with different sizes of colloids

Since the wavelength of the stopband is directly proportional to the void size, the color of the films can be tuned to higher wavelengths by increasing the size of the colloids in the sacrificial template. The optical spectra obtained for the opal films fabricated from the colloids with dry particle sizes of 300 nm, 355 nm, 390 nm, 440 nm, and 465 nm, showed strong stopbands at 640 nm, 730 nm, 835 nm, 905 nm, and 960 nm, respectively (**Figure 3-21a**). Transmittance spectra of the opal films show clear stopbands that gradually shift towards the near-infrared (NIR) region as the particle size increases (**Figure 3-21a**). Stopbands at 490 nm, 560 nm, 620 nm, and 740 nm were obtained for inverse opal films made with PMMA colloids having dry particle sizes of 355 nm, 390 nm, 440 nm, and 465 nm respectively. No stopband was observed for the films made by using colloids of 300 nm because it might have shifted to the UV region. Theoretically, the corresponding stopband

should appear at 390 nm if the volume fraction of the voids is assumed to be 0.74 and the shape of the voids is spherical. The stopbands obtained for the inverse opal films were blue shifted from the stopbands of opal films when both films were fabricated by using the colloids of the same size. Furthermore, the dependency of the stopband on the angle of incident light was also studied and found out that the stopband was blue shifted with the increments of the angle indicating good periodicity.

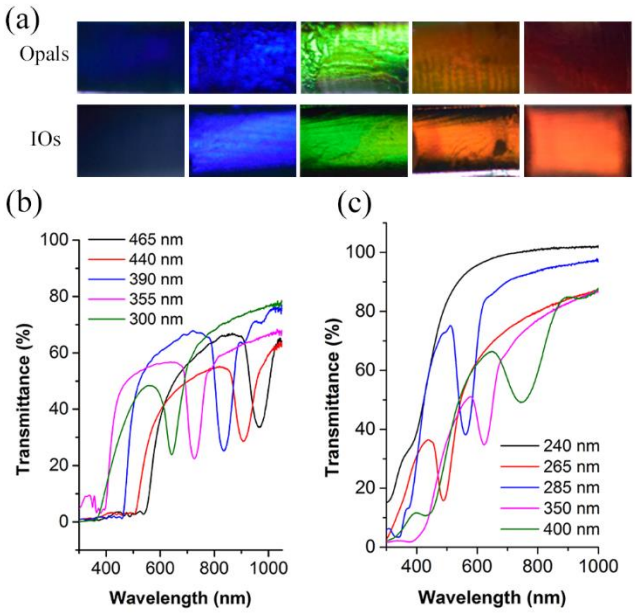

Figure 3-21: (a) Digital photographs of opal films and inverse opal films (IOs) were taken at an angle to the light source which was kept parallel to the surface; (b) transmittance spectra of opal films fabricated with varying particle sizes (300 nm, 355 nm, 390nm, 440 nm, and 465 nm); (c) transmittance spectra of inverse opal films made with particle sizes mentioned in (b); the sizes of the voids were mentioned in the legend (240 nm, 265 nm, 285 nm, 350 nm, and 400 nm).

3.4 Conclusion

In this study, we have optimized the conditions to produce defect-free inverse opal films using the co-assembly technique. Parameters such as colloidal concentration, tetraethyl orthosilicate concentration, and pH of the acid solution used to prepare the tetraethyl orthosilicate stock solution affect the quality of the inverse opal films significantly. Even though there are several other factors that control the quality of the inverse opal films, the optimum concentrations of colloids and tetraethyl orthosilicate are crucial for the fabrication process. Defects such as stick-slip bands form due to low concentrations of colloids and overlayers result from the high concentration of tetraethyl orthosilicate. The ratio of colloids to tetraethyl orthosilicate is critical to minimizing the presence of cracks. Slow hydrolysis of tetraethyl orthosilicate improves the quality of the inverse opal films. As well, we have synthesized PMMA colloids with different sizes. Since there is a good linear relationship between the particle size and the stopband wavelength, by changing the size of the colloids, it is possible to fabricate the inverse opal films that can reflect light in the full range of the visible light; hence leading to potential applications, such as displays and sensors.

CHAPTER IV

DETERMINATION OF THE STRUCTURE OF SILICA INVERSE OPALS USING SEM IMAGES

4.1 Introduction

An inverse opal is a crystalline material that consists of submicron size voids arranged in a long-range order. The periodic arrays of voids interfere with the light passing through them and prevent the propagation of certain wavelengths (band gap). Therefore inverse opals are extensively studied as a potential material for photonic crystals.[181-183] Other than photonics, [2, 184] these materials have potential applications in data storage,[185] sensors,[135] scaffolding,[186] and in optoelectronics.[187] The inverse opal crystals are generally fabricated *via* infiltration of a sol-gel precursor into the interstitial sites of self-assembled colloids followed by removal of the colloidal template.[27, 96, 157, 181, 188] Since the conventional fabrication technique that is based on infiltration generates several defects in the inverse opal structure, co-assembly was developed to reduce the number of defects in the produced inverse opal films.[20] In this method, the inverse opals are fabricated using a solution containing both colloids and sol-gel precursor and then the colloidal template is removed.

The structure of the inverse opals determines the photonic properties; thus, it is important to analyze the structure of the fabricated inverse opals. The periodic arrangement of voids in an inverse opal can be analyzed using small-angle x-ray diffraction (SAXS),[25, 26] Transmission Electron Microscope (TEM),[27-29, 189] Scanning Electron Microscope (SEM),[30, 31] and diffraction of light.[32] Image analysis techniques of SEM or TEM images can provide more information. A digital image represents a real object as a combination of pixels with different intensities of colors. For example, an 8-bit grayscale image has 256 shades of possible gray values for a pixel.[190] The position of these gray values in the 2-dimensional grid is seen as the image. The distance between two discrete objects can be calculated using the scaling factor of the image. Hence, small objects can be analyzed using images taken with digital cameras. Not only can one define the positions of objects in the real space, but also information such as periodicity, crystallinity, etc., can be obtained by analyzing images. Fourier transformation is a useful tool that is used for the analysis of the periodicity of an object and also can be combined with other image analysis techniques. The Fourier transformation breaks the space domain signal of an image to a frequency domain signal which is composed of series of sinusoidal signals. Any periodicities in the original image appear as a spot pattern in the resulting image of a periodic/crystalline material.[191] Since inverse opal photonic crystals have periodicities in their microstructures, Fast Fourier transform (FFT) can be used to determine the structure.[111, 180, 192, 193]

The structure of the inverse opal films such as the assembly of voids, domains, lattice orientation, and cracks fabricated *via* co-assembly was analyzed in more detail. In **chapter 3,** we have reported that the quality of the inverse opal films depends on the concentration of the colloids and the tetraethyl orthosilicate. There, we have used both image thresholding, and ultraviolet-visible spectroscopy to analyze defects of inverse opal films. In this chapter, we focus mainly on the structure of the inverse opals. Also, we have investigated the use of 2-D fast Fourier transform

(2D-FFT) to analyze the crystalline domains in inverse opals. Here, the SEM images were analyzed to quantify the surface filling fraction of silica and fraction of surface defects. Furthermore, we have introduced methodologies to determine the optimum ratio of colloids to tetraethyl orthosilicate and to analyze the uniform periodicity of fabricated thin films.

4.2 Materials and Methods

4.2.1 Materials

All the chemicals were used as received unless otherwise it is mentioned. Ethylene glycol dimethacrylate (98%), methyl methacrylate (99%), 1-dodecanethiol ($C_{12}H_{26}S$, 98%), ammonium persulfate ($(NH_4)_2S_2O_8$, 98%) and tetraethylorthosilicate (TEOS, 98%) were purchased from Sigma-Aldrich Chemicals (St. Louis, MO). Absolute ethyl alcohol and ACS reagent grade hydrochloric acid (HCl, 36.5-38.0%) were purchased from Pharmco-AAPER (Brookfield, CT). ACS reagent grade hydrogen peroxide (H_2O_2, 30% (w/w)) was purchased from Ricca chemical company (Arlington, TX). Silicon wafers (p-type Si:B[100], R_o = (1-100) Ω cm) were purchased from El-Cat Inc. (Ridgefield Park, NJ). The surface of the silicon substrates was treated using a corona treater (Electro-Technic Products, BD-20). A water purification system (Barnstead Nanopure^{TM}), at a resistance of 18.1 Ω/cm, was used to obtain deionized water.

4.2.2 Methods

4.2.2.1 Synthesis of Colloidal Particles

Poly(methyl methacrylate) (PMMA) colloids with particle size of 345(±20) nm were synthesized by emulsion polymerization, and characterized as described in **chapter 3**. Briefly, ammonium persulfate (0.1 g) was added to a three-neck round bottom flask containing deionized (DI) water (45.0 mL) at 80 °C. Then the solution was stirred at 400 RPM for 1 h. Meanwhile, methyl methacrylate (9.25 mL), ethylene glycol dimethacrylate (47.4 μL) and 1-dodecanethiol (23.7 μL)

were mixed in a glass vial and sonicated for 5 min. Afterward, the sonicated mixture was injected into the three-neck round bottom flask and stirred for 3 h. Resultant colloids were purified by centrifugation (45 min. at 4,500 RPM) and washed three times with DI water. The resulting pellet was re-dispersed in DI water to prepare a colloidal PMMA working solution. The size of the resulting particles was measured using scanning electron microscope (SEM) (FEI Quanta 600 FE).

4.2.2.2 Fabrication of Inverse Opal Films

Inverse opal films were fabricated using the co-assembly process as previously reported,[20] where Si substrates, cleaned in piranha solution and treated with a BD-20 handheld corona treater (Electro-technique products Inc.), were vertically suspended in a vial containing a solution of colloids and tetraethyl orthosilicate in the desired ratio (the tetraethyl orthosilicate stock solution was prepared by mixing 0.1 M HCl, 200 proof ethanol, and tetraethyl orthosilicate in a 1:1.5:1 mass ratio). The ratio between the concentrations of colloids to tetraethyl orthosilicate (Col/TEOS) in the mixture was varied as follows: 0.21, 0.37, 0.53, 0.68, 0.84, 1.00, and 1.30. The solvent was evaporated slowly over a 24 h period at 65°C in a Binder™ oven and allowed to deposit onto the substrate. The films were then calcined in air using a Thermolyne 2110 tube furnace at 500 °C for 2 h with a 5 h ramp time to remove the polymer template and partially sinter the SiO_2 structure.

4.2.2.3 Image Analysis

Determination of size of voids

The top surface of the inverse opal films was imaged using SEM at a magnification of 16000× and the images were analyzed using ImageJ 1.48v software (Wayne Rasband, National Institutes of Health, USA). The size of the voids (300 voids from each Col/TEOS ratio) was measured using the "analyze particles" function of ImageJ. The 2D-FFT algorithm was used to analyze the interplanar distance of voids and the lattice orientations of the inverse opals.

Determination of area of surface defects

The percentage area of surface defects analyzed using the following method: three random SEM images were analyzed for each inverse opal film made with different ratios of Col/TEOS. The SEM images were converted to 8-bit grayscale binary images using the Otsu thresholding method in ImageJ. To determine the area corresponding to defects ($A_{defects}$), the areas of voids (A_{voids}) and silica (A_{silica}) have to be deduced from the total (A_{total}) and the percentage of defects (%$A_{defects}$) can be determined by,

$$\%A_{defects} = \frac{[A_{total} - (A_{voids} + A_{silica})]}{A_{total}} \times 100 \qquad \textbf{(4-1)}$$

The area of voids (A_{voids}) was calculated using the analyze particle option in the ImageJ software and converted to percentage. The following parameters were set for the analyze particle option to minimize the errors by eliminating defective areas: size-0.05 to 0.10 μm^2, circularity-0.75 to1.00, and edges were excluded. Since the percentage area of silica (A_{silica}) was unable to be calculated directly, a different method was used. A region with a good periodicity was selected in each SEM image and the area of voids (a_{voids}) was determined as mentioned earlier. The area of silica in that region was found out by subtracting the area of voids (a_{voids}) from the total (a_{total}) and the percentage of silica is given by,

$$\%A_{silica} = \frac{(a_{total} - a_{voids})}{a_{total}} \times 100 \qquad \textbf{(4-2)}$$

Then, percentage area of defects (% $A_{defects}$) was determined by substituting A_{voids} and A_{silica} into the previous equation (**Equation(4-1)**).

4.3 Results and discussion

4.3.1 Analysis of the close-packed arrangement of voids

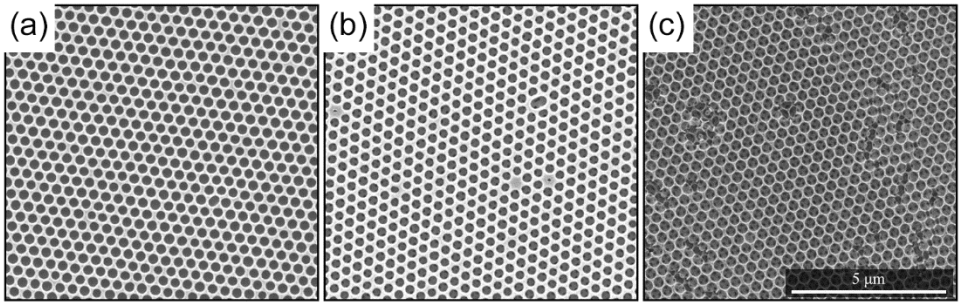

Figure 4-1: SEM images of inverse opal films made with different ratios of colloids and tetraethyl orthosilicate: (a) 0.21, (b) 0.53, and (c) 1.3.

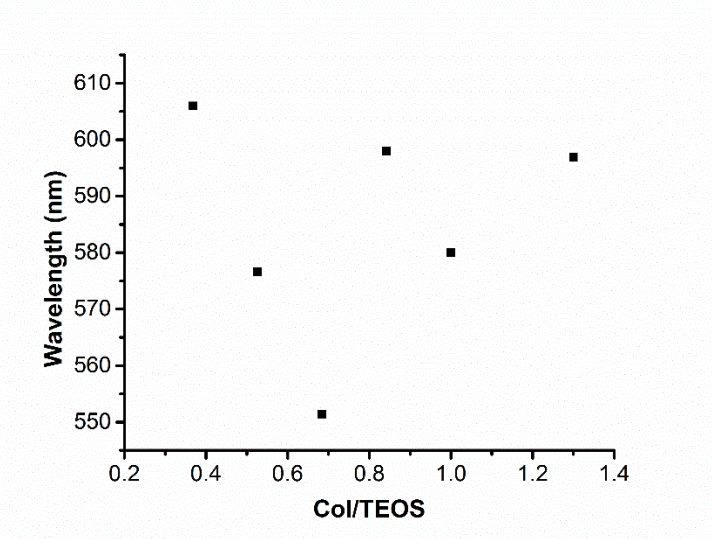

Figure 4-2: The graph of position of the stopband with varying ratios of Col/TEOS.

The inverse opal films were fabricated by changing the ratio of concentration of PMMA colloids (size = 345 nm) to tetraethyl orthosilicate (Col/TEOS) in working solutions (Col/TEOS - 0.21, 0.37, 0.53, 0.68, 0.84, 1.00, and 1.30). After removing the template (colloids), the resulting thin films were imaged under SEM. **Figure 4-1** shows SEM images of inverse opal films made with three different ratios of Col/TEOS. The images are arranged in the order of increasing ratio of Col/TEOS

(left to right: 0.21, 0.53, and 1.3). The quality of the inverse opal films varied depending on the ratio of Col/TEOS where the higher Col/TEOS ratios resulted in highly defective films. As well, the shape and the position of a stopband is an indication of the quality of an inverse opal film. In **Chapter 3,** the variation of the shape of stopbands with respect to the varying concentrations of colloids and tetraethyl orthosilicate was discussed in detail. **Figure 4-2** shows the variation of the position of the stopband with the ratio of Col/TEOS. Even though the stopband varies with Col/TEOS, a proper trend was not observed. As the structure determines the optical properties of these inverse opals; it is worthwhile to study the influence of Col/TEOS to the structure of the fabricated inverse opals.

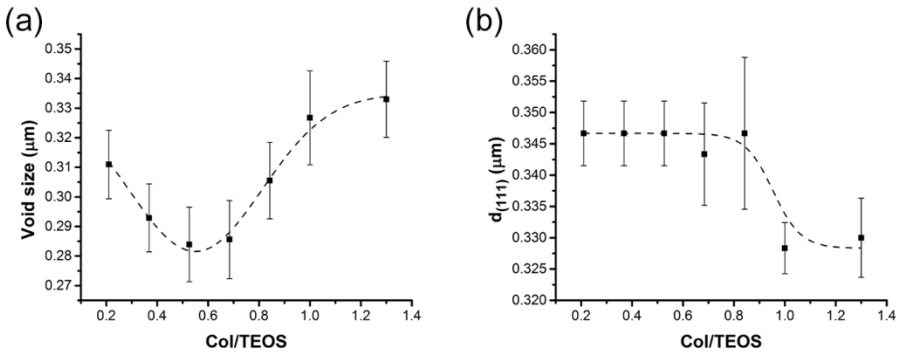

Figure 4-3: Variation of the (a) void size and (b) interplanar distance as a function of Col/TEOS ratio.

The size of the voids of the inverse opals varies with the ratio of Col/TEOS. The size of voids was analyzed from the SEM images of top view of the fabricated inverse opals. According to the graph in **Figure 4-3a**, the ratios above 1.0 yielded the highest void size while the lowest size of the voids corresponded to the ratio of ~0.6. The size variation may result either from (1) the expansion of silica during calcination or (2) the filling of an additional amount of silica on the top surface of inverse opal films. Since both colloids and tetraethyl orthosilicate simultaneously assemble during the co-assembly, both components collectively determine the structure of the colloidal film. All

samples were calcined under the same temperature program; hence the same rate can be assumed for the shrinkage of colloids in each case. Under these conditions, it is difficult to determine the reason for variation of void size depending on the ratio of Col/TEOS; therefore, a 2D-FFT was conducted for the SEM images.

Two dimensional fast Fourier transform (2D-FFT) is a useful analysis technique to study the structure of a crystalline material. It was adopted to study materials with large periodic structures, such as opals and inverse opals.[32, 180, 194, 195] The Fourier transformation of an image consisting of *m* rows and *n* columns and can be represented as[191]

$$F(h,k) = \sum_{n=0}^{N-1}\sum_{m=0}^{N-1} I(n,m)\exp\left[\left({}^{2\pi i}/_{N}\right)(hn+km)\right] \qquad \textbf{(4-3)}$$

where h and k are spatial frequencies. The spot pattern resulting from the analysis can be used to calculate the interplanar distance and center-to-center distance of voids in an inverse opal film. Since the angle between center-to-center distance and the interplanar distance is 30°, the relationship between the interplanar distance (d) and the center-to-center distance (a) is given by

$$d = a\cos(30) \qquad \textbf{(4-4)}$$

According to **Figure 4-3b**, the variation of the interplanar distances with the Col/TEOS ratio follows a trend different from the trend seen for the variation of void sizes. At low ratios of Col/TEOS the interplanar distance was at ~345 nm and does not vary significantly. When the Col/TEOS ratio reached 1.0, the interplanar distance decreased to ~330 nm. Even though the size of voids varies when the Col/TEOS ratio is below 1.0, the interplanar distance stays constant. This means that the size variation of the voids (Col/TEOS ratio below 1.0) is not due to the shrinkage of the lattice. For further evaluation of the variation of size of voids, an SEM image of a cross-section of an inverse opal film was taken.

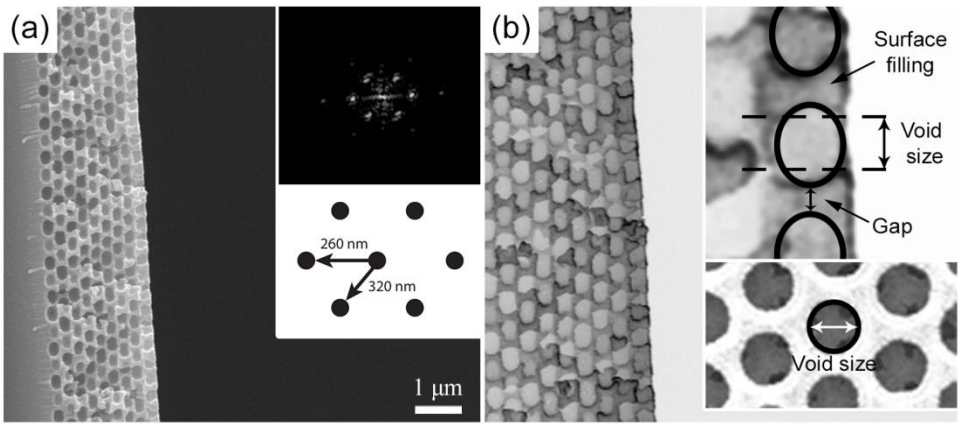

Figure 4-4: (a) SEM images of a cross-section of an inverse opal film made at the Col/TEOS ratio of 0.68, the top inset shows the 2D-FFT image and the bottom shows the schematic representation of the FFT pattern with two different interplanar distances and (b) the same SEM image converted with lookup tables (invert LUT) of ImageJ for better visualization of the structure; the top inset is an enlarged image of (b) showing *surface filling* of silica, real and measured sizes of a void, and the gap between two voids and the bottom inset shows the size of a void as seen from the top view.

As seen in **Figure 4-4**, the inverse opal films made using co-assembly showed spheroidal voids. As well, additional amounts of silica were seen on the surface (labelled as *surface filling* in **Figure 4-4b**-inset). The silica matrix of the inverse opal is resulted from the sol-gel chemistry of silica. According to the sol-gel process tetraethyl orthosilicate hydrolyzed and condensed to form sol particles which are later interconnected with each other to from a network (gel). This network further condensed during calcination which results in shrinkage in the matrix.[178, 196] According to the previous study published by Phillips et al., spheroid shaped voids were produced when the inverse opal films were fabricated on rigid substrates.[159] Since colloids are attached to the substrate, during calcination, shrinkage of the silica matrix occurs along one direction. We have calcined our samples at 500 °C and our results were comparable with the data published by Phillips et al. Since the voids are spheroidal in shape, there are two different interplanar distances for the inverse opal crystal (inset of **Figure 4-4a)**. From the top surface view, voids have a circular shape and the size

of the voids for the inverse opal film (Col/TEOS ratio of 0.68) shown in **Figure 4-4** is 286(±13) nm. However, the actual void size (measured from the cross section) is 223(±13) nm and 336(±20) nm along the minor and major axes respectively. As the background is darker in the original image, an inverse lookup table (inverse LUT) was used to clearly visualize the geometry of the void (**Figure 4-4b**). The inset (top) of **Figure 4-4b** shows an enlarged part of the cross-section close to the surface of the thin film. It is evident that a gap is present between two adjacent voids and that there is an additional amount of silica on the top surface layer of the voids, which is referred here as *surface filling*.

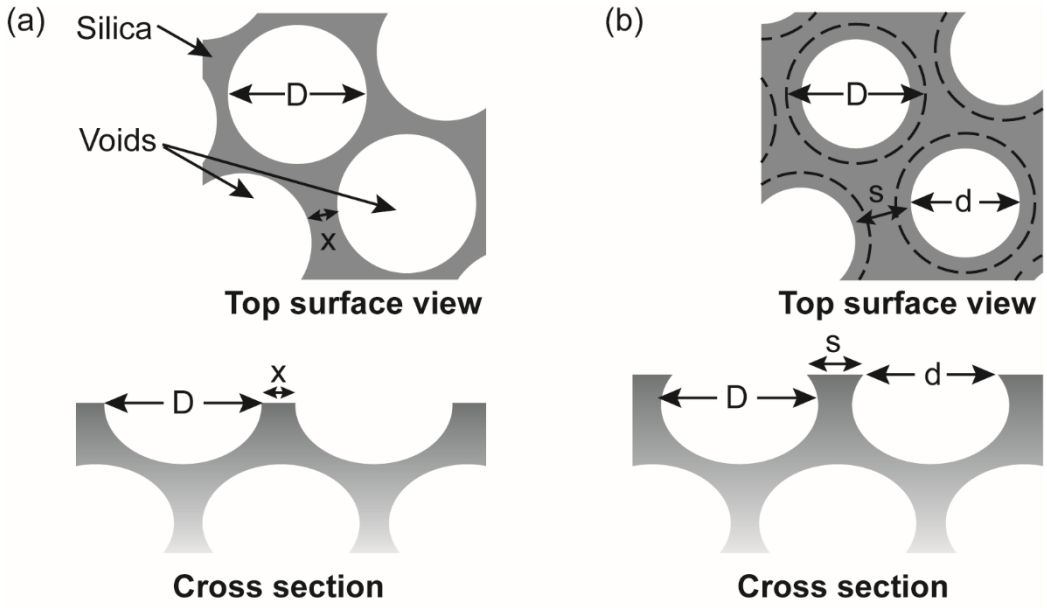

Figure 4-5: (a) A cross section and a top view of inverse opals where **D** is the diameter of a void and **x** is the gap between two voids when half of the space is filled with silica (along the minor axis of a void). (b) A cross section and a top view of an inverse opal with additional amounts of silica (*surface filling*) filled onto the surface layer of voids where **d** is the diameter of a void and **s** is the gap between two voids when more than half of the space is filled with silica. The dashed line represents the true diameter of a void. The x and s are measured along the line that connects centers of two adjacent voids.

As seen in **Figure 4-5**, the *surface filling* reduces the size of the voids measured from the top surface of an inverse opal. Here, we have set the gap between two voids (x) when the space in between is halfway filled with silica (along the minor axis of a void) as the ideal condition. In the presence of a *surface filling*, the gap between two voids (s) is larger than the ideal (s > x).

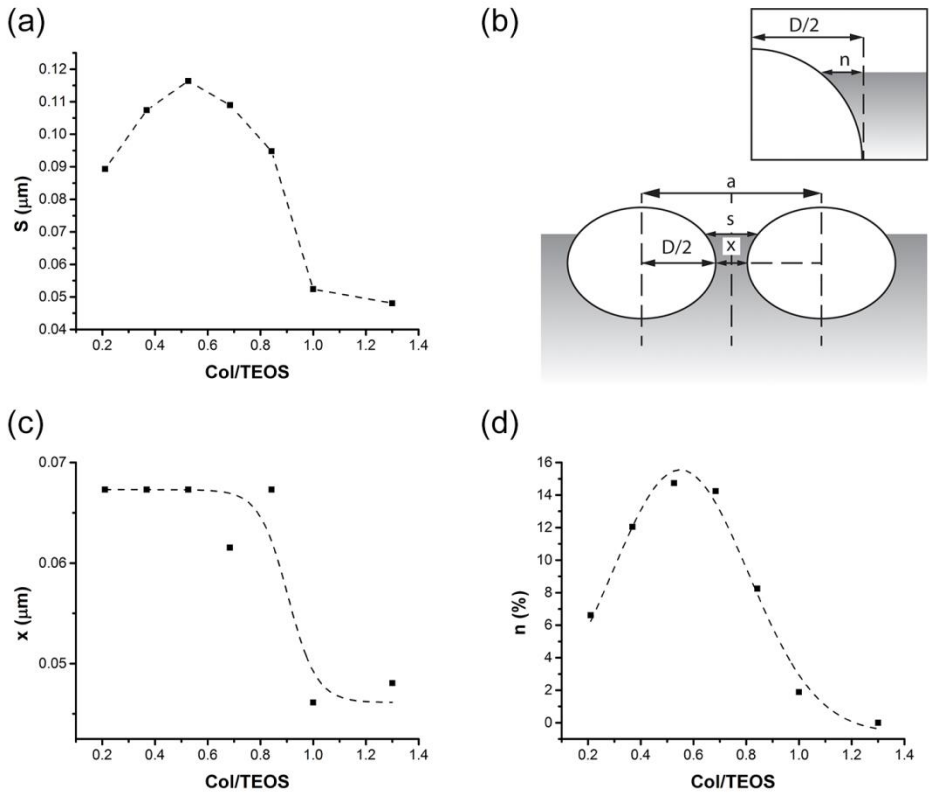

Figure 4-6: (a) The variation of the gap (**s**) between two voids observed from the top surface view. The **s** is the difference between the center-to-center distance (**a**) and the size of voids (**D**)) (b) A schematic representation of the arrangement of voids on silica matrix where x is the ideal gap between voids and **n** is the half of the difference between **s** and **x**. (c) The gap between two voids (**x**), and (d) the surface filling fraction (**n%**) of silica as functions of the Col/TEOS ratio.

The *surface filling* was determined as a percentage (n%) where the complete coverage of a void by silica was set as 100%. In **Figure 4-6a**, the difference between the center-to-center distance (**a**) and the size of voids (**D**) was measured as the gap between two voids (**s**). The difference, **s,**

increases up to 115 nm (at 0.53 ratio of Col/TEOS) and then decreases. The lowest **s** value (50 nm) is obtained when the ratio of Col/TEOS is 1.3. At this level, the void size is 333(±12) nm, which is closer to the void size (336 nm) measured from the cross-section of the inverse opal film made at the Col/TEOS ratio of 0.68 (**Figure 4-4**); hence, we can assume that at this ratio (1.3) there is no *surface filling* (n% = 0). The value of **s** at this stage must be equal to **x**. Considering above factors and assuming the size of the voids is equal to 333 nm, a relationship between the **x** and **a** can be derived:

$$x = a - 333 \qquad \textbf{(4-5)}$$

Furthermore, a relationship between **x** and the additional amount of silica between voids on the surface (**n**) can be derived:

$$n = {}^{s}/_{2} - {}^{x}/_{2} \qquad \textbf{(4-6)}$$

The fraction of the excess amount of silica on the surface (**n%**) can be obtained with the following assumption; when the surface filling is 100% then,

$$n = {}^{D}/_{2} \qquad \textbf{(4-7)}$$

So the fraction of surface filling is

$$n(\%) = \frac{n}{{}^{D}/_{2}} \times 100 \qquad \textbf{(4-8)}$$

The variation of x with respect to the ratio of Col/TEOS shows a similar trend as the variation of interplanar distance (**Figure 4-6c**). When the Col/TEOS ratio is below 1.0, the gap between the voids is 70 nm and above 1.0 is 50 nm. The small gap observed above the ratio of 1.0 must be due to the lesser amount of tetraethyl orthosilicate. Since tetraethyl orthosilicate is insufficient above the Col/TEOS ratio of 1.0, condensation of silanol groups during the calcination leads to shrinkage of the lattice which ultimately leads to cracks.

The surface filling fraction with respect to the ratio of colloids and tetraethyl orthosilicate is shown in **Figure 4-6d**. According to **Figure 4-6d**, the *surface filling* approaches zero when the ratio reaches 1.0. The highest fraction is obtained when the ratio is ~0.6. The quality of the film at this ratio is good compared to the others (refer **Chapter 3** for more details). This means tetraethyl orthosilicate plays a vital role in the co-assembly process to improve the quality of the resulting thin films. This was further confirmed by correlating this finding with the corresponding stopbands.

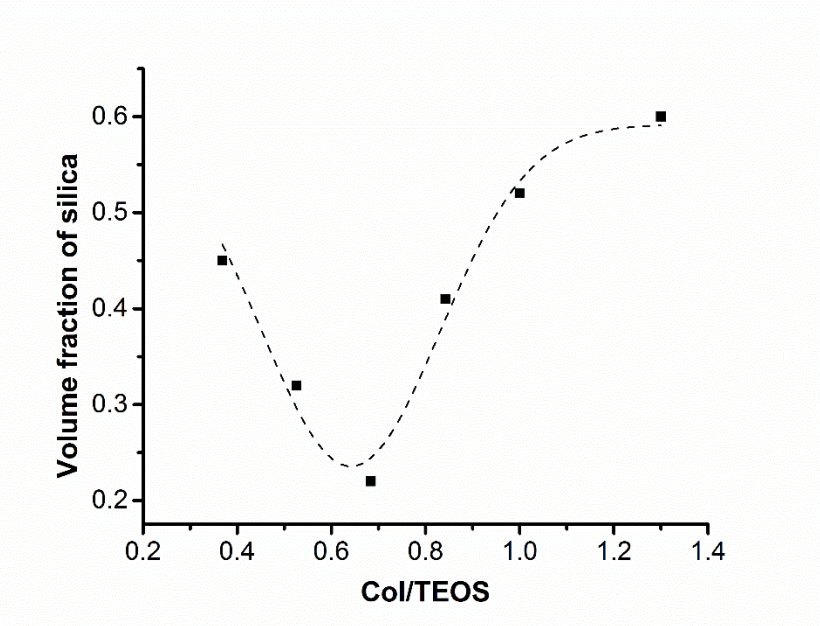

Figure 4-7: The variation of the volume fraction of silica with respect to the Col/TEOS ratio.

According to **Figure 4-7**, both the volume fraction of the silica and the void size (**Figure 4-3a**) of inverse opals made with varying ratios of Col/TEOS showed a similar trend. Moreover, both volume fraction of silica and the void size showed an inverse behavior with the *surface filling* fraction of silica. Therefore, the lowest volume fraction of silica is obtained at the maximum *surface filling* fraction of silica. The volume fraction of silica was obtained using the following equation:

$$\lambda = \frac{2d_{hkl}}{m}[\phi n_a + (1-\phi)n_s] \qquad \textbf{(4-9)}$$

Here, λ is the wavelength of the stopband, d_{hkl} is the interplanar distance between two crystal planes, m is the order of the incident light, ϕ is the volume fraction of silica, n_s is the refractive index of silica (1.459), and n_a is the refractive index of air (1.000). Considering first order reflection (m=1), the volume fraction of the inverse opals made with varying Col/TEOS ratios was calculated. Since the size of actual void does not change significantly with Col/TEOS ratio, the void size along the minor axis (from the cross section of an inverse opal film) was taken as 220 nm. As there are two different gaps between voids, 50 nm was considered as the gap for Col/TEOS ratios of 1.0 and 1.3, and 70 nm was used for the rest of the ratios. The center-to-center distance (a) was calculated for each sample by adding both 70 nm and 50 nm to 220 nm for the corresponding samples. Then d_{hkl} was calculated by using **Equation (4-4)**. The variation of the stopband with Col/TEOS ratio was similar to the variation of the volume fraction with Col/TEOS except for the ratios of 1.0 and 1.3; this is due to the shift in d_{hkl} (**Figure 4-2**).

4.3.2 Analysis of the percentage of surface defects

The surface defects present in the inverse opal films made by the co-assembly technique were quantified from the SEM images. The analysis was conducted for random images that were taken from the samples and the defects were quantified as a percentage with respect to the unit area of the analysis (300 nm). When the amount of tetraethyl orthosilicate is reduced, more cracks were seen; hence, it is worthwhile to study the effect of the tetraethyl orthosilicate toward the quality of the inverse opal films. Here, the analysis was conducted using the films made at the ratios of colloids to tetraethyl orthosilicate that is higher than 0.6. because cracks were observed at higher ratios of Col/TEOS.

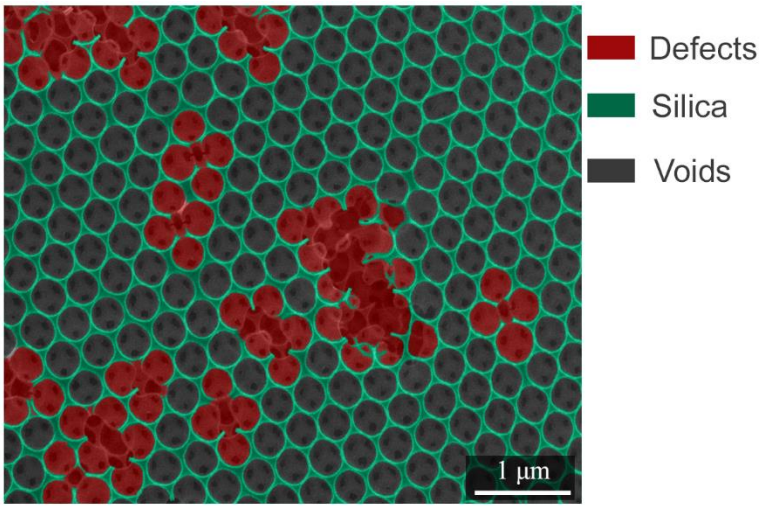

Figure 4-8: A representation of different types of areas present in a top view of an inverse opal; the areas occupied by voids (gray), silica (green) and defects (red). The image shown here was taken at a magnification of 50,000× for clear identification of different type of areas. (Images with 16,000× magnification was used for the actual analysis).

A perfect crystal should have a surface with a uniform close-packed void arrangement. For a given area, there should be a maximum number of voids that can fill the space. The area of defects can be calculated by subtracting the area of voids (A_{voids}) from thetotal (A_{total}). Since these inverse opals have significant amount of silica in the space between voids, a correction for the area covered by silica (A_{silica}) has to be conducted. The A_{silica} can be determined by analyzing a small area without defects, where the area covered with voids (a_{voids}) is subtracted from total (a_{total}) (**Equation (4-2)**). The corrected area percentage of defects was calculated using **Equation (4-1)**. The results were plotted against the ratio of colloids to tetraethyl orthosilicate (**Figure 4-9**).

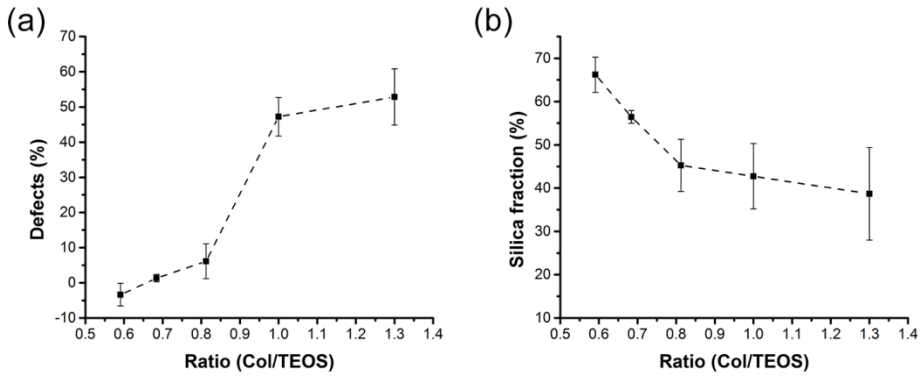

Figure 4-9: (a) The corrected area percentage of surface defects and (b) the fraction of silica with respect to the ratio of colloids to tetraethyl orthosilicate (Col/TEOS).

According to **Figure 4-9a**, the percentage of defects reduces significantly when the ratio of Col/TEOS reaches to 0.6. The highest amounts of defects were seen in the samples made with the ratios of 1.0 and 1.3. There is a notable difference in defects between ratios of 1.0 and 0.8. However, as seen in **Figure 4-9b,** the $\%A_{silica}$ is reduced when the amount of tetraethyl orthosilicate is low. The results suggest that the optimum ratio of Col/TEOS, that is needed to form inverse opal films without surface defects, is 0.8. Below 0.8, the additional amount of tetraethyl orthosilicate is condensed and deposited on the top surface.

4.3.3 Analysis of the structural arrangement of voids in inverse opal films

The 2D-FFT algorithm generates a spot pattern, resembling the long-range order of voids. **Figure 4-10a** shows an SEM image of an inverse opal film along a (111) plane of the fcc crystal. Moreover, the angle between two adjacent rows of voids is 60° and this is clearly visible in the reciprocal lattice (**Figure 4-10b**). As shown in **Figure 4-10b**, the 2D-FFT image with spots is arranged into a hexagonal pattern, which is generally observed for fcc crystals. [189] The hexagonal pattern appeared on the FFT image is a 30^{o} rotation of the hexagonal pattern of voids in the SEM image, as the 2D-FFT image represents the reciprocal space.

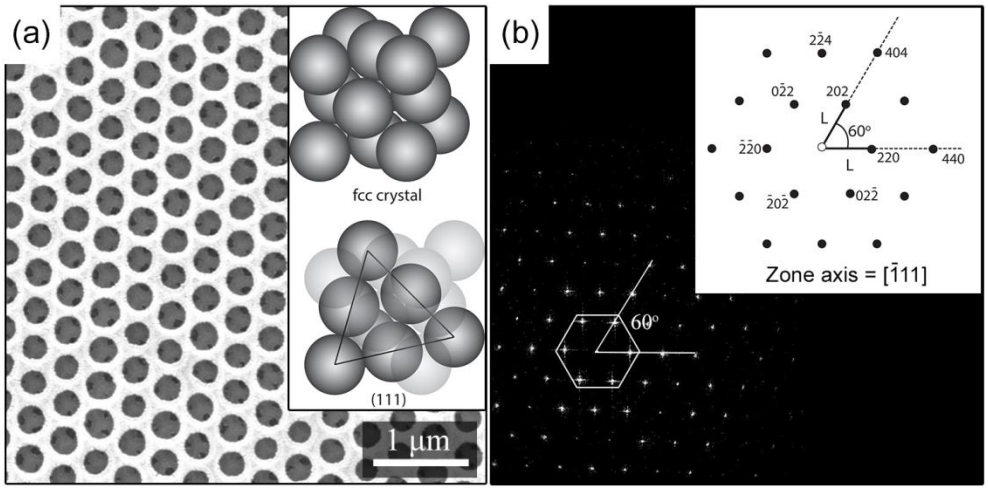

Figure 4-10: (a) An SEM image of a (111) crystal plane of an fcc crystal lattice; the inset shows the fcc arrangement of spheres and the (111) plane and (b) a 2D-FTT image of the SEM image in (a) and the inset represents the lattice points in the reciprocal lattice projected along the zone axis of $[\bar{1}11]$.

The reciprocal lattice vector is equal to the cosine value of the real space lattice vector. Also, the reciprocal lattice vector is equal to the interplanar distance (d) and the real lattice vector is equal to the center-to-center distance (a) of voids [**Equation (4-4)**]. Here, the reciprocal lattice vector is the same for all spots and the value is 0.34 µm/cycle. As reported by Blanford, et al., the reciprocal lattice vector of a two-dimensional diffraction pattern of an fcc crystal, projected on [111] axis, is the same for all spots. Moreover, the reciprocal lattice of an fcc crystal has a bcc lattice structure and this reciprocal lattice produces a hexagonal spot pattern around the zone axes of [111].[197] Inset of **Figure 4-10b** shows the appearance of the spots around the zone axis of $[\bar{1}11]$. The spots around the zone axis are lattice points. However, some of the lattice points in the reciprocal plane are forbidden and will not be visible in a diffraction pattern. For an example, points such as 011, 112, 110, 211, etc., will not appear in a diffraction pattern of an fcc lattice. Instead when the projected axis is $[\bar{1}11]$ then the lattice points of 202, 220, $02\bar{2}$, $\bar{2}0\bar{2}$, $\bar{2}\bar{2}0$, and $0\bar{2}2$ are seen on the resulting spot pattern.[197]

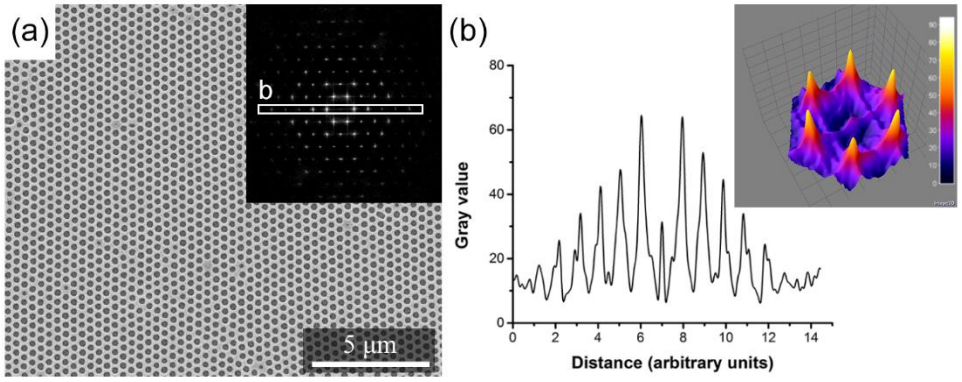

Figure 4-11: (a) An SEM image of a surface an inverse opal film, where inset shows the 2D-FFT pattern and the plot profile of the spots inside the box is labeled as b is shown at (b). The inset of (b) is the 3D profile of the first cycle of the FFT spot pattern, where the color represents the intensity of each spot.

The plot profile of a 2D-FFT image separates each spot based on their gray values. The white color has the highest gray value of 255 for an 8-bit grayscale image. In this analysis, the background was subtracted to remove any interference. This reduced the gray value of the spots as a whole but it reduces the background noise significantly. Since the highest brightness is for the spots at the first cycle, these spots have the highest gray value. **Figure 4-11** shows an SEM image of an inverse opal film with long-range order of porosity, where inset shows the 2D-FFT image. As seen in **Figure 4-11 b**, the plot profile of the spots inside the horizontal box in the FFT image (inset of **Figure 4-11a**), shows a symmetrical pattern of peaks with different gray values. The relative distance of each spot is projected with an arbitrary scale. Moreover, the profile is symmetric and the gray value of the spots decreases as they are positioned far away from the zone axis. The inset of **Figure 4-11b** is a three-dimensional profile of the first cycle of the FFT image. The color represents the gray value of each spot. The plot profiles showed in the **Figure 4-11b** are for an inverse opal film with long-range order of voids.

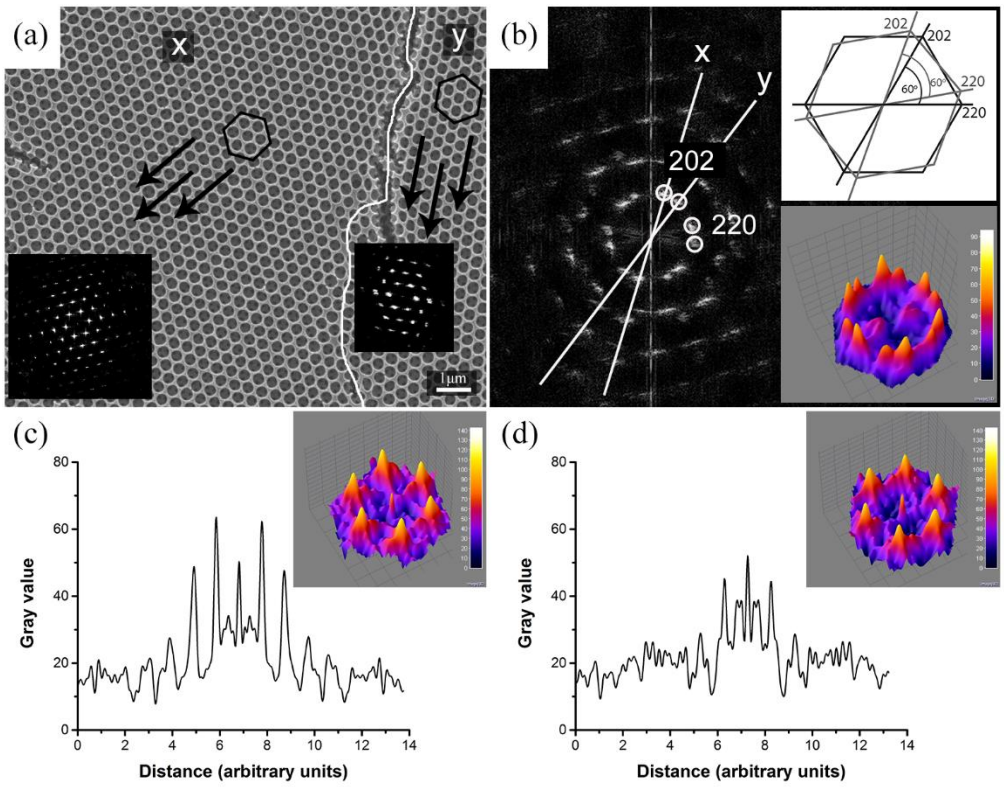

Figure 4-12: (a) An SEM image of an inverse opal film with two distinct domains including their 2D-FFT images, (b) The FFT analyzed image of the entire SEM image in (a) showing separation of two distinct spot patterns for the first cycle; the inset on top shows the shift of the spot pattern due to two distinct domains and bottom shows the 3D plot profile of the first cycle, (c) and (d) represent the plot profiles of spots at line x and y respectively.

An FFT image of a sample that has two domains consists of two different hexagonal arrangements of spots. Since both arrangements have the same reciprocal lattice vectors, the geometry of the hexagonal patterns should be the same. However, depending on the orientation of the domains the two spot patterns can be shifted from each other. If these two orientations are significantly different then the shift should be visible in the FFT analysis. In order to test this, an area of an inverse opal sample with two major domains was considered. The SEM image of this particular area is shown in **Figure 4-12a**, and the 2D-FFT analysis for each orientation is inserted at each place. The **Figure**

4-12b shows the FFT analysis for the entire SEM image. According to **Figure 4-12b,** there is a significant difference in the orientations of these two domains as the first cycle has 12 spots. The shift of the lattice point 202 and 220 is shown in the top inset of the **Figure 4-12b** and the orientation shift between the two patterns is measured to be 20°. The 3D profile of the gray values for the FFT analysis of the whole area showed doublets of peaks arranged around the zone axis. These doublets represent the orientation shift and one has higher gray value compared to the other. The higher gray value must correspond to the major domain (labeled as x in the **Figure 4-12a**) and the other is for the minor domain (y). The plot profiles of both x and y are shown in **Figure 4-12c** and **d** respectively.

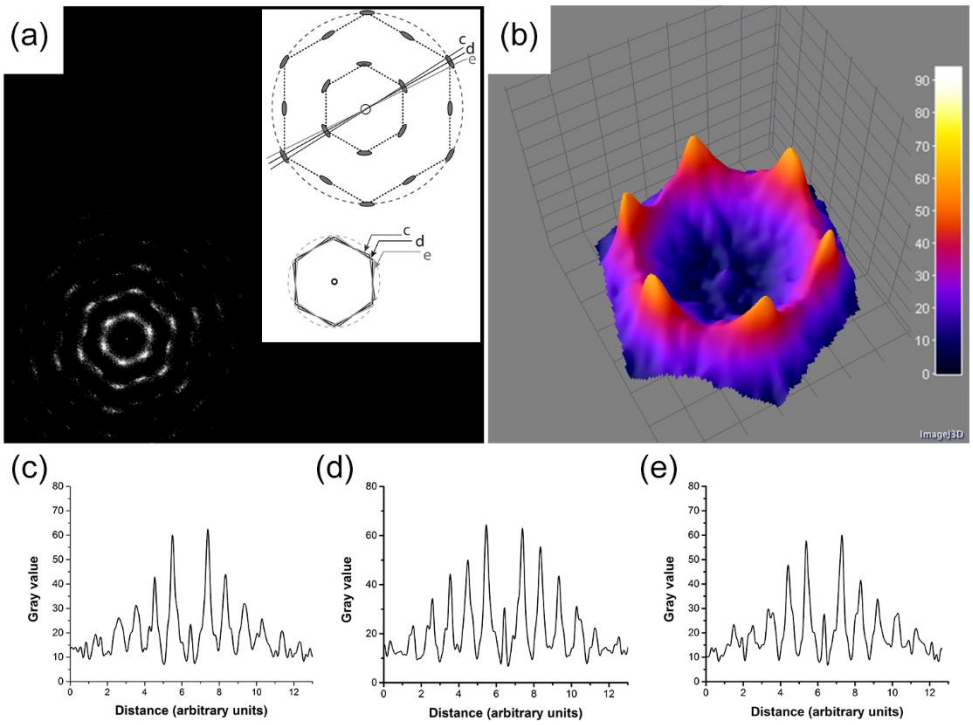

Figure 4-13: The 2D-FFT analysis for a sample with multiple domains: (a) 2D-FFT image, the inset shows the cartoon representation of the shift in the lattice orientation, (b) 3D-plot profile of the FFT image, (c), (d), and (e) the plot profiles obtained along the axes shown in (a) as c, d, and e respectively.

As seen in **Figure 4-13**, when the number of domains increases the spots in the FFT have an elongated shape. Also, **Figure 4-13b** is the 3D plot profiles taken for the FFT images of **Figure 4-13a**. The broad peaks result from multiple lattice orientations. Since the lattice orientation shift is small, the hexagonal arrangement is preserved. The plot profiles (**Figure 4-13c, d, and e**) also confirmed this observation as the individual patterns are similar to a lattice with one domain.

As seen in **Figure 4-14**, the split in the central peak (the zone axis) is due to a crack. The **Figure 4-14a** shows such an SEM image of an inverse opal film with a crack and **Figure 4-14b** shows the 3D plot profile with a split in the center peak. The **Figure 4-14c** shows an SEM image of a sample that has several cracks including a crack that separates the image into two. Even though there are many cracks still useful information about the orientation of the lattice can be obtained from the 3D plot profiles. However, the amount of cracks affects the intensities of the peaks.

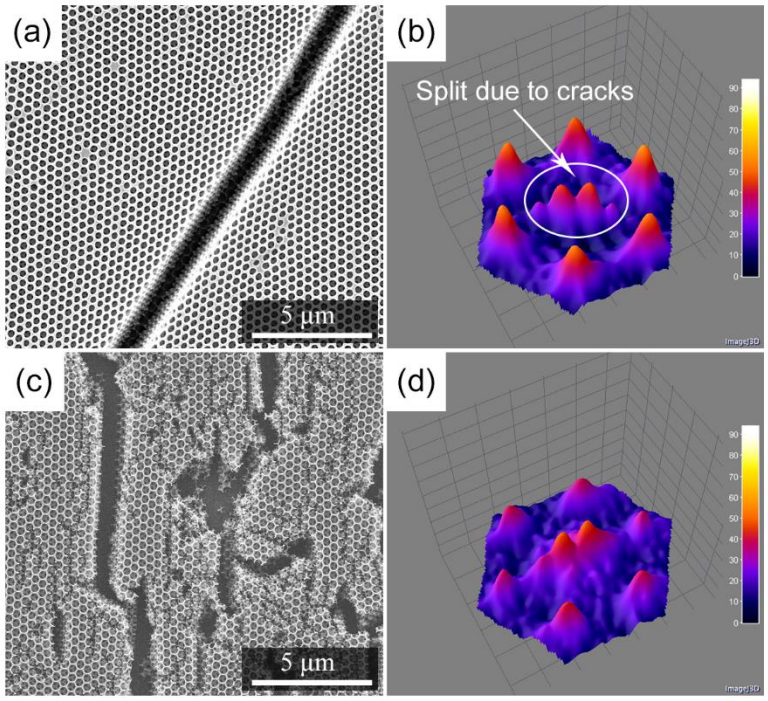

Figure 4-14: The 2D-FFT analysis of inverse opal films with cracks: (a) A crack that separates the SEM image into two, (b) 3D plot profile of (a), (c) an SEM image that shows multiple cracks, (d) 3D plot profile of (c).

4.4 Conclusion

Here, we conclude that the image analysis tools can be successfully used to obtain valuable information of the structure of inverse opal films. Furthermore, we have introduced a technique to determine the close-packed arrangement of voids and percentage of surface defects. According to our analysis, the structure of the inverse opal films depends on the ratio of colloids to tetraethyl orthosilicate. Most importantly, we have explained the presence of a significant gap between the voids and an extra surface layer of silica in some inverse opal samples. The surface filling fraction is increased with Col/TEOS ratio up to the ~0.6 and then decreased. Once the ratio is reached to 1.0, cracks started to appear in the resulting films. The quality of the films depends on the ratio of colloids to tetraethyl orthosilicate and when the ratio is ~0.6 the inverse opals with the best quality is obtained. We have also shown that the plot profiles of the 2D-FFT images can be successfully used to determine the periodicity in the presence of multiple lattice orientations.

CHAPTER V

FABRICATION OF POLY(2-HYDROXYETHYL METHACRYLATE)-BASED INVERSE OPAL HYDROGEL AS A POTENTIAL ORGANIC SOLVENT SENSOR

5.1 Introduction

The periodic microstructures in a photonic crystal diffract light and constructive interferences of the reflected waves determine the color of the material. Reversible changes in the refractive index or in the spacing of the grating, induced by an external stimulus, enable the use of photonic crystals in sensing applications. Visible color changes are possible with photonic sensors. Unlike inorganic colloidal structures, hydrogel photonic crystals can be made to be responsive to external stimulus by virtue of changing their chemistry. Hydrogels, three-dimensional network polymers, can reversibly absorb or desorb water by changing their volume. Most of these polymers are responsive to other organic solvents. The swelling of a hydrogel, resulting from absorption of large quantity of solvents, can be controlled by changing the composition of the monomers, functionalizing the surface, introducing new functional groups, or changing the cross-link density;[198, 199]

The fabrication of photonic hydrogels is challenging. Depending on the fabrication technique, the photonic hydrogel sensors are categorized into various types such as, holographic sensors,[200-203] crystalline colloidal array sensors,[83, 204, 205] and inverse opal sensors.[206-209] The inverse opal hydrogel sensors are relatively more advantageous than the other types due to high diffraction effi-

ciency.[210] Generally, inverse opal hydrogels are fabricated by infiltration of monomer mixtures to self-assembled colloidal crystals followed by the removal of the template. Poly(2-hydroxyethyl methacrylate) or poly(HEMA)-based hydrogels are synthetic hydrogels, which are widely used as inverse opal hydrogels due to their properties such as, high versatility,[211] easy preparation, optical transparency,[212, 213] biocompatibility,[214-216] etc. However, the poor sensitivity of poly(HEMA) - the homopolymer of HEMA - limits its potential uses in sensing applications. Therefore, various modifications have been introduced to improve the sensitivity of the poly(HEMA) hydrogels. For an example, co-polymerization of HEMA with other monomers such as acrylic acid,[217] 3-acrylamidophenylboronic acid,[34] and N-isopropylacrylamide for sensing pH, glucose, and temperature,[35] respectively. Since poly(HEMA) shows a noticeable response (swelling) to ethanol, the poly(HEMA) based hydrogels are studied as ethanol sensors[36]; however, they have not been thoroughly investigated for sensing other organic solvents. Furthermore, most fabrication techniques yield hydrogel inverse opal films with low mechanical stability which can be improved by transferring the hydrogel to another substrate.[218] Nevertheless, the transfer of the hydrogel creates problems in obtaining uniform swelling. Another strategy that can increase the mechanical and dimensional stability is to fabricate a thin zone of inverse opal structure on top of a bulk hydrogel.[219] The objective of this study is to fabricate poly(HEMA) based inverse opal hydrogels with high mechanical stability and to investigate their potential to use in sensing organic solvents.

A hydrogel composed of HEMA, N,N-(dimethylamino)ethyl methacrylate (DMAEMA), and tetraethylene glycol dimethacrylate (TEGDMA) was used to fabricate an inverse opal hydrogel. Opal films made out of silica colloids were used as the templates. Photo polymerization was used to polymerize the monomers. Here, a new simple methodology was introduced to yield inverse opal hydrogels with high mechanical strength by using a poly(dimethylsiloxane) (PDMS) mold. Moreover, the swelling behavior of the poly(HEMA/DMAEMA/TEGDMA) hydrogels was studied as a response to pH, and concentrations of salt (NaCl) in the aqueous solutions to evaluate the

potential of developing pH and salt sensors. As previously reported poly(HEMA/DMAEMA-/TEGDMA) hydrogels show significant swelling in organic solvents, such as N,N-dimethyl formamide (DMF), Dimethyl sulfoxide (DMSO), methanol, ethanol, and ethylene glycol.

5.2 Materials and methods

5.2.1 Materials and instruments

The silica particles (350 nm) were obtained as dry particles from NanoCym (Scottsdale, AZ). The silicon elastomer (PDMS - SYLGARD^{TM} 184) was purchased from Dow Corning (Midland, MI). The 2-hydroxyethyl methacrylate (HEMA, 97%), N,N-(dimethylaminoethyl)methacrylate (DMAEMA, 98%), 2-hydroxy-2-methylpropiophenone (97%), tetraethylene glycol dimethacrylate (TEGDMA, ≥ 90%), were obtained from Sigma-Aldrich (St. Louis, MO). Absolute ethyl alcohol (EtOH), ACS reagent grade hydrochloric acid (HCl, 36.5-38.0%), and sulfuric acid (H_2SO_4, 95.0-98%) were bought from Pharmco-AAPER (Brookfield, CT). ACS reagent grade hydrogen peroxide (H_2O_2, 30% (w/w)) was purchased from Ricca chemical company (Arlington, TX). Silicon wafers (p-type Si:B[100], R_o = (1-100) Ω cm) were acquired from El-Cat Inc. (Ridgefield Park, NJ). Microscope slides (premium) were purchased from Fisher Scientific (Fair Lawn, NJ). The surface of the substrates was treated using a corona treater (Electro-Technic Products, BD-20). The electron microscopy images were taken using a scanning electron microscope (SEM, FEI Quanta 600 FE). A convection oven (Binder ED 115) was used for the deposition of the silica opal films. Transmittance spectra were taken using a UV-Vis spectrophotometer (Cary 50 bioBio) in transmittance mode. The graphs were plotted using OriginPro 9 software (OriginLab Corporation). A water purification system (Barnstead Nanopure^{TM}), at a resistance of 18.1 Ω/cm, was used to obtain deionize water. The JT Baker® buffered oxide etchant [6:1 mixture of ammonium Fluoride (NH_4F) to hydrofluoric acid (HF)] was purchased from Capitol Scientific, Inc. (Austin, TX). The buffer oxide etching was conducted at Helmerich Research Center, OSU-Tulsa.

5.2.2 Methods

5.2.2.1 Synthesis of poly(HEMA/DMAEMA/TEGDMA) hydrogels

The hydrogel was prepared by thoroughly mixing HEMA, DMAEMA, TEGDMA and 2-hydroxy-2-methylpropiophenone in a ratio of 38:2:1:1 (mol/mol) respectively, with the solvent mixture containing water and ethylene glycol (1:1 mol/mol). The composition of the polymer was adapted from a study, previously published by You et al.[220]

5.2.2.2 Investigation of the swelling behavior of poly(HEMA/DMAEMA/TEGDMA) hydrogels as a response to pH and concentration of salt

The hydrogels (75 mm x 25 mm x 4 mm) were synthesized in PDMS molds and cut into small pieces with desired size (25 mm x 10 mm x 4 mm) to use in the experiment. The PDMS molds were prepared by mixing Sylgard^{TM} 184 silicone elastomer and curing agent (10:1 wt. %) and poured over the template, made from glass slides (75 mm x 25 mm x 4 mm), in a petri dish. Then the mixture was degassed in a vacuum to remove all the air bubbles, and thermally cured in an oven (Barnstead^{TM}) at 75 °C for 5 – 6 h. After fabrication, the hydrogel samples were purified in DI water for 4 days and dried in a vacuum desiccator until hydrogels reached a constant weight. The dehydrated hydrogels were immersed in solutions with different pH and salt concentrations for predetermined time periods (0, 10, 20, 30, 40, 50, 60, 70 and 80 min for pH solutions and 0, 70, 140, 350, 420, 660, and 1415 min for salt solutions). At the end of each time period, the hydrogels were taken out, blotted with a paper tissue to remove excess solution, and the weight was measured using an analytical balance. The swelling behavior of the hydrogel was investigated in different pH values between pH 2.2 and 7.0; the series of solutions was prepared by changing the pH in 0.4 increments. The buffer solutions were made using 0.2 M K_2HPO_4 and 0.1 M citric acid. As well, the swelling of the hydrogel was studied at different NaCl concentrations of 1.0, 0.1, and 0.01 M.

In both experiments, the percent mass swelling ratio ($\%Q_m$) was determined, by means of solvent uptake, at each time point using the following equation:

$$(\%Q_m) = \frac{(m_s - m_d)}{m_d} \times 100\% \qquad \textbf{(5-1)}$$

Here, m_s is the mass of the swollen hydrogel, and m_d is the mass of the dry hydrogel.

5.2.2.3 Fabrication of silica opal thin films

Silica colloids (350 nm) were dispersed in absolute ethanol to prepare the working solution. The concentration of colloids in the working solution was 20 mg/mL. Then a substrate, glass or silicon wafer, was dipped in a vial containing the silica colloid suspension and heated in a convection oven at 65 °C for 24 h to evaporate the solvent.

5.2.2.4 Fabrication of inverse opal hydrogels

A schematic representation of the fabrication process of inverse opal hydrogels is shown in **Figure 5.1**. Briefly, a PDMS mold was fabricated using a glass template. After removing the template, a silica opal film fabricated on a glass slide or a silicon wafer was placed in the well, the monomer mixture was poured over the opal film and cured with 365 nm UV light for 90 s using a Dymax™ light curing system (225 mW/cm^2, Model 5000 Flood). The hydrogel-silica composite, peeled off from the PDMS mold, was trimmed to remove the excess hydrogel. To separate the silicon wafers from the composite, the composites were submerged in DI water for 24 h. Finally, the hydrogel-silica composite with the glass substrate and the composites (separated from silicon wafers) were subjected to 2% HF etching (etched on buffered oxide (6:1 mixture of NH_4F to HF) until the substrate is detached from the hydrogel - ~2 days) to remove the silica beads. The glass slides were expected to detach from the composite during HF etching.

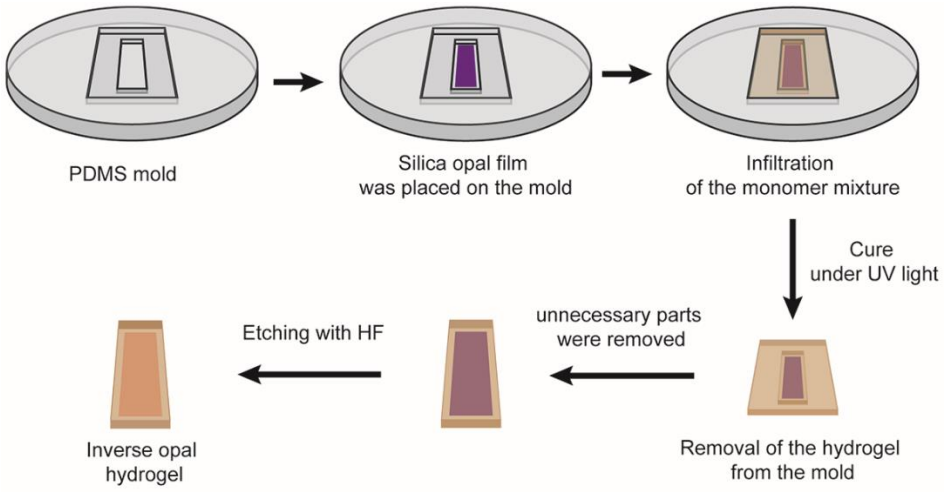

Figure 5-1: The schematic representation of the fabrication of inverse opal hydrogels.

5.3 Results and discussion

5.3.1 Swelling behavior of the poly(HEMA/DMAEMA/TEGDMA) hydrogel in response to pH and concentration of salt

The swelling behavior of the poly(HEMA/DMAEMA/TEGDMA) hydrogel with pH of the medium is mainly due to the presence of N,N-(dimethylamino)ethyl methacrylate (DMAEMA) monomer units. The pKa of DMAEMA is 8.44,[221] and poly(N,N-(dimethylamino)ethyl methacrylate) [poly(DMAEMA)] is 7.5.[222] Thus the pH response for poly(HEMA/DMAEMA/TEGDMA) hydrogel can be expected in acidic pH. In this study, the swelling behavior of poly(HEMA/-DMAEMA/TEGDMA) hydrogel in response to pH was evaluated in solvents having pH values of from 2.2 to 7.0 with 0.4 increments. The hydrogel showed a small change in $\%Q_m$ (< 20%) in response to pH. The mass swelling ratio followed a similar trend as shown in **Figure 5-2a**, in all solutions regardless of the pH value. As shown by the graph in **Figure 5-2b**, the increase in pH caused decrease in swelling from 18% (at pH 2.2) to 8% (at pH 7.0). Since the pH of the solution was maintained at the desired value using buffers, the salts (ionic strength) might have influenced the swelling of the hydrogels.[223, 224]

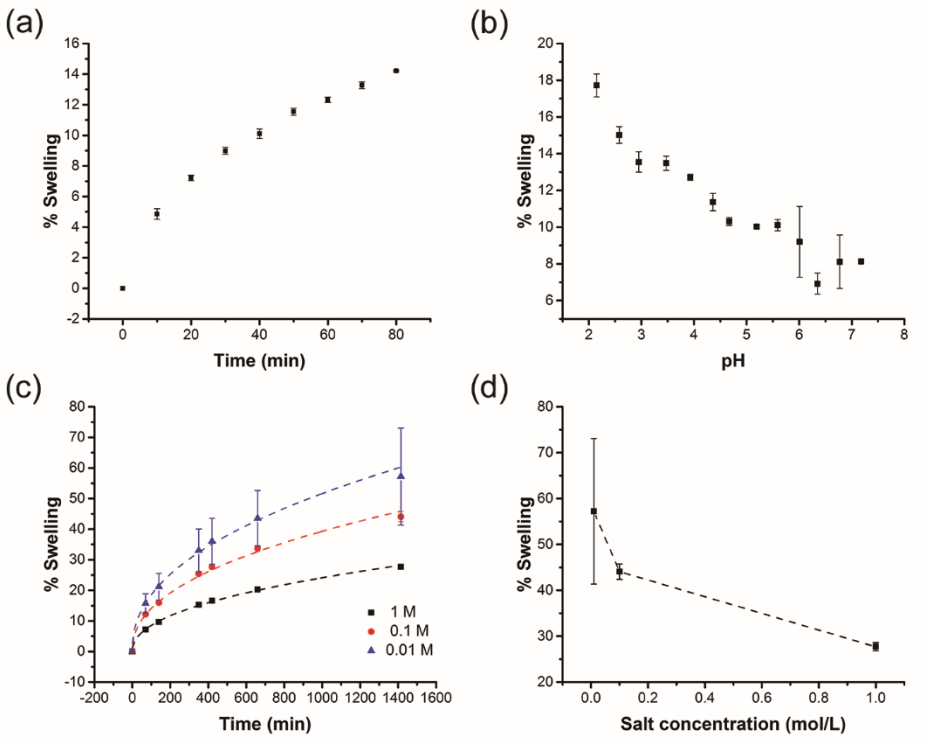

Figure 5-2: Mass swelling ratio ($\%Q_m$) as a function of (a) time at pH 5.6, (b) pH at 40 min, (c) time in salt solutions with different salt (NaCl) concentrations, and (d) concentration of salt (NaCl) at 1415 min (24 h).

To analyze the swelling behavior of poly(HEMA/DMAEMA/TEGDMA) hydrogel, the samples were swollen in 1.0, 0.1, and 0.01 M NaCl solutions. The $\%Q_m$ was remarkably increased with time at the lowest concentration of NaCl (0.01 M) used in the experiment. In each NaCl solution, the swelling was rapid at the beginning (up to ~70 min) and then slowed (**Figure 5-2c**). It has been shown that the swelling of hydrogels has a prominent effect from the ionic strength of the surrounding environment.[223, 224] Availability of water decreases as the salt concentration increases, which may also contribute to the decrease in swelling.

5.3.2 Fabrication of silica opal films

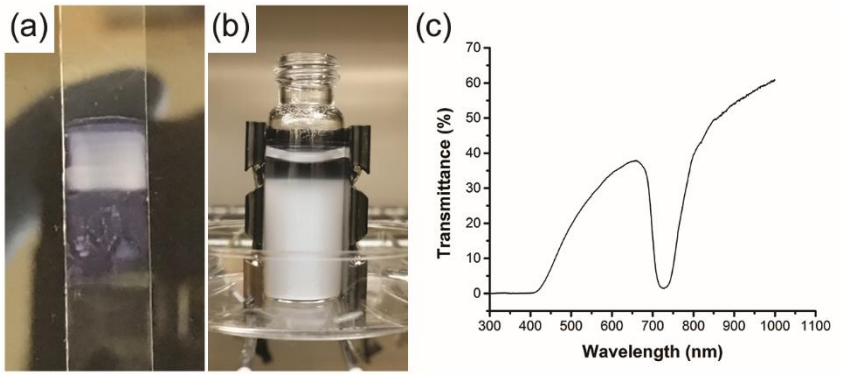

Figure 5-3: (a) A silica opal film fabricated on a glass slide; (b) A glass vial containing silica dispersed in water (8 mg/mL) kept undisturbed for 12 h; (c) Transmittance spectrum of a silica opal film made out of silica colloids dispersed in water.

The silica opal films were fabricated on glass slides using vertical deposition technique, where the samples were heated at 55 ºC in an oven for 24 h. Even though, the silica particles were well dispersed in water by agitation and sonication at the beginning of the experiment, ~1/4 volume fraction of silica colloids was settled within 12 h. The poor stability of silica colloids in water resulted in short opal films (2-3 cm) (**Figure 5-3**). The size of the colloids used in this experiment was 350 nm and a stopband was observed at 730 nm for the fabricated opal film. Since there is a relationship between the size of the particles and the position of the stopband, for a first order reflection, the expected stopband wavelength (λ) can be determined from the following equation;

$$\lambda = 1.632D[\phi n_s + (1-\phi)n_a] \qquad \textbf{(5-2)}$$

Here, D is the size of the particles, m is the order of the incident light, ϕ is the volume fraction of the matrix (air), n_s is the refractive index of the silica, and n_a is the refractive index of air. For silica opal films with perfect close-packed arrangement of colloids (ϕ = 0.74) and the expected position of the stopband is 765 nm.

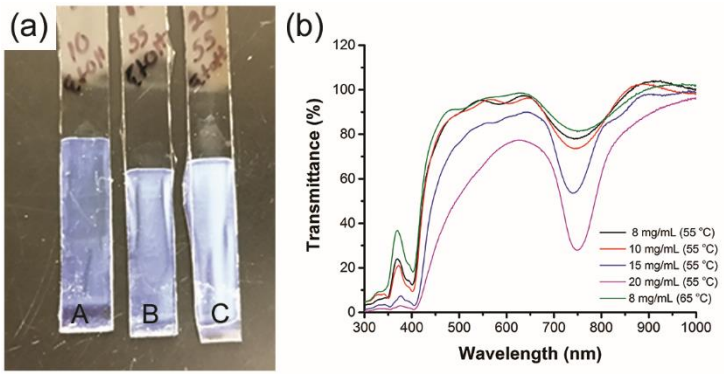

Figure 5-4: (a) Three silica opal films fabricated with silica colloids dispersed in ethanol; the concentrations of silica was (A) 8 mg/mL, (B) 10 mg/mL, and (C) 20 mg/mL; (b) transmittance spectra obtain for the silica opal films made with different concentrations of silica.

According to the previous studies, ethanol is another solvent which can be used to disperse silica colloids.[218, 225, 226] In contrast to water-dispersed silica colloids, which yielded short opal films, silica colloids dispersed in ethanol resulted in long opal films (> 5 cm). Four dispersions with different concentrations of colloids (8, 10, 15, and 20 mg/mL) were used to fabricate the opal films. The temperature also had an influence on the intensity of the stopband and 55 °C was found as the optimum temperature. According to the observations (**Figure 5-4**) the best films were fabricated in solutions with 20 mg/mL of colloids at 55 °C. As seen in **Figure 5-4**, the intensity of the stopband increased with increasing silica concentration. However, beyond 20 mg/mL significant further improvement was not achieved. It is difficult to disperse silica particles entirely in ethanol, at high concentrations. Compared to the silica opal films fabricated with water as the dispersant, the opal films made in ethanol as the dispersant showed less intense stopbands. Usually, the intensity of the stopband depends on the number of layers of the thin film (**Chapter 3**). However, the position of the stopband is 750 nm, which is closer to the expected value (765 nm). The position of the stopband is an indication of the better close-packing of silica particles.

5.3.3 Fabrication of inverse opal hydrogels

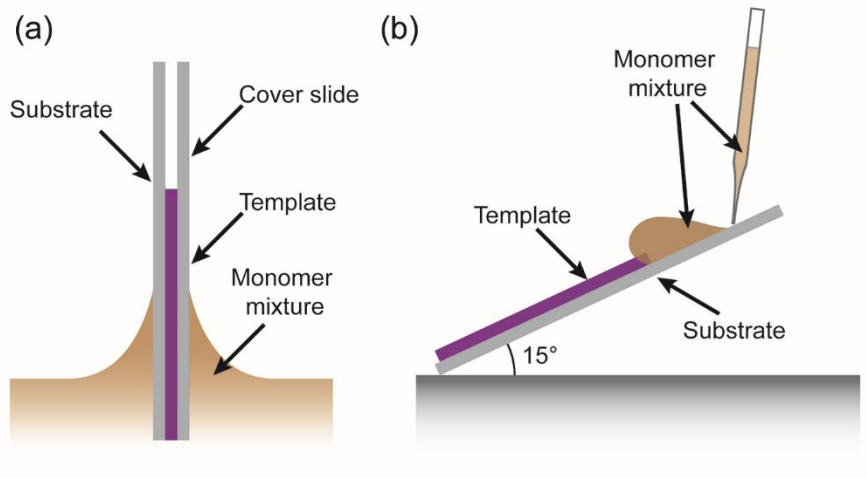

Figure 5-5: Two general methods were used for the infiltration of a monomer mixture to an opal film: (a) opal film is covered with a cover slide and dipped in the monomer mixture, where the monomers infiltrate into the interstitial sites *via* capillary forces and (b) the opal film is held at an angle of ~15°, and the monomer mixture is poured on top of the film and the excess solution is allowed to drain.

The two conventional methods used to infiltrate monomer mixtures to hydrogels are shown in **Figure 5-5**. In the first method, the silica opal film is covered with another slide and partially immersed in the monomer mixture.[227] The second method uses a silica opal film inclined at an angle ~15° and the monomer mixture is dropped onto the top of slide and the excess is drained.[36] The resulting inverse opal hydrogels fabricated from both methods are thin and difficult to handle. In this study, a new, alternative methodology was introduced to infiltrate the hydrogel, using a PDMS mold, where we had more control over the thickness of the resulting films. Here, a PDMS mold was prepared with a well (the depth was 2 mm) to place the silica opal film (**Figure 5-1**). Once the monomer mixture is poured into the well and photopolymerized the composite film can be detached from the mold. The resulting inverse opal hydrogel, after removing the silica template,

has two zones: a thin zone with the inverse opal structure (patterned zone), and a thick zone in which only the polymer is present with no structure (unpatterned zone). The thin, patterned zone containing the inverse opal structure is responsible for the sensing applications while the thick, unpatterned zone provides the mechanical stability and dimensional stability. The thickness of the unpatterned zone can be controlled by changing the depth of the well in the PDMS mold. Moreover, this unpatterned zone aids the diffusion of the analytes toward the patterned sensing region. However, the infiltration of the monomer mixture was poor in this new method; but, can be significantly improved by leaving the monomer-filled PDMS molds under a vacuum in a desiccator for 48 h. As well, the removal of the hydrogel from the substrate, without damaging the inverse opal structure, was also challenging.

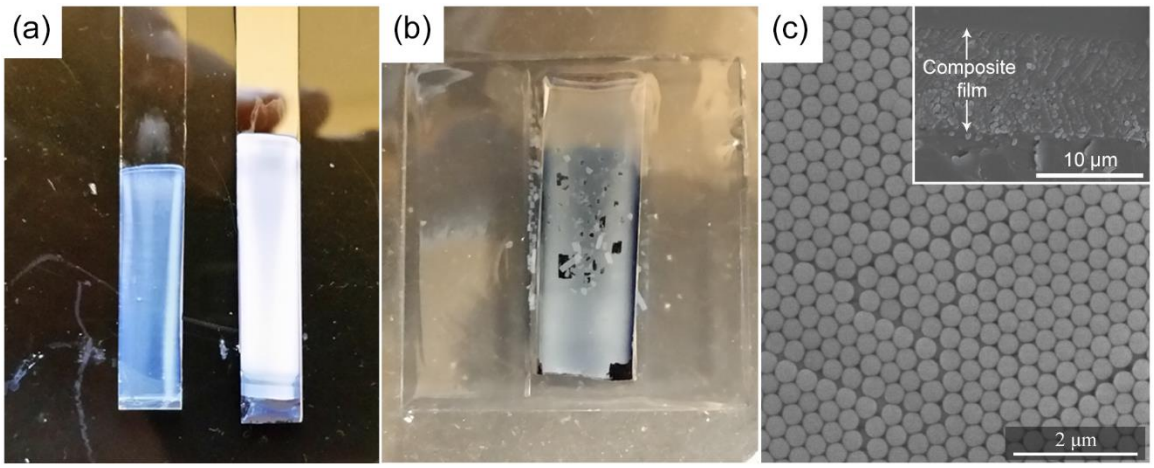

Figure 5-6: (a) Silica opal film fabricated on a glass slide (left) and a silicon wafer (right); (b) Hydrogel-silica opal composite made, using a PDMS mold, by infiltrating the monomer mixture for 24 h; (c) An SEM image of a silica opal film fabricated on a glass slide and the inset shows an SEM image of a silica opal-hydrogel composite film (infiltrated for 48 h with the monomer mixture).

Initially, the hydrogel was mechanically peeled off or immersed in a solvent i.e. water or ethanol to separate the substrate from the silica opal-hydrogel composite film by swelling the hydrogel. The glass substrate was hard to separate from the composite either mechanically or by swelling in a solvent. On the contrary, the silicon wafer substrate was easy to remove from the composite by swelling the hydrogel in DI water, which can be attributed to the weak interactions between the silica colloids and silicon surface. However, the silica opal film started to peel off from some places upon leaving in contact with the monomer mixture for 48 h in a vacuum desiccator **(Figure 5-6)**. Since it is essential to keep the opal film in the monomer mixture for 48 h in a vacuum desiccator for a better infiltration, glass slides were used as the substrate in future experiments. After fabrication, the silica-hydrogel composites were separated from the glass slide by using a 2% HF solution (soaked in the HF solution for ~2 days). Once the substrate was separated from the composite, the composite was soaked in HF solution for another 24 h for the completion of the etching of the silica colloidal template. As seen in **Figure 5-7**, the template was successfully etched from the silica opal-hydrogel composites made by infiltrating the monomer mixture for 48 h.

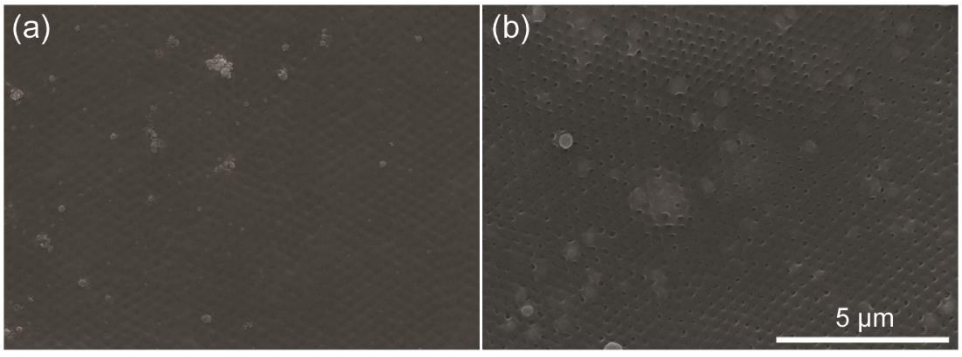

Figure 5-7: Hydrogel films after etched in HF solutions: (a) the hydrogel monomer mixture was infiltrated for few mins; (b) the monomer mixture was infiltrated for 48 h in a vacuum desiccator.

5.4 Conclusion and future directions

This study introduces a new methodology to fabricate inverse opal hydrogels which can be used as a potential sensor to detect organic solvents. This fabrication involves several steps: fabrication of silica opal films, infiltration of the monomer mixture, photopolymerization of monomers to synthesize the polymer, and removal of the template. Here, it is shown that silica particles dispersed in ethanol can be successfully used to fabricate long silica opal films with a good quality, using both glass microscope slides and silicon wafers as the substrate for the opal films. Even though the silicon substrate was easily removed from the opal-hydrogel composite by swelling the hydrogel, the stability of the opal film was poor when the monomer mixture is not infiltrated for 48 h in a vacuum. Therefore, the use of glass as the substrate for fabricating opal films was advantageous in this new method. Moreover, the glass substrate and the silica opal template were simultaneously removed from the composite by HF etching. Since the poly(HEMA/DMAEMA/TEGDMA) inverse opal hydrogels has a response to organic solvents such as N,N-dimethyl formamide (DMF), Dimethyl sulfoxide (DMSO), methanol, ethanol, and ethylene glycol an inverse opal hydrogel sensor can be fabricated. As well, a shift of the stopband might be observed in response to the salt concentration as the poly(HEMA/DMAEMA/TEGDMA) hydrogel showed a notable change in swelling at low salt concentrations; thus the potential of this inverse opal hydrogel to be used in salt sensing applications can also be evaluated.

REFERENCES

1. Srinivasarao, M., Nano-Optics in the Biological World: Beetles, Butterflies, Birds, and Moths. *Chemical Reviews* **1999,** *99* (7), 1935-1962.

2. Yablonovitch, E., Inhibited Spontaneous Emission in Solid-State Physics and Electronics. *Physical Review Letters* **1987,** *58* (20), 2059-2062.

3. John, S., Strong localization of photons in certain disordered dielectric superlattices. *Physical Review Letters* **1987,** *58* (23), 2486-2489.

4. John, S.; Quang, T., Collective Switching and Inversion without Fluctuation of Two-Level Atoms in Confined Photonic Systems. *Physical Review Letters* **1997,** *78* (10), 1888-1891.

5. Mekis, A.; Chen, J. C.; Kurland, I.; Fan, S.; Villeneuve, P. R.; Joannopoulos, J. D., High Transmission through Sharp Bends in Photonic Crystal Waveguides. *Physical Review Letters* **1996,** *77* (18), 3787-3790.

6. Lin, S.-Y.; Chow, E.; Hietala, V.; Villeneuve, P. R.; Joannopoulos, J. D., Experimental Demonstration of Guiding and Bending of Electromagnetic Waves in a Photonic Crystal. *Science* **1998,** *282* (5387), 274-276.

7. Haibin, N.; Ming, W.; Wei, C., Sol-gel co-assembly of hollow cylindrical inverse opals and inverse opal columns. *Optics Express* **2011,** *19* (27), 25900-25910.

8. Ni, H.; Wang, M.; Li, L.; Chen, W.; Wang, T., Photonic-Crystal-Based Optical Fiber Bundles and Their Applications. *IEEE Photonics Journal* **2013,** *5* (4), 2400213-2400213.

9. Wadsworth, W. J.; Percival, R. M.; Bouwmans, G.; Knight, J. C.; Russell, P. S. J., High power air-clad photonic crystal fibre laser. *Optics Express* **2003,** *11* (1), 48-53.

10. Altug, H.; Vučković, J., Photonic crystal nanocavity array laser. *Optics Express* **2005,** *13* (22), 8819-8828.

11. Hirose, K.; Liang, Y.; Kurosaka, Y.; Watanabe, A.; Sugiyama, T.; Noda, S., Watt-class high-power, high-beam-quality photonic-crystal lasers. *Nature Photonics* **2014,** *8*, 406-411.

12. Lin, S. Y.; Fleming, J. G.; Hetherington, D. L.; Smith, B. K.; Biswas, R.; Ho, K. M.; Sigalas, M. M.; Zubrzycki, W.; Kurtz, S. R.; Bur, J., A three-dimensional photonic crystal operating at infrared wavelengths. *Nature* **1998,** *394*, 251-253.

13. Qi, M.; Lidorikis, E.; Rakich, P. T.; Johnson, S. G.; Joannopoulos, J. D.; Ippen, E. P.; Smith, H. I., A three-dimensional optical photonic crystal with designed point defects. *Nature* 2004, 429, 538.

14. Lai, N. D.; Liang, W. P.; Lin, J. H.; Hsu, C. C.; Lin, C. H., Fabrication of two- and three-dimensional periodic structures by multi-exposure of two-beam interference technique. *Optics Express* **2005**, 13 (23), 9605-9611.

15. Aoki, K.; Miyazaki, H. T.; Hirayama, H.; Inoshita, K.; Baba, T.; Sakoda, K.; Shinya, N.; Aoyagi, Y., Microassembly of semiconductor three-dimensional photonic crystals. *Nature Materials* **2003**, 2, 117.

16. Meseguer, F.; Blanco, A.; Míguez, H.; García-Santamaría, F.; Ibisate, M.; López, C., Synthesis of inverse opals. *Colloids and Surfaces A: Physicochemical and Engineering Aspects* **2002,** *202* (2), 281-290.

17. Edrington, A. C.; Urbas, A. M.; DeRege, P.; Chen, C. X.; Swager, T. M.; Hadjichristidis, N. , Xenidou, M.; Fetters, L. J.; Joannopoulos, J. D.; Fink, Y.; Thomas, E. L., Polymer-Based Photonic Crystals. *Advanced Materials* **2001**, 13 (6), 421-425.

18. Galisteo-López, J. F.; Ibisate, M.; Sapienza, R.; Froufe-Pérez, L. S.; Blanco, Á.; López, C., Self-Assembled Photonic Structures. *Advanced Materials* **2011**, 23 (1), 30-69.

19. Whitesides, G. M.; Grzybowski, B., Self-Assembly at All Scales. *Science* **2002**, 295 (5564), 2418-2421.

20. Hatton, B.; Mishchenko, L.; Davis, S.; Sandhage, K. H.; Aizenberg, J., Assembly of large-area, highly ordered, crack-free inverse opal films. *Proceedings of the National Academy of Sciences of the United States of America* **2010**, 107 (23), 10354-10359.

21. Hernán, M.; Francisco, M.; Cefe, L.; Álvaro, B.; S., M. J.; Joaquín, R.; Amparo, M.; Vicente, F., Control of the Photonic Crystal Properties of fcc-Packed Submicrometer SiO2 Spheres by Sintering. *Advanced Materials* **1998**, 10 (6), 480-483.

22. Wong, S.; Kitaev, V.; Ozin, G. A., Colloidal Crystal Films: Advances in Universality and Perfection. *Journal of the American Chemical Society* **2003**, 125 (50), 15589-15598.

23. Miguez, H.; Tetreault, N.; Hatton, B.; Yang, S. M.; Perovic, D.; Ozin, G. A., Mechanical stability enhancement by pore size and connectivity control in colloidal crystals by layer-by-layer growth of oxide. *Chemical Communications* **2002,** (22), 2736-2737.

24. Wang, L.; Zhao, X. S., Fabrication of Crack-Free Colloidal Crystals Using a Modified Vertical Deposition Method. *The Journal of Physical Chemistry C* **2007,** *111* (24), 8538-8542.

25. Vos, W. L.; Megens, M.; van Kats, C. M.; Bösecke, P., X-ray Diffraction of Photonic Colloidal Single Crystals. *Langmuir* **1997,** *13* (23), 6004-6008.

26. Megens, M.; van Kats, C. M.; Bösecke, P.; Vos, W. L., In Situ Characterization of Colloidal Spheres by Synchrotron Small-Angle X-ray Scattering. *Langmuir* **1997,** *13* (23), 6120-6129.

27. Holland, B. T.; Blanford, C. F.; Stein, A., Synthesis of Macroporous Minerals with Highly Ordered Three-Dimensional Arrays of Spheroidal Voids. *Science* **1998,** *281* (5376), 538-540.

28. Zhou, W. L.; Xu, L.; Zakhidov, A. A.; Baughman, R. H.; Wiley, J. B., Structure and Nanocrystallites of Ni and NiO Three Dimensional Ordered Macromeshes. *MRS Proceedings* **2011,** *703*, V9.19.

29. Yan, H.; Zhang, K.; Blanford, C. F.; Francis, L. F.; Stein, A., In Vitro Hydroxycarbonate Apatite Mineralization of $CaO{-}SiO_2$ Sol−Gel Glasses with a Three-Dimensionally Ordered Macroporous Structure. *Chemistry of Materials* **2001,** *13* (4), 1374-1382.

30. Cheng, B.; Ni, P.; Jin, C.; Li, Z.; Zhang, D.; Dong, P.; Guo, X., More Direct Evidence of the fcc Arrangement for Artificial Opal. *Optics Communications* **1999,** *170* (1), 41-46.

31. Míguez, H.; Meseguer, F.; López, C.; Mifsud, A.; Moya, J. S.; Vázquez, L., Evidence of FCC Crystallization of SiO_2 Nanospheres. *Langmuir* **1997,** *13* (23), 6009-6011.

32. Nishijima, Y.; Juodkazis, S., Optical Characterization and Lasing in Three-Dimensional Opal-Structures. *Frontiers in Materials* **2015,** *2* (49).

33. Lee, Y.-J.; Braun, P.V.; Tunable Inverse Opal Hydrogel pH Sensors. *Advanced Materials* **2003,** *15* (7-8), 563-566.

34. Lee, Y.-J.; Pruzinsky, S. A.; Braun, P. V., Glucose-Sensitive Inverse Opal Hydrogels: Analysis of Optical Diffraction Response. *Langmuir* **2004,** *20* (8), 3096-3106.

35. Shin, J.; Han, S. G.; Lee, W., Dually tunable inverse opal hydrogel colorimetric sensor with fast and reversible color changes. *Sensors and Actuators B: Chemical* **2012,** *168*, 20-26.

36. Pernice, R.; Adamo, G.; Stivala, S.; Parisi, A.; Busacca, A. C.; Spigolon, D.; Sabatino, M. A.; D'Acquisto, L.; Dispenza, C., Opals infiltrated with a stimuli-responsive hydrogel for ethanol vapor sensing. *Optical Materials Express* **2013,** *3* (11), 1820-1833.

37. Jayasinghe, H. G.; Tormos, C. J.; Khan, M.; Madihally, S.; Vasquez, Y., A soft lithography method to generate arrays of microstructures on hydrogel surfaces. *Journal of Polymer Science Part B* **2018**, 56: 1144-1157.

38. Vukusic, P.; Sambles, J. R., Photonic structures in biology. *Nature* **2003,** *424*, 852.

39. Parker, A. R., Natural photonic engineers. *Materials Today* **2002,** *5* (9), 26-31.

40. Johnson, S. G.; Joannopoulos, J. D., Designing synthetic optical media: photonic crystals. *Acta Materialia* **2003,** *51* (19), 5823-5835.

41. Stavenga, D. G.; Otto, J. C.; Wilts, B. D., Splendid coloration of the peacock spider Maratus splendens. *Journal of The Royal Society Interface* **2016,** *13* (121).

42. Song, C. X.; Liu, F.; Hao, Y. H.; Hu, X. H.; Zhang, Y. F.; Liu, X. H., Multilayer manipulated diffraction in flower beetles Torynorrhina flammea: intraspecific structural colouration variation. *Journal of Optics* **2014,** *16* (10), 105302.

43. Andrew Richard, P.; Zoltan, H., Diffractive optics in spiders. *Journal of Optics A: Pure and Applied Optics* **2003,** *5* (4), S111.

44. Hinton, H. E.; Gibbs, D. F.; Silberglied, R., Stridulatory files as diffraction gratings in mutillid wasps. *Journal of Insect Physiology* **1969,** *15* (4), 549-552.

45. Yoshioka, S.; Kinoshita, S., Wavelength-selective and anisotropic light-diffusing scale on the wing of the Morpho butterfly. *Proceedings of the Royal Society B: Biological Sciences* **2004,** *271* (1539), 581-587.

46. Zi, J.; Yu, X.; Li, Y.; Hu, X.; Xu, C.; Wang, X.; Liu, X.; Fu, R., Coloration Strategies in Peacock Feathers. *Proceedings of the National Academy of Sciences* **2003,** *100* (22), 12576-12578.

47. Morimoto, G.; Yamaguchi, N.; Ueda, K., Plumage Color as a Status Signal in Male–male Interaction in the Red-flanked Bushrobin, *Tarsiger cyanurus*. *Journal of Ethology* **2006,** *24* (3), 261-266.

48. Tsuyoshi, U.; Garuda, F.; Gen, M.; Kiyoshi, M.; Akinori, K.; Takeo, K.; Takahiko, H., Numerical Study on the Structural Color of Blue Birds by a Disordered Porous Photonic Crystal Model. *Europhysics Letters* **2014,** *107* (3), 34004.

49. Saranathan, V.; Forster, J. D.; Noh, H.; Liew, S.-F.; Mochrie, S. G. J.; Cao, H.; Dufresne, E. R.; Prum, R. O., Structure and Optical Function of Amorphous Photonic Nanostructures from Avian Feather Barbs: A Comparative Small Angle X-ray Scattering (SAXS) Analysis of 230 Bird Species. *Journal of The Royal Society Interface* **2012,** *9* (75), 2563-2580.

50. Sanders, J. V., Colour of Precious Opal. *Nature* **1964,** *204*, 1151–1153.

51. Aizenberg, J.; Tkachenko, A.; Weiner, S.; Addadi, L.; Hendler, G., Calcitic Microlenses as Part of the Photoreceptor System in Brittlestars. *Nature* **2001,** *412*, 819-822.

52. Armstrong, S., Photonic Crystals Aid Fish's Night Vision, *Nature Photonics* **2012,** *6*, 575.

53. Gur, D.; Politi, Y.; Sivan, B.; Fratzl, P.; Weiner, S.; Addadi, L., Guanine-Based Photonic Crystals in Fish Scales Form from an Amorphous Precursor. *Angewandte Chemie International Edition* **2013,** *52* (1), 388-391.

54. Sukhoivanov, I. A.; Guryev, I. V., Introduction to Photonic Crystals. In *Photonic Crystals: Physics and Practical Modeling*, Sukhoivanov, I. A.; Guryev, I. V., Eds. Springer Berlin Heidelberg: Berlin, Heidelberg, 2009; pp 1-12.

55. Noda, S.; Tomoda, K.; Yamamoto, N.; Chutinan, A., Full Three-Dimensional Photonic Bandgap Crystals at Near-Infrared Wavelengths *Science* **2000**, 289 (5479), 604-606.

56. Ho, K. M.; Chan, C. T.; Soukoulis, C. M.; Biswas, R.; Sigalas, M., Photonic band gaps in three dimensions: New layer-by-layer periodic structures. *Solid State Communications* **1994**, 89 (5), 413-416.

57. Fleming, J. G.; Lin, S.-Y., Three-dimensional photonic crystal with a stop band from 1.35 to 1.95 μm. *Optics Letters* **1999**, 24 (1), 49-51.

58. Megens, M.; Wijnhoven, J. E. G. J.; Lagendijk, A.; Vos, W. L., Fluorescence lifetimes and linewidths of dye in photonic crystals. *Physical Review A* **1999**, 59 (6), 4727-4731.

59. Noda, S.; Imada, M.; Okano, M.; Ogawa, S.; Mochizuki, M.; Chutinan, A., Semiconductor three-dimensional and two-dimensional photonic crystals and devices. *IEEE Journal of Quantum Electronics* **2002**, 38 (7), 726-735.

60. Ogawa, S.; Imada, M.; Noda, S., Analysis of thermal stress in wafer bonding of dissimilar materials for the introduction of an InP-based light emitter into a GaAs-based three-dimensional photonic crystal. *Applied Physics Letters* **2003**, 82 (20), 3406-3408.

61. Soukoulis, C. M., Photonic band gap materials: the "semiconductors" of the future? *Physica Scripta* **1996,** *1996* (T66), 146.

62. Ogawa, S.; Imada, M.; Yoshimoto, S.; Okano, M.; Noda, S., Control of Light Emission by 3D Photonic Crystals. *Science* 2004, 305 (5681), 227-229.

63. Lee, W.; Pruzinsky, S; Braun, P. Multi-Photon Polymerization of Waveguide Structures Within Three-Dimensional Photonic Crystals. *Advanced Materials* **2002,** *14* (4), 271-274.

64. Taton, T. A.; Norris, D. J., Defective Promise in Photonics. *Nature* **2002,** *416*, 685-686.

65. Joannopoulos, J. D.; Villeneuve, P. R.; Fan, S., Photonic Crystals: Putting a New Twist on Light. *Nature* **1997,** *386*, 143-149.

66. Yan, Q.; Wang, L.; Zhao, X. S.; Artificial Defect Engineering in Three-Dimensional Colloidal Photonic Crystals. *Advanced Functional Materials* **2007,** *17* (18), 3695-3706.

67. Notomi, M.; Shinya, A.; Mitsugi, S.; Kuramochi, E.; Ryu, H. Y., Waveguides, Resonators and Their Coupled Elements in Photonic Crystal Slabs. *Opt. Express* **2004,** *12* (8), 1551-1561.

68. Arsenault, A. C.; Puzzo, D. P.; Manners, I.; Ozin, G. A., Photonic-crystal Full-colour Displays. *Nature Photonics* **2007,** *1*, 468-472.

69. Zheng, X.; Meng, S.; Chen, J.; Wang, J.; Xian, J.; Shao, Y.; Fu, X.; Li, D., Titanium Dioxide Photonic Crystals with Enhanced Photocatalytic Activity: Matching Photonic Band Gaps of TiO2 to the Absorption Peaks of Dyes. *The Journal of Physical Chemistry C* **2013,** *117* (41), 21263-21273.

70. Darwin, C. G., XXXIV. The theory of X-ray reflexion. *The London, Edinburgh, and Dublin Philosophical Magazine and Journal of Science* **1914,** *27* (158), 315-333.

71. Joannopoulos, J. D.; Johnson, S. G.; Winn, J. N.; Meade, R. D., *Photonic Crystals: Molding the Flow of Light, Second Edition*. Princeton University Press: 2011.

72. Armstrong, E.; O'Dwyer, C., Artificial Opal Photonic Crystals and Inverse Opal Structures - Fundamentals and Applications from Optics to Energy Storage. *Journal of Materials Chemistry C* **2015,** *3* (24), 6109-6143.

73. Hiltner, P. A.; Krieger, I. M., Diffraction of Light by Ordered Suspensions. *The Journal of Physical Chemistry* **1969,** *73* (7), 2386-2389.

74. Baryshev, A. V.; Kosobukin, V. A.; Samusev, K. B.; Usvyat, D. E.; Limonov, M. F., Light Diffraction from Opal-based Photonic Crystals with Growth-induced Disorder: Experiment and Theory. *Physical Review B* **2006,** *73* (20), 205118.

75. Astratov, V. N.; Bogomolov, V. N.; Kaplyanskii, A. A.; Prokofiev, A. V.; Samoilovich, L. A.; Samoilovich, S. M.; Vlasov, Y. A., Optical Spectroscopy of Opal Matrices with CdS Embedded in its Pores: Quantum confinement and photonic band gap effects. *Il Nuovo Cimento D* **1995,** *17* (11), 1349-1354.

76. Vlasov, Y. A.; Astratov, V. N.; Karimov, O. Z.; Kaplyanskii, A. A.; Bogomolov, V. N.; Prokofiev, A. V., Existence Of A Photonic Pseudogap for Visible Light in Synthetic Opals. *Physical Review B* **1997,** *55* (20), R13357-R13360.

77. Bogomolov, V. N.; Gaponenko, S. V.; Germanenko, I. N.; Kapitonov, A. M.; Petrov, E. P.; Gaponenko, N. V.; Prokofiev, A. V.; Ponyavina, A. N.; Silvanovich, N. I.; Samoilovich, S. M., Photonic Band Gap Phenomenon and Optical Properties of Artificial Opals. *Physical Review E* **1997,** *55* (6), 7619-7625.

78. Reynolds, A.; López-Tejeira, F.; Cassagne, D.; J. García-Vidal, F.; Jouanin, C.; Sánchez-Dehesa, J., Spectral Properties of Opal-based Photonic Crystals having a SiO_2 Matrix. *Physical Review B* **1999,** *60* (16), 11422-11426.

79. Golubev, V. G.; Hutchison, J. L.; Kosobukin, V. A.; Kurdyukov, D. A.; Medvedev, A. V.; Pevtsov, A. B.; Sloan, J.; Sorokin, L. M., Three-Dimensional Ordered Silicon-Based Nanostructures in Opal Matrix: Preparation and Photonic Properties. *Journal of Non-Crystalline Solids* **2002,** *299-302* (Part 2), 1062-1069.

80. Thijssen, M. S.; Sprik, R.; Wijnhoven, J. E. G. J.; Megens, M.; Narayanan, T.; Lagendijk, A.; Vos, W. L., Inhibited Light Propagation and Broadband Reflection in Photonic Air-Sphere Crystals. *Physical Review Letters* **1999,** *83* (14), 2730-2733.

81. van Driel, H. M.; Vos, W. L., Multiple Bragg Wave Coupling in Photonic Band-gap Crystals. *Physical Review B* **2000,** *62* (15), 9872-9875.

82. Ge, J.; Yin, Y., Responsive Photonic Crystals. *Angewandte Chemie International Edition* **2011,** *50* (7), 1492-1522.

83. Rundquist, P. A.; Photinos, P.; Jagannathan, S.; Asher, S. A., Dynamical Bragg Diffraction from Crystalline Colloidal Arrays. *The Journal of Chemical Physics* **1989,** *91* (8), 4932-4941.

84. Robert, J. S.; David, J. K., Theoretical Analysis of the Crystalline Colloidal Array Filter. *Applied. Spectroscopy* **1986,** *40* (6), 782-784.

85. Hiltner, P. A.; Papir, Y. S.; Krieger, I. M., Diffraction of Light by Nonaqueous Ordered Suspensions. *The Journal of Physical Chemistry* **1971,** *75* (12), 1881-1886.

86. Liu, L.; Li, P.; Asher, S. A., Fortuitously Superimposed Lattice Plane Secondary Diffraction from Crystalline Colloidal Arrays. *Journal of the American Chemical Society* **1997,** *119* (11), 2729-2732.

87. Zachariasen, W. H., *Theory of X-Ray Diffraction in Crystals*. Dover Publications: 2004.

88. Schroden, R. C.; Al-Daous, M.; Blanford, C. F.; Stein, A., Optical Properties of Inverse Opal Photonic Crystals. *Chemistry of Materials* **2002,** *14* (8), 3305-3315.

89. Grzybowski, B. A.; Wilmer, C. E.; Kim, J.; Browne, K. P.; Bishop, K. J. M., Self-Assembly: from Crystals to Cells. *Soft Matter* **2009,** *5* (6), 1110-1128.

90. Titov, A. V.; Král, P., Modeling the Self-Assembly of Colloidal Nanorod Superlattices. *Nano Letters* **2008,** *8* (11), 3605-3612.

91. Wang, D.; Hore, M. J. A.; Ye, X.; Zheng, C.; Murray, C. B.; Composto, R. J., Gold Nanorod Length Controls Dispersion, Local Ordering, and Optical Absorption in Polymer Nanocomposite Films. *Soft Matter* **2014,** *10* (19), 3404-3413.

92. Baranov, D.; Fiore, A.; van Huis, M.; Giannini, C.; Falqui, A.; Lafont, U.; Zandbergen, H.; Zanella, M.; Cingolani, R.; Manna, L., Assembly of Colloidal Semiconductor Nanorods in Solution by Depletion Attraction. *Nano Letters* **2010,** *10* (2), 743-749.

93. Savenko, S. V.; Dijkstra, M., Phase Behavior of a Suspension of Colloidal Hard Rods and Nonadsorbing Polymer. *The Journal of Chemical Physics* **2006,** *124* (23), 234902.

94. Denkov, N.; Velev, O.; Kralchevski, P.; Ivanov, I.; Yoshimura, H.; Nagayama, K., Mechanism of Formation of Two-Dimensional Crystals orom Latex Particles On Substrates. *Langmuir* **1992,** *8* (12), 3183-3190.

95. Clark, T. D.; Tien, J.; Duffy, D. C.; Paul, K. E.; Whitesides, G. M., Self-Assembly of 10-µm-Sized Objects into Ordered Three-Dimensional Arrays. *Journal of the American Chemical Society* **2001,** *123* (31), 7677-7682.

96. Xia, Y.; Gates, B.; Yin, Y.; Lu, Y., Monodispersed Colloidal Spheres: Old Materials with New Applications. *Advanced Materials* **2000,** *12* (10), 693-713.

97. López, C., Three-Dimensional Photonic Bandgap Materials: Semiconductors for Light. *Journal of Optics A: Pure and Applied Optics* **2006,** *8* (5), R1.

98. Halaoui, L. I.; Abrams, N. M.; Mallouk, T. E., Increasing the Conversion Efficiency of Dye-Sensitized TiO2 Photoelectrochemical Cells by Coupling to Photonic Crystals. *The Journal of Physical Chemistry B* **2005,** *109* (13), 6334-6342.

99. Wanke, M. C.; Lehmann, O.; Müller, K.; Wen, Q.; Stuke, M., Laser Rapid Prototyping of Photonic Band-Gap Microstructures. *Science* **1997,** *275* (5304), 1284-1286.

100. Lucie, M.; Sang Mo, Y.; Sergei, V. K.; Sylvie, S.-C.; Catherine, D., A Review of Molecular Beam Epitaxy of Ferroelectric Batio 3 Films on Si, Ge and Ga as Substrates and Their Applications. *Science and Technology of Advanced Materials* **2015,** *16* (3), 036005.

101. Gong, Q.; Hu, X., *Photonic Crystals: Principles and Applications*. Pan Stanford: 2014.

102. de Sousa Pereira Meneses e Vasconcelos, H. C.; Gonçalves, M. C., *Overall Aspects of Non-Traditional Glasses: Synthesis, Properties and Applications*. Bentham Science Publishers: 2016.

103. Campbell, M.; Sharp, D. N.; Harrison, M. T.; Denning, R. G.; Turberfield, A. J., Fabrication of Photonic Crystals for The Visible Spectrum by Holographic Lithography. *Nature* **2000,** *404*, 53.

104. Pradeesh, K.; Rao Kotla, N.; Ahmad, S.; Dwivedi, V. K.; Prakash, G. V., Naturally Self-Assembled Nanosystems and Their Templated Structures for Photonic Applications. *Journal of Nanoparticles* **2013,** *2013*, 13.

105. Zhang, P. Q.; Xie, X. S.; Guan, Y. F.; Zhou, J. Y.; Wong, K. S.; Yan, L., Adaptive Synthesis of Optical Pattern for Photonic Crystal Lithography. *Applied Physics B* **2011,** *104* (1), 113-116.

106. Feiertag, G.; Ehrfeld, W.; Freimuth, H.; Kolle, H.; Lehr, H.; Schmidt, M.; Sigalas, M. M.; Soukoulis, C. M.; Kiriakidis, G.; Pedersen, T.; Kuhl, J.; Koenig, W., Fabrication of Photonic Crystals by Deep X-Ray Lithography. *Applied Physics Letters* **1997,** *71* (11), 1441-1443.

107. Yuan, L.; Herman, P. R., Laser Scanning Holographic Lithography for Flexible 3D Fabrication of Multi-Scale Integrated Nano-structures and Optical Biosensors. *Scientific Reports* **2016,** *6*, 22294.

108. Sang Hoon, K.; Ki-Dong, L.; Ja-Yeon, K.; Min-Ki, K.; Seong-Ju, P., Fabrication of Photonic Crystal Structures on Light Emitting Diodes by Nanoimprint Lithography. *Nanotechnology* **2007,** *18* (5), 055306.

109. Vogelaar, L.; Nijdam, W.; van Wolferen, H. A. G. M.; de Ridder, R. M.; Segerink, F. B.; Flück, E.; Kuipers, L.; van Hulst, N. F., Large Area Photonic Crystal Slabs for Visible Light with Waveguiding Defect Structures: Fabrication with Focused Ion Beam Assisted Laser Interference Lithography. *Advanced Materials* **2001,** *13* (20), 1551-1554.

110. Eckert, A. W., *The World of Opals*. Wiley: 1997.

111. Waterhouse, G. I. N.; Waterland, M. R., Opal and Inverse Opal Photonic Crystals: Fabrication and Characterization. *Polyhedron* **2007,** *26* (2), 356-368.

112. Marlow, F.; Muldarisnur; Sharifi, P.; Brinkmann, R.; Mendive, C., Opals: Status and Prospects. *Angewandte Chemie International Edition* **2009,** *48* (34), 6212-6233.

113. Stöber, W.; Fink, A.; Bohn, E., Controlled Growth of Monodisperse Silica Spheres in the Micron Size Range. *Journal of Colloid and Interface Science* **1968,** *26* (1), 62-69.

114. Braun, P. V.; Wiltzius, P., Electrochemically Grown Photonic Crystals. *Nature* **1999,** *402*, 603-604.

115. Trau, M.; Saville, D. A.; Aksay, I. A., Field-Induced Layering of Colloidal Crystals. *Science* **1996,** *272* (5262), 706-709.

116. Jiang, P.; Bertone, J. F.; Hwang, K. S.; Colvin, V. L., Single-Crystal Colloidal Multilayers of Controlled Thickness. *Chemistry of Materials* **1999,** *11* (8), 2132-2140.

117. Wang, L.; Wan, Y.; Li, Y.; Cai, Z.; Li, H.-L.; Zhao, X. S.; Li, Q., Binary Colloidal Crystals Fabricated with a Horizontal Deposition Method. *Langmuir* **2009,** *25* (12), 6753-6759.

118. Tétreault, N.; Míguez, H; Ozin, G. A.; Silicon Inverse Opal—A Platform for Photonic Bandgap Research. *Advanced Materials* **2004,** *16* (16), 1471-1476.

119. Waterhouse, G. I. N.; Chen, W.-T.; Chan, A.; Jin, H.; Sun-Waterhouse, D.; Cowie, B. C. C., Structural, Optical, and Catalytic Support Properties of γ-Al2O3 Inverse Opals. *The Journal of Physical Chemistry C* **2015,** *119* (12), 6647-6659.

120. Nishimura, S.; Abrams, N.; Lewis, B. A.; Halaoui, L. I.; Mallouk, T. E.; Benkstein, K. D.; van de Lagemaat, J.; Frank, A. J., Standing Wave Enhancement of Red Absorbance and Photocurrent in Dye-Sensitized Titanium Dioxide Photoelectrodes Coupled to Photonic Crystals. *Journal of the American Chemical Society* **2003,** *125* (20), 6306-6310.

121. Somani, P. R.; Dionigi, C.; Murgia, M.; Palles, D.; Nozar, P.; Ruani, G., Solid-State Dye PV Cells Using Inverse Opal TiO_2 Films. *Solar Energy Materials and Solar Cells* **2005,** *87* (1), 513-519.

122. Nelson, E. C.; Dias, N. L.; Bassett, K. P.; Dunham, S. N.; Verma, V.; Miyake, M.; Wiltzius, P.; Rogers, J. A.; Coleman, J. J.; Li, X.; Braun, P. V., Epitaxial Growth of Three-Dimensionally Architectured Optoelectronic Devices. *Nature Materials* **2011,** *10*, 676.

123. Sakamoto, J. S.; Dunn, B., Hierarchical Battery Electrodes Based on Inverted Opal Structures. *Journal of Materials Chemistry* **2002,** *12* (10), 2859-2861.

124. Nishijima, Y.; Ueno, K.; Juodkazis, S.; Mizeikis, V.; Misawa, H.; Maeda, M.; Minaki, M., Tunable Single-Mode Photonic Lasing from Zirconia Inverse Opal Photonic Crystals. *Optics Express* **2008,** *16* (18), 13676-13684.

125. Zhang, J.; Liu, H.; Wang, Z.; Ming, N., Assembly Of High-Quality Colloidal Crystals Under Negative Pressure. *Journal of Applied Physics* **2008,** *103* (1), 013517.

126. Chung, Y.-W.; Leu, I.-C.; Lee, J.-H.; Hon, M.-H., Influence of Humidity on the Fabrication of High-Quality Colloidal Crystals via a Capillary-Enhanced Process. *Langmuir* **2006,** *22* (14), 6454-6460.

127. Zhang, J.; Luo, X.; Yan, X.; Zhu, G., Fabrication of High-Quality Colloidal Crystal Films by Vertical Deposition Method Integrated With a Piezoelectric Actuator. *Thin Solid Films* **2010,** *518* (18), 5204-5208.

128. Wendt, J. R.; Vawter, G. A.; Gourley, P. L.; Brennan, T. M.; Hammons, B. E., Nanofabrication of Photonic Lattice Structures in GaAs/AlGaAs. *Journal of Vacuum Science & Technology B: Microelectronics and Nanometer Structures Processing, Measurement, and Phenomena* **1993,** *11* (6), 2637-2640.

129. García-Santamaría, F.; Miyazaki, H. T.; Urquía, A.; Ibisate, M.; Belmonte, M.; Shinya, N.; Meseguer, F.; López, C., Nanorobotic Manipulation of Microspheres for On-Chip Diamond Architectures. *Advanced Materials* **2002,** *14* (16), 1144-1147.

130. Arsenault, A. C.; Clark, T. J.; von Freymann, G.; Cademartiri, L.; Sapienza, R.; Bertolotti, J.; Vekris, E.; Wong, S.; Kitaev, V.; Manners, I.; Wang, R. Z.; John, S.; Wiersma, D.; Ozin, G. A., From Colour Fingerprinting to the Control of Photoluminescence in Elastic Photonic Crystals. *Nature Materials* **2006,** *5* (3), 179-184.

131. Blanco, A.; Chomski, E.; Grabtchak, S.; Ibisate, M.; John, S.; Leonard, S. W.; Lopez, C.; Meseguer, F.; Miguez, H.; Mondia, J. P.; Ozin, G. A.; Toader, O.; van Driel, H. M., Large-scale Synthesis of a Silicon Photonic Crystal With a Complete Three-Dimensional Bandgap Near 1.5 Micrometres. *Nature* **2000,** *405* (6785), 437-440.

132. Rinne, S. A.; Garcia-Santamaria, F.; Braun, P. V., Embedded Cavities and Waveguides in Three-Dimensional Silicon Photonic Crystals. *Nature Photonics* **2008,** *2* (1), 52-56.

133. Guan, G.; Zapf, R.; Kolb, G.; Hessel, V.; Löwe, H.; Ye, J.; Zentel, R., Preferential CO Oxidation Over Catalysts with Well-Defined Inverse Opal Structure in Microchannels. *International Journal of Hydrogen Energy* **2008,** *33* (2), 797-801.

134. Lee, K.; Asher, S. A., Photonic Crystal Chemical Sensors: pH and Ionic Strength. *Journal of the American Chemical Society* **2000,** *122* (39), 9534-9537.

135. Lee, J.; Shanbhag, S.; Kotov, N. A., Inverted Colloidal Crystals as Three-Dimensional Microenvironments For Cellular Co-Cultures. *Journal of Materials Chemistry* **2006,** *16* (35), 3558-3564.

136. Han, W.; Li, B.; Lin, Z., Drying-Mediated Assembly of Colloidal Nanoparticles into Large-Scale Microchannels. *ACS Nano* **2013,** *7* (7), 6079-6085.

137. Allain, C.; Limat, L., Regular Patterns of Cracks Formed by Directional Drying of a Collodial Suspension. *Physical Review Letters* **1995,** *74* (15), 2981-2984.

138. Jagla, E. A., Stable Propagation of an Ordered Array of Cracks During Directional Drying. *Physical Review E* **2002,** *65* (4), 046147.

139. Lidon, P.; Salmon, J.-B., Dynamics of Unidirectional Drying of Colloidal Dispersions. *Soft Matter* **2014,** *10* (23), 4151-4161.

140. Tirumkudulu, M. S.; Russel, W. B., Cracking in Drying Latex Films. *Langmuir* **2005,** *21* (11), 4938-4948.

141. Míguez, H.; Meseguer, F.; López, C.; Blanco, Á.; Moya, J. S.; Requena, J.; Mifsud, A.; Fornés, V., Control of the Photonic Crystal Properties of fcc-Packed Submicrometer SiO_2 Spheres by Sintering. *Advanced Materials* **1998,** *10* (6), 480-483.

142. McLachlan, M. A.; Johnson, N. P.; Rue, R. M. D. L.; McComb, D. W., Thin Film Photonic Crystals: Synthesis and Characterisation. *Journal of Materials Chemistry* **2004,** *14* (2), 144-150.

143. Klein, S.; Manoharan, V.; Pine, D.; Lange, F., Preparation of Monodisperse PMMA Microspheres in Nonpolar Solvents by Dispersion Polymerization with a Macromonomeric Stabilizer. *Colloid and Polymer Science* **2003,** *282* (1), 7-13.

144. Pusey, P. N.; Zaccarelli, E.; Valeriani, C.; Sanz, E.; Poon, W. C. K.; Cates, M. E., Hard Spheres: Crystallization and Glass Formation. *Philosophical Transactions of the Royal Society A: Mathematical, Physical and Engineering Sciences* **2009,** *367* (1909), 4993-5011.

145. Nemati, K. M., Fracture Analysis of Concrete Using Scanning Electron Microscopy. *Scanning* **1997,** *19* (6), 426-430.

146. Nemati, K. M.; Stroeven, P., Stereological Analysis of Micromechanical Behavior of Concrete. *Materials and Structures* **2001**, 34 (8), 486-494.

147. Koh, Y. K.; Yip, C. H.; Chiang, Y.-M.; Wong, C. C., Kinetic Stages of Single-Component Colloidal Crystallization. *Langmuir* **2008,** *24* (10), 5245-5248.

148. Malvern.com. Inform white paper, Dynamic Light Scattering Common Terms Defined 2015. https://www.malvernpanalytical.com/en/learn/knowledgecenter/Whitepapers/WP111214DLSTermsDefined.html

149. Lu, G. W.; Gao, P., CHAPTER 3 - Emulsions and Microemulsions for Topical and Transdermal Drug Delivery A2 - Kulkarni, Vitthal S. In *Handbook of Non-Invasive Drug Delivery Systems*, William Andrew Publishing: Boston, 2010; 59-94.

150. O'Brien, R. W.; Midmore, B. R.; Lamb, A.; Hunter, R. J., Electroacoustic Studies of Moderately Concentrated Colloidal Suspensions. *Faraday Discussions of the Chemical Society* **1990,** *90* (0), 301-312.

151. Hanaor, D.; Michelazzi, M.; Leonelli, C.; Sorrell, C. C., The Effects of Carboxylic Acids on the Aqueous Dispersion and Electrophoretic Deposition of ZrO_2. *Journal of the European Ceramic Society* **2012,** *32* (1), 235-244.

152. Castañeda-Uribe, O. A.; Salcedo-Reyes, J. C.; Méndez-Pinzón, H. A.; Pedroza-Rodríguez, A. M., Fabrication and Optical Characterization of a High-Quality Fcc-Opal-Based Photonic Crystal Grown by The Vertical Convective Self-Assembly Method. *Universitas Scientiarum* **2010,** *15* (2), 150-158.

153. Tan, K. W.; Koh, Y. K.; Chiang, Y.-M.; Wong, C. C., Particulate Mobility in Vertical Deposition of Attractive Monolayer Colloidal Crystals. *Langmuir* **2010,** *26* (10), 7093-7100.

154. Tan, K. W.; Li, G.; Koh, Y. K.; Yan, Q.; Wong, C. C., Layer-by-Layer Growth of Attractive Binary Colloidal Particles. *Langmuir* **2008,** *24* (17), 9273-9278.

155. Shapiro, L. G.; Stockman, G. C., *Computer Vision*. Prentice Hall: 2001.

156. Zhao, X. S.; Su, F.; Yan, Q.; Guo, W.; Bao, X. Y.; Lv, L.; Zhou, Z., Templating Methods for

Preparation of Porous Structures. *Journal of Materials Chemistry* **2006,** *16* (7), 637-648.

157. Fudouzi, H., CHAPTER 3 Opal Photonic Crystal Films with Tunable Structural Color. In *Responsive Photonic Nanostructures: Smart Nanoscale Optical Materials*, The Royal Society of Chemistry: 2013; 44-62.

158. Phillips, K. R.; Vogel, N.; Hu, Y.; Kolle, M.; Perry, C. C.; Aizenberg, J., Tunable Anisotropy in Inverse Opals and Emerging Optical Properties. *Chemistry of Materials* **2014,** *26* (4), 1622-1628.

159. Jin, C.; Meng, X.; Cheng, B.; Li, Z.; Zhang, D., Photonic Gap in Amorphous Photonic Materials. *Physical Review B* **2001,** *63* (19), 195107.

160. Ueno, K.; Inaba, A.; Sano, Y.; Kondoh, M.; Watanabe, M., A Soft Glassy Colloidal Array in Ionic Liquid, which Exhibits Homogeneous, Non-Brilliant and Angle-Independent Structural Colours. *Chemical Communications* **2009,** (24), 3603-3605.

161. Gu, Z.-Z.; Fujishima, A.; Sato, O., Fabrication of High-Quality Opal Films with Controllable Thickness. *Chemistry of Materials* **2002,** *14* (2), 760-765.

162. Maurin, I.; Moufarej, E.; Laliotis, A.; Bloch, D., Optics Of An Opal Modeled with a Stratified Effective Index and the Effect of The Interface. *J. Opt. Soc. Am. B* **2015,** *32* (8), 1761-1772.

163. Dufresne, E. R.; Corwin, E. I.; Greenblatt, N. A.; Ashmore, J.; Wang, D. Y.; Dinsmore, A. D.; Cheng, J. X.; Xie, X. S.; Hutchinson, J. W.; Weitz, D. A., Flow and Fracture in Drying

Nanoparticle Suspensions. *Physical Review Letters* **2003,** *91* (22), 224501.

164. Lee, W. P.; Routh, A. F., Why Do Drying Films Crack? *Langmuir* **2004,** *20* (23), 9885-9888.

165. Pauchard, L.; Abou, B.; Sekimoto, K., Influence of Mechanical Properties of Nanoparticles on Macrocrack Formation. *Langmuir* **2009,** *25* (12), 6672-6677.

166. Dragnevski, K. I.; Routh, A. F.; Murray, M. W.; Donald, A. M., Cracking of Drying Latex Films: An ESEM Experiment. *Langmuir* **2010,** *26* (11), 7747-7751.

167. Atkinson, A.; Guppy, R. M., Mechanical stability of sol-gel films. *Journal of Materials Science* **1991,** *26* (14), 3869-3873.

168. Groisman, A.; Kaplan, E., An Experimental Study of Cracking Induced by Desiccation. *EPL (Europhysics Letters)* **1994,** *25* (6), 415.

169. Gauthier, G.; Lazarus, V.; Pauchard, L., Shrinkage Star-Shaped Cracks: Explaining The Transition from 90 Degrees to 120 Degrees. *EPL (Europhysics Letters)* **2010,** *89* (2), 26002.

170. Lazarus, V.; Pauchard, L., From Craquelures to Spiral Crack Patterns: Influence of Layer Thickness on the Crack Patterns Induced by Desiccation. *Soft Matter* **2011,** *7* (6), 2552-2559.

171. Kitagawa, K., Thin-Film Thickness Profile Measurement by Three-Wavelength Interference Color Analysis. *Appl. Opt.* **2013,** *52* (10), 1998-2007.

172. Cong, H.; Cao, W., Colloidal Crystallization Induced by Capillary Force. *Langmuir* **2003,** *19* (20), 8177-8181.

173. Teh, L. K.; Tan, N. K.; Wong, C. C.; Li, S., Growth Imperfections in Three-Dimensional Colloidal Self-Assembly. *Applied Physics A* **2005,** *81* (7), 1399-1404.

174. Shokri, N.; Zhou, P.; Keshmiri, A., Patterns of Desiccation Cracks in Saline Bentonite Layers. *Transport in Porous Media* **2015,** *110* (2), 333-344.

175. Tilley, R. J. D., *Defects in Solids*. Wiley: 2008.

176. Iler, R. K., *The Chemistry of Silica: Solubility, Polymerization, Colloid and Surface Properties and Biochemistry of Silica*. Wiley: 1979.

177. Hench, L. L.; West, J. K., The Sol-Gel Process. *Chemical Reviews* **1990,** *90* (1), 33-72.

178. Brinker, C. J., Glasses and Glass Ceramics from Gels Hydrolysis and Condensation of Silicates: Effects on Structure. *Journal of Non-Crystalline Solids* **1988,** *100* (1), 31-50.

179. Blanford, C. F.; Carter, C. B.; Stein, A., A Method for Determining Void Arrangements in Inverse Opals. *Journal of Microscopy* **2004,** *216* (3), 263-287.

180. Galisteo-López, J. F.; Ibisate, M.; Sapienza, R.; Froufe-Pérez, L. S.; Blanco, Á.; López, C., Self-Assembled Photonic Structures. *Advanced Materials* **2011,** *23* (1), 30-69.

181. Velev, O. D.; Lenhoff, A. M., Colloidal Crystals as TemplatesfFor Porous Materials.

Current Opinion in Colloid & Interface Science **2000,** *5* (1), 56-63.

182. Holland, B. T.; Blanford, C. F.; Do, T.; Stein, A., Synthesis of Highly Ordered, Three-Dimensional, Macroporous Structures of Amorphous or Crystalline Inorganic Oxides, Phosphates, and Hybrid Composites. *Chemistry of Materials* **1999,** *11* (3), 795-805.

183. Wijnhoven, J. E. G. J.; Vos, W. L., Preparation of Photonic Crystals Made of Air Spheres in Titania. *Science* **1998,** *281* (5378), 802-804.

184. Lanata, M.; Cherchi, M.; Zappettini, A.; Pietralunga, S. M.; Martinelli, M., Titania Inverse Opals for Infrared Optical Applications. *Optical Materials* **2001,** *17* (1), 11-14.

185. Cumpston, B. H.; Ananthavel, S. P.; Barlow, S.; Dyer, D. L.; Ehrlich, J. E.; Erskine, L. L.; Heikal, A. A.; Kuebler, S. M.; Lee, I. Y. S.; McCord-Maughon, D.; Qin, J.; Röckel, H.; Rumi, M.; Wu, X.-L.; Marder, S. R.; Perry, J. W., Two-Photon Polymerization Initiators for Three-Dimensional Optical Data Storage and Microfabrication. *Nature* **1999,** *398,* 51-54.

186. Zhang, Y. S.; Zhu, C.; Xia, Y., Inverse Opal Scaffolds and Their Biomedical Applications. *Advanced Materials* **2017,** *29* (33), 1701115.

187. Painter, O.; Lee, R. K.; Scherer, A.; Yariv, A.; O'Brien, J. D.; Dapkus, P. D.; Kim, I., Two-Dimensional Photonic Band-Gap Defect Mode Laser. *Science* **1999,** *284* (5421), 1819-1821.

188. Lytle, J. C.; Stein, A., Recent Progress in Syntheses and Applications of Inverse Opals and Related Macroporous Materials Prepared by Colloidal Crystal Templating. In *Annual Review of Nano Research*, World Scientific: 2011; 1-79.

189. Blanford, C. F.; Do, T. N.; Holland, B. T.; Stein, A., Synthesis Of Highly Ordered Macroporous Minerals: Extension of the Synthetic Method to Other Metal Oxides and Organic-Inorganic Composites. *MRS Proceedings* **2011,** *549*, 61.

190. Dougherty, E. R.; Lotufo, R. A., *Hands-on Morphological Image Processing*. Society of Photo Optical: 2003.

191. Aubert, E.; Lecomte, C., Illustrated Fourier Transforms for Crystallography. *Journal of Applied Crystallography* **2007,** *40* (6), 1153-1165.

192. Casillas, D. C.; Wilkinson, D. C.; Lai, C. H.; Wilke, S. K.; Ignatowich, M. J.; Haile, S. M.; Dunn, B. S., High-Temperature Structural Stability of Ceria-Based Inverse Opals. *Journal of the American Ceramic Society* **2017,** *100* (6), 2659-2668.

193. Mishchenko, L.; Hatton, B.; Kolle, M.; Aizenberg, J., Patterning Hierarchy in Direct and Inverse Opal Crystals. *Small* **2012,** *8* (12), 1904-1911.

194. Palacios-Lidón, E.; Juárez, B. H.; Castillo-Martínez, E.; López, C., Optical and Morphological Study of Disorder in Opals. *Journal of Applied Physics* **2005,** *97* (6), 063502.

195. Nicolas, S.; Benjamin, R.; Jean-Pierre, G.; A., C. J.; Emmanuel, F., Investigation of Hidden Periodic Structures on SEM Images of Opal-Like Materials using FFT and IFFT. *Scanning* **2014,** *36* (5), 487-499.

196. Scherer, G. W., Effect Of Shrinkage On The Modulus of Silica Gel. *Journal of Non-Crystalline Solids* **1989,** *109* (2), 183-190.

197. Wilkes, P., *Solid State Theory in Metallurgy*. Cambridge University Press: 1973.

198. Buenger, D.; Topuz, F.; Groll, J., Hydrogels in Sensing Applications. *Progress in Polymer Science* **2012,** *37* (12), 1678-1719.

199. Peppas, N. A.; Ottenbrite, R. M.; Park, K.; Okano, T., *Biomedical Applications of Hydrogels Handbook*. Springer New York: 2010.

200. Blyth, J.; Millington, R. B.; Mayes, A. G.; Frears, E. R.; Lowe, C. R., Holographic Sensor for Water in Solvents. *Analytical Chemistry* **1996,** *68* (7), 1089-1094.

201. Millington, R. B.; Mayes, A. G.; Blyth, J.; Lowe, C. R., A Hologram Biosensor for Proteases. *Sensors and Actuators B: Chemical* **1996,** *33* (1), 55-59.

202. Spooncer, R. C.; Al-Ramadhan, F. A.; Jones, B. E., A Humidity Sensor using a Wavelength-Dependent Holographic Filter with Fibre Optic Links. *International Journal of Optoelectronics.* **1992,** *7* (3), 449-452.

203. Yetisen, A. K., Fundamentals of Holographic Sensing. In *Holographic Sensors*, Springer International Publishing: Cham, 2015; 27-51.

204. Carlson, R. J.; Asher, S. A., Characterization of Optical Diffraction and Crystal Structure in Monodisperse Polystyrene Colloids. *Applied Spectroscopy* **1984,** *38* (3), 297-304.

205. Yuanjin, Z.; Xiangwei, Z.; Zhongze, G., Photonic Crystals in Bioassays. *Advanced Functional Materials* **2010,** *20* (18), 2970-2988.

206. Ueno, K.; Matsubara, K.; Watanabe, M.; Takeoka, Y., An Electro- and Thermochromic Hydrogel as a Full-Color Indicator. *Advanced Materials* **2007,** *19* (19), 2807-2812.

207. Saito, H.; Takeoka, Y.; Watanabe, M., Simple And Precision Design of Porous Gel as a Visible Indicator for Ionic Species and Concentration. *Chemical Communications* **2003,** (17), 2126-2127.

208. Takeoka, Y.; Watanabe, M., Template Synthesis and Optical Properties of Chameleonic Poly(N-isopropylacrylamide) Gels using Closest-Packed Self-Assembled Colloidal Silica Crystals. *Advanced Materials* **2003,** *15* (3), 199-201.

209. Barry, R. A.; Wiltzius, P., Humidity-Sensing Inverse Opal Hydrogels. *Langmuir* **2006,** *22* (3), 1369-1374.

210. Yetisen, A. K.; Butt, H.; Volpatti, L. R.; Pavlichenko, I.; Humar, M.; Kwok, S. J. J.; Koo, H.; Kim, K. S.; Naydenova, I.; Khademhosseini, A.; Hahn, S. K.; Yun, S. H., Photonic Hydrogel Sensors. *Biotechnology Advances* **2016,** *34* (3), 250-271.

211. Seidel, J. M.; Malmonge, S. M., Synthesis of Polyhema Hydrogels for Using as Biomaterials. Bulk and Solution Radical-Initiated Polymerization Techniques. *Materials Research* **2000,** *3*, 79-83.

212. Wichterle, O.; LÍM, D., Hydrophilic Gels for Biological Use. *Nature* **1960,** *185*, 117.

213. Chirila, T. V.; Chen, Y. C.; Griffin, B. J.; Constable, I. J., Hydrophilic Sponges Based on 2-Hydroxyethyl Methacrylate. I. Effect of Monomer Mixture Composition on The Pore Size. *Polymer International* **1993,** *32* (3), 221-232.

214. Chirila, T. V.; Constable, I. J.; Crawford, G. J.; Vijayasekaran, S.; Thompson, D. E.; Chen, Y.-C.; Fletcher, W. A.; Griffin, B. J., Poly(2-Hydroxyethyl Methacrylate) Sponges as Implant Materials: In Vivo and in Vitro Evaluation of Cellular Invasion. *Biomaterials* **1993,** *14* (1), 26-38.

215. Oxley, H. R.; Corkhill, P. H.; Fitton, J. H.; Tighe, B. J., Macroporous Hydrogels for Biomedical Applications: methodology and morphology. *Biomaterials* **1993,** *14* (14), 1064-1072.

216. Kon, M.; de Visser, A. C., A poly(HEMA) Sponge for Restoration of Articular Cartilage Defects. *Plastic and Reconstructive Surgery* **1981,** *67* (3), 288-294.

217. Lee, Y.-J.; Braun, P. V., Tunable Inverse Opal Hydrogel pH Sensors. *Advanced Materials* **2003,** *15* (7-8), 563-566.

218. Wei, H.; Xiaobin, H.; Binyuan, Z.; Fan, Z.; Di, Z., Tunable Photonic Polyelectrolyte Colorimetric Sensing for Anions, Cations and Zwitterions. *Advanced Materials* **2010,** *22* (44), 5043-5047.

219. Couturier, J.-P.; Wischerhoff, E.; Bernin, R.; Hettrich, C.; Koetz, J.; Sütterlin, M.; Tiersch, B.; Laschewsky, A., Thermoresponsive Polymers and Inverse Opal Hydrogels for the Detection of Diols. *Langmuir* **2016,** *32* (17), 4333-4345.

220. You, J.-O.; Auguste, D. T., Conductive, Physiologically Responsive Hydrogels. *Langmuir* **2010,** *26* (7), 4607-4612.

221. van de Wetering, P.; Zuidam, N. J.; van Steenbergen, M. J.; van der Houwen, O. A. G. J.; Underberg, W. J. M.; Hennink, W. E., A Mechanistic Study of the Hydrolytic Stability of Poly(2-(dimethylamino)ethyl methacrylate). *Macromolecules* **1998,** *31* (23), 8063-8068.

222. Samsonova, O.; Pfeiffer, C.; Hellmund, M.; Merkel, O. M.; Kissel, T., Low Molecular Weight pDMAEMA-block-pHEMA Block-Copolymers Synthesized via RAFT-Polymerization: Potential Non-Viral Gene Delivery Agents? *Polymers* **2011,** *3* (2), 693.

223. Gupta, N. V.; Shivakumar, H. G., Investigation of Swelling Behavior and Mechanical Properties of a pH-Sensitive Superporous Hydrogel Composite. *Iranian Journal of Pharmaceutical Research : IJPR* **2012,** *11* (2), 481-493.

224. Zhang, M.; Cheng, Z.; Zhao, T.; Liu, M.; Hu, M.; Li, J., Synthesis, Characterization, and Swelling Behaviors of Salt-Sensitive Maize Bran–Poly(acrylic acid) Superabsorbent Hydrogel. *Journal of Agricultural and Food Chemistry* **2014,** *62* (35), 8867-8874.

225. Wang, J.; Han, Y., Tunable Multiresponsive Methacrylic Acid Based Inverse Opal Hydrogels Prepared by Controlling the Synthesis Conditions. *Langmuir* **2009,** *25* (3), 1855-1864.

226. Yang, Q.; Peng, H.; Li, J.; Li, Y.; Xiong, H.; Chen, L., Label-Free Colorimetric Detection of Tetracycline using Analyte-Responsive Inverse-Opal Hydrogels Based on Molecular Imprinting Technology. *New Journal of Chemistry* **2017,** *41* (18), 10174-10180.Shi, D.; Zhang, X.; Yang, Z.; Liu, S.; Chen, M., Fabrication of PAM/PMAA Inverse Opal Photonic Crystal Hydrogels by a

"Sandwich" Method and Their pH And Solvent Responses. *RSC Advances* **2016,** *6* (89), 85885-85890.

227. Shi, D.; Zhang, X.; Yang, Z.; Liu, S.; Chen, M., Fabrication of PAM/PMAA inverse opal photonic crystal hydrogels by a "sandwich" method and their pH and solvent responses. *RSC Advances* **2016,** *6* (89), 85885-85890.

VITA

Ujith S. K. Madduma-Bandarage

Candidate for the Degree of
Doctor of Philosophy

Thesis: FABRICATION AND CHARATERIZATION OF INVERSE OPALS WITH TUNABLE STOPBANDS

Major Field: Chemistry

Biographical:

Education:

- Completed the requirements for the Doctor of Philosophy in Chemistry at Oklahoma State University, Stillwater, Oklahoma in July, 2018.
- Completed the requirements for the Bachelor of Science in Chemistry at University of Kelaniya, Kelaniya, Sri Lanka in 2010.

Experience:

- Graduate Research/ Teaching Assistant (Year 2012- 2018), Oklahoma State University, Stillwater, Oklahoma, USA.
- Research fields – Material science, Nano-material synthesis, photonic materials
- Teaching Assistant (Year 2010- 2011), Department of Chemistry, University of Kelaniya, Sri Lanka.
- Teaching Assistant (Year 2011- 2012), Department of Chemistry, Open University, Sri Lanka.

Publication:

Thushara J. Athauda, **Ujith S. K. Madduma-Bandarage**, and Yolanda Vasquez, "Integration of ZnO/ZnS nanostructured materials into a cotton fabric platform," RSC Advances, 2014, 4, 61327-61332.

Awards:

- 3rd place for the oral presentation at Annual Research Symposium in 2016 at Oklahoma State University Stillwater.
- 2nd place for the poster presentation at ACS Pentasectional in 2017 at Cameron University campus, Lawton, Oklahoma.

Professional Memberships:

- Member of the American Chemical Society (2014 – Present)
- Golden Key International Honour Society (2014 – Present)